



universität  
wien

# DISSERTATION / DOCTORAL THESIS

Titel der Dissertation / Title of the Doctoral Thesis

## Allosteric Modulation of Macromolecular Machines by Small Molecules

verfasst von / submitted by

Jiří Wald

angestrebter akademischer Grad / in partial fulfilment of the requirements for the degree of

Doctor of Philosophy (PhD)

Wien, 2021 / Vienna, 2021

Studienkennzahl lt. Studienblatt /  
degree programme code as it appears on the student  
record sheet:

UA-794 685 490

Dissertationsgebiet lt. Studienblatt /  
field of study as it appears on the student record sheet:

Molecular Biology

Betreut von / Supervisor:

Dr. Thomas Christian Marlovits, Privatdoz.



## **Abstract**

Broadly speaking, machines are complex devices composed of different parts that consume energy to perform various activities. Such machines can be also found in nature, where they are molecular assemblies of proteins, nucleic acids and carbohydrates. These machines are fundamental elements in basic life involved in construction of viruses all living cells. Understanding the mechanistical aspects underlying these processes requires detailed knowledge of the overall architecture and atomic organization of the entire biological macromolecular machine. Due to their structural and functional complexity, structural characterization of these macromolecules is often a challenging experimental effort and is often narrowed to determination of isolated sub-structures offering only limited conceptual understanding. Moreover, specific conformation of the atomic structure often depends on the presence of small molecules, that positively or negatively regulate specialized activity of the entire macromolecule through allosteric modulation of the structural organization. Therefore, structure determination of the whole molecular machine in the presence of the small molecules actively acting as regulators is often the key to understand the underlying mechanism. In this thesis, cryo-electron microscopy (cryo-EM) single-particle analysis was used to characterize the structure of two macromolecular assemblies in the presence of small molecules: (1) the prokaryotic RuvAB branch migration machinery complexed to Holliday junction and ATPgS/ADP (RuvAB-HJ) and (2) the pleconaril-resistant human rhinovirus-B5 (HRV-B5) complexed to novel antiviral compound OBR-5-340.

## Zusammenfassung

Im Allgemeinen gesehen sind Maschinen komplexe Objekte, bestehend aus verschiedenen Komponenten und angetrieben von Energie um verschiedenartigste Aufgaben durchführen zu können. Diese Art von Maschinen kommen auch in der Natur vor. In diesem Fall sind sie molekulare Bausteine bestehend aus Proteinen, Nukleinsäuren und Kohlehydraten. Darüber hinaus sind Maschinen fundamentale Elemente des einfachen Lebens, die für die Konstruktion von Viren benötigt werden und in allen lebenden Zellen vorkommen. Um die Funktionsweise der biologischen, makromolekularen Maschinen zu verstehen, ist es notwendig sich mit den grundlegenden, mechanischen Aspekten auseinanderzusetzen. Dazu ist es notwendig ein detailliertes Wissen über die generelle Architektur, aber auch der Organisation der gesamten biologischen, markomolekularen Maschine auf nahezu Atomebene zu erforschen. Aufgrund der strukturellen und funktionalen Komplexität von diesen Makromolekülen ist dieser Prozess anspruchsvoll und experimentell aufwendig. Oft beschränkt man sich dabei auf die Ermittlung der Funktionsweise von isolierten Substrukturen, die allerdings nur ein beschränktes Verständnis des Gesamtkonzeptes zulassen. Darüber hinaus hängt die spezifische Angleichung der atomaren Strukturen oft von der Anwesenheit von kleinen Molekülen ab. Diese regulieren im positiven wie im negativen Sinne durch spezielle Aktivitäten das gesamte Makromolekül mittels allosterischer Umwandlung der Konformation. Aus diesem Grund besteht die Strukturbestimmung der gesamten molekularen Maschine aus dem Vorhandensein von kleinen Molekülen. Deren Rolle als Regulatoren ist oft der Schlüssel um die darunterliegenden Mechanismen zu verstehen. In dieser Doktorarbeit wurde die Kryoelektronenmikroskopie (Kryo-EM) Einzelpartikelanalyse verwendet um die Struktur von zwei makromolekularen Baugruppen mittels Vorhandensein von kleinen Molekülen zu charakterisieren: (1) die prokariotische RuvAB Verzweigungswanderungsmaschine im Komplex mit der Holliday-Struktur in Präsenz von ATPgS/ADP (RuvAB-HJ) und (2) der Pleconaril-resistente, menschliche Rhinovirus-B5 (HRV-B5) in Präsenz des antiviralen Wirkstoffes OBR-5-340.

## **Acknowledgments**

This work would never be possible without a great help and support from many people. First and foremost, I would like to thank my supervisor Thomas C. Marlovits for giving me the great opportunity to work in his group, freedom to design my own experiments and his continuous support. I am extremely grateful to Lux (Wolfgang Lugmayr) for all his support and encouragement, which was through the years very vital, Luciano Ciccarelli who helped me during the initial cryo-EM phase of the RuvAB project, Nikolaus Gösweiner-Mohr and Oliver Vesper for their support during the biochemical preparation of the RuvAB sample and finally Dirk Fahrenkamp who joined the RuvAB project in the critical moment on the “last mile” and helped me to finish it. I would also like to thank Dieter Blaas and the entire team of the human rhinovirus project. Special thanks to all current and previous Marlovits lab members and my PhD. committee for all discussions and help. It truly has been extraordinary time in this lab and was a privilege to work with all of you – thank you! However, nobody has been more important to me in the pursuit of this work than my family. Especially, I would like to thank my Mom and Dad, whose love and guidance are with me in whatever I pursue and also my brother Tom of his great scientific and non-scientific advices.

Most importantly, I wish to thank my loving, supportive and patient wife Dominika, who made countless sacrifices to help me get to this point – but most of all, thank you for being my best friend. Without you I would not be the person I am today.

# Table of Contents

Abstract .....	1
Zusammenfassung .....	2
Acknowledgments .....	3
Table of Contents .....	4
Preamble .....	5
List of Publications during PhD .....	8
Chapter 1: Architecture and operating principles of the RuvAB Holliday junction branch migration complex .....	10
Supplementary Information for Chapter 1 .....	58
Chapter 2: Cryo-EM structure of pleconaril-resistant rhinovirus-B5 complexed to the antiviral OBR-5-340 reveals unexpected binding site .....	93
Supplementary Information for Chapter 2 .....	123
Concluding thoughts and future challenges .....	140
Abbreviations .....	142
References .....	143

## Preamble

Before the humankind developed the very first simple machines to gain mechanical advantage, each living organism and every single cell were using molecular machines to perform tasks essential for life such as replication and repair of DNA or ATP synthesis. In simplified manner, molecular machines perform an intricate task of transforming energy into the useful work. Molecular machines are of various design and composes of proteins, nucleic acids or carbohydrates with size ranges from few kDa to several MDa and are present through all cell compartments as well as in the extracellular matrix<sup>1-5</sup>. Complex molecular machines often compose of many “parts”, which must act together in an orchestrated and synchronized way to accomplish the main task. To ensure their correct performance, molecular motors are regulated by additional factors that enhance or suppress their activity (typically interaction proteins or small molecules). Unfortunately, structural characterization of fully assembled molecular machines is often due to their complexity and conformational flexibility an extremely difficult task and thus often only isolated sub-structures are subjected for structure determination. Thanks to the tremendous improvements in structural determination methods in the last decade (especially cryo-EM) blueprints of many fully or partially assembled molecular machines are not mystery anymore<sup>6-34</sup>. However, for the understanding of the functional details and interplay of all components, resolving key intermediate states is necessary for unambiguously defining the detailed mechanisms.

First chapter of my PhD thesis describes the dynamic structure and mechanism of substrate translocation of an active branch migration motor complexed to the four-way DNA called Holliday junction – a key intermediate during DNA recombination<sup>35,36</sup>. In course of homologous recombination of genetic material as well as DNA repair, ATP driven branch migration is executed by the conserved RuvAB complex in prokaryotes<sup>37-44</sup>. Although RuvAB complex served in the last decades as a paradigm for branch migration, the mechanical aspects of DNA translocation resulting in branch migration are still unknown<sup>45</sup>. In this study, we *in-vitro* assembled the bacterial RuvAB branch migration complex, slowed down the kinetic of branch migration reaction and determined the structures of multiple intermediate states at resolutions between 2.9 to 3.3 Å using cryo-EM. We show that within the RuvAB branch migration complex, substrate translocation and

ATP hydrolysis are directly coupled and driven by a series of allosterically coordinated conformational changes. Consequently, RuvB motors are observed to pull the DNA from the Holliday junction crossover in a lever-like mechanism. The herewith presented results uncover the conformational landscape required for the hydrolytic cycle and the concerted DNA translocation event at unambiguous detail and define the mechanistic principles of DNA translocation during branch migration performed by the RuvAB complex. This establishes a structural framework to understand how hexameric AAA+ translocases cooperatively and efficiently utilize energy derived from continuous ATP hydrolysis for the generation of mechanical force. Moreover, RuvAB system is deeply conserved in bacteria and structural characterization of the key intermediate steps allows to design state-specific inhibitors that could trap the system and thus prevent DNA recombination<sup>46</sup> or DNA repair.

In contrast to the first chapter, where cryo-EM single particle approach was used to describe the conformational dynamics during branch migration, progressing hydrolytic cycle and substrate translocation, chapter two demonstrates the power of cryo-EM in drug research. Here I focus on structural determination of pleconaril-resistant Human rhinovirus in presence or absence of a bioavailable antiviral pyrazolopyrimidine molecule OBR-5-340 with shown *in vivo* activity. The human rhinoviruses (HRVs), discovered in the 1950s, are the most common viral infectious agents of upper respiratory tract infection and are the major cause of the common cold<sup>47-49</sup>. HRVs, members of the family *Picornaviridae* and genus *Enterovirus* are small (27nm), nonenveloped, positive-sense, single-stranded-RNA viruses. More than 160 rhinovirus (RV) types cause about a billion respiratory infections annually in the United States alone, contributing to influenza-like illness. The pyrazolopyrimidine OBR-5-340 capsid binder prevents conformational changes required for genome release. By using cryo-EM, we show that OBR-5-340 inhibits the naturally pleconaril-resistant RV-B5 by attaching close to the pocket entrance in a binding geometry different from that of most capsid binders. We found that OBR-5-340 attaches closer to the entrance of the pocket than most other capsid binders, whose viral complexes have been studied so far, showing only marginal overlaps of the attachment sites.

To summarize, this work presents two topics having high resolution cryo-EM and consequent single particle analysis in common. First, the use of cryo-EM (and massive data collection) allowed to study at high resolution fully assembled, active, structurally non-uniform and flexible RuvAB branch migration motor complexed to the Holliday junction. These results represent an important step in understanding of the generation and regulation of mechanical work fuelled ATP hydrolysis and performed by oligomeric AAA+ proteins. Second, the use of cryo-EM single particle analysis of homogeneous sample of viral capsids +/- the inhibitor to identify the drug binding site.

## List of Publications during PhD

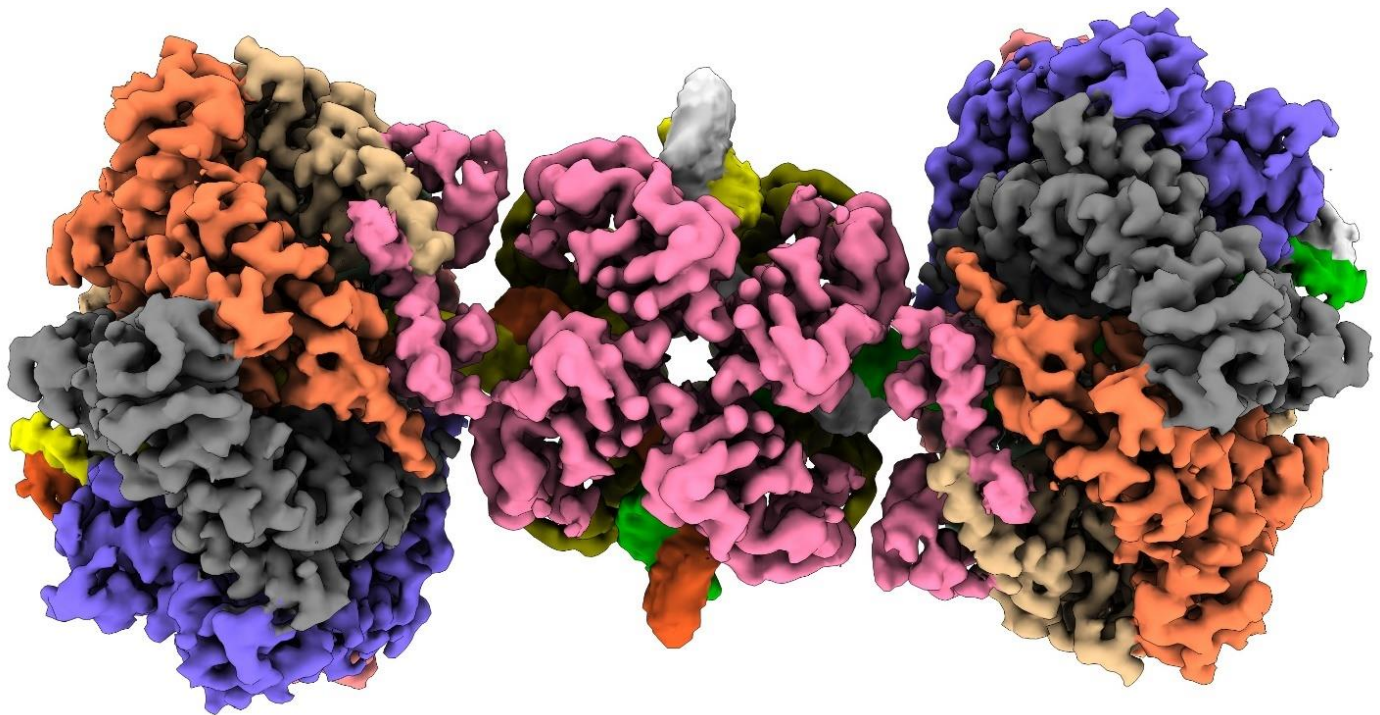
- 1) Architecture and operating principles of the RuvAB Holliday junction branch migration complex.  
**Wald J**<sup>1</sup>, Fahrenkamp D<sup>1</sup>, Gössweiner-Mohr N, Lugmayr W, Ciccarelli L, Vesper O and Marlovits TC<sup>1</sup> (manuscript submitted)  
<sup>1</sup> Corresponding authors
  
- 2) Cryo-EM structure of pleconaril-resistant rhinovirus-B5 complexed to the antiviral OBR-5-340 reveals unexpected binding site.  
**Wald J**\*, Pasin M\*, Richter M\*, Walther C\*, Mathai N, Kirchmair J, Makarov VA, Goessweiner-Mohr N, Marlovits TC, Zanella I, Real-Hohn A, Verdaguer N, Blaas D and Schmidtke M. PNAS USA. 2019 Sep 17;116(38):19109-19115. doi: 10.1073/pnas.1904732116. Epub 2019 Aug 28.  
\*Equal contributions
  
- 3) Substrate-engaged type III secretion system structures reveal gating mechanism for unfolded protein translocation.  
Miletic S\*, Fahrenkamp D\*, Goessweiner-Mohr N\*, **Wald J**\*, Pantel M, Vesper O, Kotov V and Marlovits TC. Nature Communication 12, 1546 (2021).  
<https://doi.org/10.1038/s41467-021-21143-1>  
\*Equal contributions
  
- 4) Structure and dynamics of the ESX-5 type VII secretion system of Mycobacterium tuberculosis.  
Bunduc C, Fahrenkamp D, **Wald J**, Ummels R, Houben E, Bitter W and Marlovits TC. Nature. 2021 May 12. doi: 10.1038/s41586-021-03517-z

- 5) Structural basis for peptide and drug uptake in mammals by the solute carriers PepT1 and PepT2.  
Killer M, **Wald J**, Pieprzyk J, Marlovits TC and Löw C. (accepted in Science Advances)
- 6) In-depth interrogation of protein thermal unfolding data with MoltenProt.  
Kotov V, Mlynek G, Vesper O, Pletzer M, **Wald J**, Teixeira-Duarte CM, Celia H, Garcia-Alai M, Nussberger S, Buchanan SK, Morais-Cabral JH, Löw C, Djinovic-Carugo K and Marlovits TC. Protein Sci. 2021 Jan;30(1):201-217. doi: 10.1002/pro.3986. Epub 2020 Nov 21.
- 7) Salmonella-based platform for efficient delivery of functional binding proteins to the cytosol.  
Chabloz A, Schaefer JV, Kozieradzki I, Cronin SJF, Strebinger D, Macaluso F, **Wald J**, Rabbitts TH, Plückthun A, Marlovits TC and Penninger JM. Commun Biol. 2020 Jul 3;3(1):342. doi: 10.1038/s42003-020-1072-4.
- 8) Helical reconstruction of Salmonella and Shigella needle filaments attached to type 3 basal bodies.  
Kotov V, Lunelli M, **Wald J**, Marlovits TC and Kolbe M. Biochemistry and Biophysics Reports, 2021, ISSN 2405-5808, doi: 10.1016/j.bbrep.2021.101039.
- 9) Predominant biphenyl dioxygenase from legacy polychlorinated biphenyl (PCB)-contaminated soil serves for the degradation of flavonoids rather than PCBs.  
Suman J, Strejcek M, Zubrova A, Capek J, **Wald J**, Michalikova K, Hradilova M, Sredlova K, Cajthaml T and Uhlik O. (in revision Frontiers in Microbiology)
- 10) Structural dynamics of the functional nonameric Type III translocase export gate.  
Yuan B, Portaliou AG, Parakra R, Smit JH, **Wald J**, Li Y, Srinivasu B, Loos MS, Dhupar HS, Fahrenkamp D, Kalodimos CG, van Hoa FH, Cordes T, Karamanou S, Marlovits TC and Economou A. J. Mol. Biol. 167188, <https://doi.org/10.1016/j.jmb.2021.167188>.

**Chapter 1:**  
**Architecture and operating principles of the RuvAB Holliday  
junction branch migration complex**

*Manuscript submitted for review, August 2021*

Jiri Wald, Dirk Fahrenkamp, Nikolaus Gössweiner-Mohr, Wolfgang Lugmayr, Luciano Ciccarelli,  
Oliver Vesper, and Thomas C. Marlovits



# Architecture and operating principles of the RuvAB Holliday junction branch migration complex

Jiri Wald\*<sup>1,2,3,4,5</sup>, Dirk Fahrenkamp\*<sup>1,2,3</sup>, Nikolaus Goessweiner-Mohr<sup>4,5</sup>, Wolfgang Lugmayr<sup>1,2,3,4,5</sup>, Luciano Ciccarelli<sup>4,5</sup>, Oliver Vesper<sup>1,2,3,4,5</sup>, and Thomas C. Marlovits<sup>#1,2,3,4,5</sup>

1. Centre for Structural Systems Biology, Notkestraße 85, 22607 Hamburg, Germany
2. Institute of Structural and Systems Biology, University Medical Center Hamburg-Eppendorf, 10 Notkestraße 85, 22607 Hamburg, Germany
3. Deutsches Elektronen Synchrotron (DESY), Notkestraße 85, 22607 Hamburg, Germany
4. Institute of Molecular Biotechnology GmbH (IMBA), Austrian Academy of Sciences, Dr. Bohr-Gasse 5, A-1030 Vienna, Austria
5. Research Institute of Molecular Pathology (IMP), Campus-Vienna-Biocenter 1, A-1030 Vienna, Austria

\* Corresponding authors

# Lead corresponding author

*Present address:*

NGM: Institute of Biophysics, Johannes Kepler University (JKU), Gruberstraße 40, 4020 Linz, Austria

## Keywords

RuvAB, branch migration, Holliday junction, cryo electron microscopy, DNA recombination, AAA+, DNA translocation

## Acknowledgements

We thank all current and former members of the Marlovits laboratory for their support in this project. We thank Steven C. West (The Francis Crick Institute) for critical suggestions on the initial design of the study and for kindly providing purified RuvA and RuvB proteins (*E. coli*), which served as positive controls in our early experiments. High performance computing was possible through access to the HPC at DESY/Hamburg (Germany) and Vienna Scientific Cluster (Austria). Cryo-EM optimizations and initial data collection were performed at the VBC EM facility. We would like to thank especially Harald Kotisch and Tom Heuser from the VBC EM facility for their support during initial cryo-EM sample preparation. We would also like to thank Mike Strauss (McGill University) for helpful suggestions to improve cryoEM sample preparation. Final cryo-EM data collections were performed at the Cryo-EM Facility at CSSB Hamburg (supported by the University of Hamburg, the University Medical Center Hamburg–Eppendorf and DFG grant numbers INST152/772-1, 152/774-1, 152/775-1, 152/776-1 and 152/777-1 FUGG.). We would like to thank Frank DiMaio (University of Washington) for his help with Rosetta (StarMap) and Tristan I. Croll (University of Cambridge) for providing additional support for ISOLDE. We thank Kai Karius (EMBL, Hamburg) for his help with the initial model of the Holliday junction and Holger Sondermann for critical input to the final manuscript. This project was supported by funds available to T.C.M. through the Behörde für Wissenschaft, Forschung und Gleichstellung of the city of Hamburg at the Institute of Structural and Systems Biology at the University Medical Center Hamburg–Eppendorf (UKE), the Institute for Molecular Biotechnology (IMBA) of the Austrian Academy of Sciences, and the Research Institute of Molecular Pathology (IMP). The laboratory of T.C.M. is supported by DESY (German Electron Synchrotron Center).

## **Author contributions**

JW – designed the experiments, generated constructs, expressed and purified proteins, performed biochemical assays and assembled complexes, performed negative stain EM screenings, optimized vitrification, collected and processed all cryo-EM data, prepared the figures.

DF, NGM, JW – built atomic models.

JW, DF, NGM, TCM – interpreted data.

WL – implemented and adjusted scripts for HPC.

JW, DF, TCM - conceptualized data and wrote manuscript.

JW, DF, TCM, LC, OV - data visualization. all authors – read, corrected, approved manuscript.

TCM – supervised project

## Abstract

The Holliday junction (HJ) is a key intermediate structure formed during DNA recombination across all kingdoms of life. In bacteria, the HJ is processed by two homohexameric RuvB motors, belonging to the AAA+-ATPase family, which assemble around the RuvA-HJ complex to energize the strand exchange reaction. Despite its importance for chromosome maintenance, the structure and the mechanism by which this complex facilitates branch migration are unknown. Here, using time-resolved cryo-EM, we obtained structures of the ATP-hydrolysing RuvAB complex in seven distinct conformational states at 2.9-3.4 Å resolution, captured during assembly and processing of a HJ. Five structures together resolve the complete ATP hydrolysis cycle of the RuvB motor and reveal the spatiotemporal relationship between ATP hydrolysis, nucleotide exchange and conformational changes in RuvB. We show how coordinated motions in a so called *converter* module, formed by DNA-disengaged RuvB protomers, stimulate ATP hydrolysis and nucleotide exchange. Immobilization of this module enables RuvB hexamers to convert the ATP-contained energy into a lever motion, which generates the pulling force driving the strand exchange reaction. We show structurally that the ATP hydrolysis cycle progresses around the ring, that RuvB motors rotate together with the DNA substrate and that the integration of both processes forms the mechanistic basis for DNA recombination by continuous branch migration. Taken together, our data decipher the molecular principles of homologous recombination by the RuvAB-HJ machinery, outline how hexameric AAA+ motors can generate mechanical force and provide a blueprint for the design of state-specific compounds targeting AAA+ motors.

## Main

Homologous recombination is a fundamental cellular process involved in the maintenance of genetic integrity and the generation of genetic diversity across all domains of life. The central and universal element of this process is a four-way DNA heteroduplex called Holliday junction (HJ)<sup>1</sup>. In prokaryotes, the two proteins RuvA and RuvB play critical roles in the processing of the HJ by promoting the ATP-dependent unidirectional strand exchange reaction known as active branch migration<sup>2-11</sup>.

Prior biochemical and structural evidence suggests that branch migration is facilitated by a tripartite complex. One or two RuvA tetramers assemble around the HJ crossover flanked by two hexameric RuvB AAA+ (ATPase associated with various cellular activities) motors, that together fuel the translocation of the newly-emerged recombined DNA<sup>12-21</sup>. Previous studies further established that the third domain of RuvA (RuvA<sup>D3</sup>) regulates branch migration through binding to the presensor-1  $\beta$ -hairpin (ps1 $\beta$ h) of RuvB, which is also consistent with the observation that RuvA<sup>D3</sup> increases the ATPase activity of the RuvB motor<sup>20,22</sup>. However, despite these developments, the structure of the RuvAB-HJ branch migration complex and the molecular mechanisms by which their AAA+ motors drive the translocation of DNA to facilitate one of the most basic biological processes in living organisms, the maintenance and exchange of genetic information, remain elusive<sup>23,24</sup>.

To unravel the architecture and decipher the operating principles of the RuvAB-HJ machinery, we performed time-resolved cryo-EM and single particle analysis of *in-vitro* reconstituted RuvAB complexes, processing a HJ. Our analyses reveal the structural landscape of an active RuvAB-HJ branch migration complex and uncover the highly dynamic interplay between a completely resolved ATP hydrolysis cycle in a rotating RuvB AAA+ motor and DNA translocation. Furthermore, we show that RuvB motors function as molecular levers that utilize the energy contained in ATP to produce a powerstroke in order to translocate their DNA.

## Results

### Quaternary structure and dynamics of the HJ-engaged RuvAB complex

Branch migration is a fast and highly dynamic action<sup>25</sup>. To allow the observation of distinct steps within this process, we performed time-resolved cryo-EM on RuvAB-HJ complexes with slowed-down kinetics. For this, we *in vitro* reconstituted active RuvAB-HJ complexes by mixing RuvA, RuvB and a synthetic HJ, containing a heterologous core, with an equimolar ratio of ATP $\gamma$ S and ADP. Prior to vitrification and cryo-EM, the reaction was incubated on ice to allow limited hydrolysis, for either 30 minutes (dataset t1, discussed later) or 5 hours (dataset t2, discussed below). (Extended Data Fig. 1). Single particle analysis revealed linearly arranged bipartite and tripartite assemblies with eight RuvA molecules (two tetramers) and the four-way HJ flanked by and flexibly connected to one or two RuvB hexamers, respectively (Fig.1, Extended Data Fig. 2). This architecture is consistent with previously proposed models of the RuvAB-HJ machinery<sup>12,13,16,20</sup>. In both particle types, DNA enters and leaves the RuvA core as a double helix with RuvB motors engaging the minor groove of the rejoined DNA (Fig, 1a-b, Extended Data Fig. 12). The RuvA core is physically connected to both RuvB motors through RuvA domain III (RuvA<sup>D3</sup>)<sup>20,26,27</sup>. Interestingly, up to two RuvA<sup>D3</sup> domains are bound to adjacently positioned RuvB protomers, indicating that these domains cooperate to control the RuvB motors (Fig. 1d, Extended Data Fig. 10). Moreover, all four RuvB-coordinating RuvA<sup>D3</sup> domains localize to the same side of the HJ crossover, implying that a single RuvA tetramer might be sufficient to operate both RuvB motors simultaneously. This is also in agreement with the proposed architecture of the RuvABC-HJ resolvosome, in which the HJ is suggested to be sandwiched by one RuvA tetramer and a RuvC resolvase dimer<sup>23,28</sup> (Extended Data Fig. 10c).

To further characterize the flexibility of RuvAB-HJ complexes, we subjected our particles to further 3D classifications. This analysis revealed that, besides the overall flexibility (Fig. 1f), in ~7% of the bipartite and 6% of the tripartite particles, the RuvB motor and its DNA underwent a counterclockwise rotation by ~60° with respect to the RuvA-HJ complex (Fig. 1c). Thus, at the end of the rotation, each RuvB protomer takes the position its neighbor had occupied before the motion

started (Fig. 1c Extended Data Fig. 8, movie 1). The rotation is further evidenced in multibody refinement analysis in which it accounts for ~45% of the total flexibility in the particles (Extended Data Fig. 9, movie 2). Taken together, we reasoned that reconstituted RuvAB-HJ complexes have been imaged in active states (Extended Data Fig. 1d). Moreover, our data reveal that the previously described continuous rotation of the DNA leaving the RuvB motors is accompanied by a concomitant rotation of the motors themselves<sup>29</sup>.

### **Structure and conformational landscape of RuvB AAA+ motors**

To understand how the hexameric RuvB rotary motion is linked to branch migration in the entire RuvAB-HJ machinery, we applied iterative focused refinements together with rigorous 3D classifications to the RuvB hexamers in our t2 dataset. This analysis revealed nine structurally distinct RuvB motor maps at resolutions ranging between 2.9 and 4.1 Å. Two of these could not be improved to a resolution that would allow unambiguous assignment of nucleotides and were therefore not considered further (Extended Data Fig. 4, 7e-m, Table 1). The remaining seven RuvB motors can be grouped according to the number of bound RuvA<sup>D3</sup> domains with one state lacking RuvA<sup>D3</sup> (s0<sub>t2</sub><sup>-A</sup>), two states containing one RuvA<sup>D3</sup> (s0<sub>t2</sub><sup>+A</sup>, s1<sub>t2</sub>) and four states accommodating two RuvA<sup>D3</sup> (s2<sub>t2</sub>-s5<sub>t2</sub>), together suggesting a dynamic interplay between RuvA<sup>D3</sup> and the RuvB motors (Extended Data Fig. 4, 18a).

All RuvB motors assemble into closed asymmetric hexamers, featuring a ~2 nm-wide central pore that accommodates the DNA (Fig. 1b, Extended Data Fig. 11d). Consistent with interaction studies, RuvB oligomerization is driven by the large (RuvB<sup>L</sup>) and small (RuvB<sup>S</sup>) ATPase subdomains of adjacent protomers<sup>17,30</sup>. Akin to other translocases<sup>31-36</sup>, four RuvB protomers together assemble into a spiral staircase, hereafter referred to as RuvB<sub>1-4</sub> from the top to the bottom of the staircase. This generates a continuous interface that primarily binds one of the two DNA strands. As such, one strand from each dsDNA entering the RuvA core is processed by one RuvB motor (Extended Data Fig 12). The two remaining two RuvB protomers, hereafter referred to as RuvB<sub>5+6</sub>, close the spiral staircase but do not bind the DNA (Fig. 2a-b). RuvB<sub>1-4</sub> bind

the DNA through their C-terminal head domains (RuvB<sup>H</sup>). Each RuvB<sup>H</sup> domain harbors four conserved arginine residues (Arg291, Arg310, Arg312 and Arg315) that, together, render the binding interface positively charged. Of these residues, Arg315 establishes electrostatic interactions with the phosphate backbone of every second nucleotide, indicating that one translocation step corresponds to the movement of two base pairs in the RuvB motor (Fig. 2c,e, Extended Data Fig. 12). Moreover, as RuvB protomers are positioned  $\sim 60^\circ$  apart from each other in the RuvB hexamer, this data further implies that the RuvB motor rotation is linked to the events occurring within one translocation step.

Variance analysis of the five states  $s_{1t2}$  to  $s_{5t2}$  ( $s_{0t2}^{-A}$  and  $s_{0t2}^{+A}$  will be introduced later) divided the RuvB hexamer into a rigid and a flexible region. The rigid area contains RuvB<sub>2+3</sub>, while RuvB<sub>5+6</sub> reside in the flexible part (Fig. 2d). Interestingly, DNA-bound RuvB<sub>1</sub> and RuvB<sub>4</sub>, which connect the two unequal halves at the top and at the bottom of the staircase, respectively, display a marked increase in variance, suggesting that motions in these border protomers contribute to RuvAB-mediated branch migration (Fig. 2d). To further assess the plasticity of individual RuvB protomers, we first extracted RuvB<sup>L</sup>, RuvB<sup>S</sup> and RuvB<sup>H</sup> and then superimposed the individual domains from all thirty RuvB protomers ( $s_{1t2}$ - $s_{5t2}$ ). This analysis revealed a very low average root mean square deviation (rmsd<sub>0</sub>: 0.55 Å, 0.49 Å and 0.40 Å) for each domain (Extended Data Fig. 13a). Superposition of individual protomers further revealed that those which occupy the same position, with respect to the DNA, group into distinct conformational clusters. These are hereafter referred to as clusters A-F, with cluster A corresponding to the position of RuvB<sub>1</sub>, cluster B with the position of RuvB<sub>2</sub>, etc.). Taken together, our data demonstrates that the plasticity of RuvB protomers is confined by their position in the hexamer (Fig. 2f, Extended Data Fig. 13b).

Furthermore, the observed changes in variance originate from RuvB domains that move as rigid entities, whereas interdomain linkers function as hinges to facilitate intra- and interprotomer signaling.

To characterize the intraprotomer plasticity even further, we measured two dihedral angles (d1 between RuvB<sup>L</sup> and RuvB<sup>S</sup>, and d2 between RuvB<sup>S</sup> and RuvB<sup>H</sup>) and one triangle angle, the

latter of which provides a more holistic view on the changes occurring within individual protomers (Fig. 3a, Extended Fig. 13c). Consistent with the superposition analysis, each cluster is characterized by a unique combination of the three angles and, thus, harbors a set of RuvB protomers with more similar conformations. Intriguingly, RuvB protomers are also subject to deformation within their clusters and are most variable in cluster E, in which the triangle angle of RuvB<sub>5</sub> covers a dynamic range of 5.6° (Fig. 3a, Extended Data Fig. 13c). We then aligned the five RuvB motor states (s1<sub>t2</sub>-s5<sub>t2</sub>) to almost invariant RuvB<sub>3</sub> in cluster C and analyzed the motions of all protomers from state to state (Extended Data Fig. 14). This approach revealed that the conformational changes of RuvB<sub>5</sub> in cluster E describe a trajectory with an average length of ~7 Å (range: ~6-10 Å) and which is directed downwards with respect to the DNA (Fig. 3b, Extended Fig. 14c). As the length of the trajectory corresponds well to the distance between three base pairs (Fig. 2a), our five structures likely represent consecutive atomic snapshots of an active RuvB motor that progresses through one translocation step of two base pairs. Moreover, the downwards-oriented movement causes the RuvB<sub>5</sub><sup>H</sup> domain to come closer to the minor groove of the DNA, while also approaching the height of RuvB<sub>4</sub> (Extended Data Fig. 14e). This suggests that the observed plasticity functions to prime RuvB<sub>5</sub> to inherit the position (bottom of the staircase), cluster (cluster D) and function (DNA binding) of RuvB<sub>4</sub>.

### **Coexisting nucleotides link the hydrolytic cycle with conformational states**

To investigate the interdependency between the observed conformational changes in RuvB hexamers and ATP hydrolysis, we analyzed the cryo-EM density corresponding to nucleotides in all thirty nucleotide binding pockets (NBPs) (Fig. 3c, Extended Data Fig. 15). This analysis revealed that DNA-bound RuvB<sub>2-3</sub> in clusters B and C are complexed with ATPγS, while RuvB<sub>5-6</sub> in clusters E and F are exclusively bound to ADP. In contrast, RuvB<sub>1</sub> in cluster A, located at the top of the staircase, can either be found in ATPγS (s1<sub>t2</sub>, s2<sub>t2</sub>), ADP+Mg<sup>2+</sup> (s3<sub>t2</sub>) or ADP (s4<sub>t2</sub>, s5<sub>t2</sub>) configuration, which is consistent with a progressing ATP hydrolysis reaction in this NBP. On the lower end of the staircase, RuvB<sub>4</sub> protomers in cluster D contain either ATPγS (s1<sub>t2</sub>), ADP (s5<sub>t2</sub>), or density that shows remote similarity to nucleotides only at high map thresholds (s2<sub>t2</sub>-s4<sub>t2</sub>).

Taking this into consideration, we regard RuvB<sub>4</sub> to be in an APO-like configuration in these states. Ordering the states according to the progressing hydrolysis reaction ( $\text{ATP} \rightarrow \text{ADP} + \text{Mg}^{2+} \rightarrow \text{ADP}$ ) in cluster A and taking into account the chronology of the nucleotide exchange event ( $\text{ADP} \rightarrow \text{APO} \rightarrow \text{ATP}$ ) in cluster D revealed that the sequence of states  $s_{1_{12}} \rightarrow s_{5_{12}}$  gives rise to a complete ATP hydrolysis cycle, which comprises the completion of the ATP hydrolysis reaction in cluster A and the exchange of ADP by ATP in cluster D (Fig. 3c-d). As this causes the ATP configuration to change from RuvB<sub>1-3</sub> to RuvB<sub>2-4</sub>, our structures establish experimentally that the ATP hydrolysis cycle operates around the ring in RuvB motors. Strikingly, the same order of events ( $s_{1_{12}}-s_{5_{12}}$ ) also produces the downward movement of RuvB<sub>5</sub> in cluster E (Fig. 3a-b) providing direct structural evidence that RuvB hexamers couple the ATP hydrolysis cycle to intra- and interprotomer signaling. Remarkably, the DNA remains bound to protomers 1-4 in clusters A-D across all five states and, therefore, the interaction with the staircase RuvB protomers is not strictly dependent on the nucleotide configuration of RuvB<sub>1</sub> and RuvB<sub>4</sub>. Consequently, the observed co-existing nucleotide configurations further corroborate the motion of RuvB<sub>5</sub> (cluster E) in that the ATP hydrolysis cycle functions to prime RuvB protomers to assume the conformations of their respective counterclockwise-adjacent clusters, a process which we will hereafter refer to as *cluster switch*. As the *cluster switch* causes the DNA binding interface (clusters A-D) and, thus, the DNA to relocate from RuvB<sub>1-4</sub> to RuvB<sub>2-5</sub> (RuvB<sub>1</sub> enters cluster F, whereas RuvB<sub>5</sub> enters cluster D), its occurrence marks the transition into the next ATP hydrolysis cycle.

In summary, our findings reveal two processes that operate in opposite directions. First, RuvB motors undergo a continuous counterclockwise rotation together with their DNA, causing individual protomers to change their position by  $\sim 60^\circ$  with every translocation step. Second, within one translocation step, the ATP hydrolysis cycle sustains conformational changes in and between RuvB protomers, which culminate in a *cluster switch* that progresses in the opposite direction through the RuvB motor (e.g. RuvB<sub>5</sub> enters cluster D, RuvB<sub>1</sub> enters cluster F, etc.). The integration of both events results in the conformational clusters (A-F), but not the protomers (RuvB<sub>1-6</sub>), to be maintained in a fixed position relative to the DNA and the central RuvA-HJ complex (Fig. 3e, Extended Data Fig. 16a). Importantly, the rotation of the RuvB hexamer further implies that the RuvA<sup>D3</sup> domains are subject to constant release and binding events during branch migration.

## NBP reorganization triggers ATP hydrolysis in cluster A

Nucleotide binding by RuvB is accomplished by a composite interface, which is composed of both ATPase subdomains together with the RuvB<sup>L</sup> domain of the counterclockwise-adjacent RuvB protomer (Extended Data Fig. 11c-d). To understand the molecular mechanisms coupling ATP hydrolysis and signal transduction, we followed the fate of ATP before (s1<sub>t2</sub>), during (s2<sub>t2</sub>) and after (s3<sub>t2</sub>-s5<sub>t2</sub>) hydrolysis in RuvB<sub>1</sub> of cluster A, whose NBP interfaces with DNA-disengaged RuvB<sub>6</sub> in cluster F.

In all ATP-containing NBPs, a conserved Walker-A motif binds the ATP-Mg<sup>2+</sup> complex in which previously identified Lys65 interacts with the ATP  $\gamma$ -phosphate<sup>37</sup>, while Thr66 coordinates the Mg<sup>2+</sup> ion. Additional contacts are provided by the two *cis*-acting arginine fingers, Arg21 and Arg218, which bind the ATP  $\alpha$ - and  $\gamma$ -phosphate, respectively. ATP-Mg<sup>2+</sup> *trans*-sensing is achieved by two elements: a conserved signature motif (127-Glu-Asp-130), located on alpha helix  $\alpha$ 4 and *trans*-acting Arg171 on alpha helix  $\alpha$ 5. *Trans*-Glu128 in the signature motif stabilizes *cis*-Arg21 and *cis*-Arg218, while *trans*-Asp129 senses *cis*-Arg21 only. Hence, both acidic residues contribute to the binding of the ATP-Mg<sup>2+</sup> complex indirectly. In contrast, *trans*-Arg171 binds the  $\gamma$ -phosphate and, hence, directly coordinates ATP (Fig. 3f).

During the transition through different states (s1<sub>t2</sub>→s5<sub>t2</sub>), RuvB<sub>6</sub> alpha helices  $\alpha$ 4 and  $\alpha$ 5 undergo a concerted motion, which enables distinct local rearrangements of *trans*-residues critical for ATP hydrolysis in the RuvB<sub>1</sub> NBP (Fig. 3g). In particular, the intermolecular interaction between *trans*-Glu128 and *cis*-Arg21, which is maintained in state s1<sub>t2</sub>, is lost in the following states, enabling *trans*-Glu128 to instead engage with *trans*-Arg171. Further, in s2<sub>t2</sub>, *trans*-Tyr131 joins *cis*-Arg21 in coordinating *trans*-Asp129, an event that coincides with the appearance of continuous EM density between *trans*-Asp129 and the ATP-Mg<sup>2+</sup> complex (Fig. 3h, Extended Data Fig. 17a). The connecting density likely corresponds to ordered water molecules, which are required to facilitate the nucleophilic attack on the ATP  $\gamma$ -phosphate (Fig. 3h). The importance of the signature motif has been highlighted by mutational studies in which the substitution of *trans*-Asp129 markedly compromised branch migration activity, whereas the mutation of *trans*-Glu128

resulted in a bacterial growth defect<sup>22</sup>. As an additional validation of the ATP hydrolysis reaction taking place in RuvB<sub>1</sub> of state  $s_{2t_2}$ , connecting EM density also emerges between the ATP  $\gamma$ -phosphate and *cis*-Asp110, which, like *trans*-Asp129, has been shown to be important for ATP hydrolysis<sup>38,39</sup>.

In the next states, progression of the ATP hydrolysis reaction can be observed, which first results in the release of the  $\gamma$ -phosphate ( $s_{2t_2} \rightarrow s_{3t_2}$ ) (Fig. 3d, Extended Data Fig. 15a). As a result, the binding of *cis*-Arg218 to the nucleotide is released, while the coordination of the Mg<sup>2+</sup> ion through *cis*-Thr66 remains intact. In the next transition ( $s_{3t_2} \rightarrow s_{4t_2}$ ), the Mg<sup>2+</sup> ion is lost, which completes the ATP hydrolysis reaction and causes *cis*-Thr66 to instead coordinate the ADP  $\beta$ -phosphate. Notably, the completion of the ATP hydrolysis reaction in state  $s_{4t_2}$  triggers a distinct motion of *cis*-Arg218 away from the RuvB<sub>1</sub> NBP, which coincides with a displacement of the entire RuvB<sub>1</sub><sup>S</sup> domain (Fig. 3h, Extended Data Fig. 17a). In turn, this motion translates into a 1 Å-long displacement of the RuvB<sub>1</sub><sup>H</sup> domain towards DNA-disengaged RuvB<sub>6</sub>, indicating that, within its conformational cluster A, ATP hydrolysis primes RuvB<sub>1</sub> for DNA release (Extended Data Fig. 14c-d). However, despite this motion, the RuvB<sub>1</sub><sup>H</sup> domain stays connected to the DNA, demonstrating that the presence of ADP in the RuvB<sub>1</sub> NBP is necessary but not sufficient to promote a *cluster switch*.

### **RuvA operates the ATP hydrolysis cycle**

One RuvA<sup>D3</sup> domain (hereafter referred to as RuvA<sub>1</sub><sup>D3</sup>) is bound to RuvB<sub>4</sub> during all five states ( $s_{1t_2} \rightarrow s_{5t_2}$ ), revealing that the RuvA-HJ complex is physically connected to both RuvB motors throughout the entire ATP hydrolysis cycle. In contrast, a second RuvA<sup>D3</sup> domain (hereafter referred to as RuvA<sub>2</sub><sup>D3</sup>) binds exclusively to RuvB<sub>5</sub> in the states  $s_{2t_2}$  to  $s_{5t_2}$  (Extended Data Fig. 18a). Both RuvA<sup>D3</sup> domains bind to a previously described hydrophobic composite interface in their respective RuvBs, which is composed of RuvB<sup>L</sup> alpha helix  $\alpha_3$  and the presensor-1  $\beta$  (ps1 $\beta$ ) hairpin (Extended Data Fig. 10,18a)<sup>15</sup>. Analyzing the impact of the RuvA<sub>2</sub><sup>D3</sup> recruitment ( $s_{1t_2} \rightarrow s_{2t_2}$ ) revealed that the binding event exerts a wedge-like effect on the RuvB hexamer, that drives apart the domain cores of RuvB<sub>5</sub><sup>L</sup> and RuvB<sub>4</sub><sup>L</sup>. The motion of RuvB<sub>5</sub> suggests that RuvA<sub>2</sub><sup>D3</sup>

binding is achieved by an induced-fit mechanism (Fig. 4b, Extended Data Fig. 14b-c, movie 3). The repositioning of RuvB<sub>5</sub> causes a concomitant motion of adjacent DNA-disengaged RuvB<sub>6</sub>, whose *trans*-acting residues Glu128, Asp129 and Arg171 facilitate the ATP hydrolysis reaction in RuvB<sub>1</sub> (Fig. 4c, Extended Data Fig. 14b-c, movie 4). Based on this observation, we postulate that RuvA<sub>2</sub><sup>D3</sup> acts as an ATPase-activating domain that stimulates ATP hydrolysis through long-range interprotomer signaling. At the same time, the displacement of RuvB<sub>4</sub><sup>L</sup> takes place, which promotes the opening of the RuvB<sub>4</sub> NBP and thereby enables the escape of the ADP molecule (Fig. 4d, Extended Data Fig. 18e, movie 5-6). Hence, our data reveal that RuvA<sub>2</sub><sup>D3</sup> also functions as a nucleotide exchange factor (NEF) for RuvB AAA+. Together, these findings establish that RuvA operates the ATP hydrolysis cycle in the RuvB motor through its RuvA<sub>2</sub><sup>D3</sup>. This is consistent with previous findings where the ATPase activity of RuvB increases in the presence of RuvA<sup>D3</sup><sup>40</sup>. Furthermore, as two RuvA<sup>D3</sup> domains are connected to each RuvB motor in fully assembled RuvAB-HJ complexes, our data indicate that the RuvA core complex contributes to the synchronization of the branch migration reaction by stimulating the ATP hydrolysis cycle in both RuvB hexamers. Interestingly, in other AAA+ hexameric translocases of the PS-I superclade, the ps1β hairpin either binds directly to the substrate<sup>41-45</sup>, or, alternatively, has been implicated in the coordination of substrate-interacting elements<sup>46-51</sup>. Hence, as the ps1β hairpin has been shown to be critically important for substrate translocation in all AAA+ motors of the PS I superclade, the regulation of the ATP hydrolysis cycle might be under the direct control of the substrate in these systems. In the following states (s2<sub>12</sub>→s4<sub>12</sub>), the ATP hydrolysis reaction proceeds in the RuvB<sub>1</sub> NBP. First, this results in the loss of the γ-phosphate (ADP+Mg<sup>2+</sup>) and only then in the dissociation of the Mg<sup>2+</sup> ion (ADP) (Extended Data Fig. 15a, 17a). Interestingly, the *trans*-acting residues of RuvB<sub>6</sub><sup>L</sup> disconnect from the nucleotide only upon loss of the Mg<sup>2+</sup> ion, which, in turn, permits a large-scale motion of RuvB<sub>6</sub> (Fig. 3g). Releasing RuvB<sub>6</sub><sup>L</sup> from its association with ADP sets in motion a chain reaction, which also affects the position of DNA-disengaged RuvB<sub>5</sub>. Hence, our data reveal that the dissociation of the Mg<sup>2+</sup> ion triggers retrograde interprotomer signaling (Fig. 4e-f, Extended Data Fig. 14b,17b,18c). As one of the consequences, gate-keeping *cis*-Arg21 of RuvB<sub>5</sub> can no longer coordinate the ADP α-phosphate in RuvB<sub>5</sub>, which, in turn, causes the entire N terminus to fold away from the RuvB<sub>5</sub> NBP (Fig. 4f). This prepares the RuvB<sub>5</sub> NBP for the release of ADP in the next translocation step, when RuvB<sub>5</sub> has transitioned into cluster D (*cluster*

*switch*) and undergoes nucleotide exchange. This is further reflected by a constantly increasing  $d_2$  angle in RuvB<sub>5</sub>, which, on a molecular level, weakens the hydrophobic interaction between N-terminal *cis*-Leu20 and its *cis* binding partners Thr193, Ile196, Phe197 and Asn221. As a result, the destabilization of *cis*-Leu20 impairs the ability of *cis*-Arg21 to coordinate the ADP  $\alpha$ -phosphate (Extended Data Fig. 18g, movie 3). In addition to RuvB<sub>5</sub>, the retrograde signaling cascade also affects RuvB<sub>4</sub> at the bottom of the staircase, which reaches the maximum opening of its NBP in state  $s_{4t_2}$ , demonstrating that nucleotide exchange evolves over three states ( $s_{2t_2} \rightarrow s_{4t_2}$ ). The acquisition of a new ATP molecule ( $s_{4t_2} \rightarrow s_{5t_2}$ ) is then accompanied by a concerted motion of RuvB<sub>6</sub>, RuvB<sub>5</sub> and RuvB<sub>4L</sub>. As a part of this motion, the coordination of the newly obtained ATP is restored by the RuvB<sub>4</sub> N-terminus in cluster D. Consequently, the gate-opening (cluster E) and gate-closing (cluster D) motions of the RuvB N-terminus serve as additional proof for the directionality of the ATP hydrolysis cycle. Finally, the retrograde signaling cascade causes RuvB<sub>4</sub><sup>L</sup> to become a part of the rigid area in the RuvB motor, which marks the completion of the ATP hydrolysis cycle (Fig. 4e, Extended Data Fig. 15b, 14a,b, 18f, movie 6).

Together, these findings establish that RuvB<sub>6</sub>, RuvB<sub>5</sub> and RuvB<sub>4L</sub> function as a RuvB motor-operating multi-domain module (hereafter referred to as *converter* module), which undergoes defined motions in the ATP hydrolysis cycle. The critical position of RuvB<sub>5</sub> in the center of the *converter* module enables the binding of RuvA<sub>2</sub><sup>D3</sup> to stimulate ATP hydrolysis (RuvB<sub>6</sub>) and nucleotide exchange (RuvB<sub>4</sub>) through interprotomer signaling.

### **RuvB motors facilitate branch migration by a lever-like mechanism**

We show that the completion of the ATP hydrolysis cycle ( $s_{1t_2}$ - $s_{5t_2}$ ) does not immediately result in a *cluster switch* and, hence, our data establish that the two events are separated in time. Importantly, the *cluster switch* repositions the RuvB hexamer on the DNA (RuvB motor “walking”) but as such does not exert a pulling force on the DNA (Fig. 5e, movie 7). Consequently, the *cluster switch* does not lead to strand exchange (branch migration) in the RuvA core. We therefore reasoned that the ATP hydrolysis cycle functions to produce the pulling force (*powerstroke*) that

is needed to promote branch migration (Fig. 5f). In addition, the RuvB motor is primed for a *cluster switch*. Notably, the *converter module* of the RuvB motor is subject to substantial conformational changes in the ATP hydrolysis cycle ( $s_{1t_2}$ - $s_{5t_2}$ ) that, together, describe a downwards-directed motion towards the RuvA-HJ core. Aligning the ATP hydrolysis cycle states ( $s_{1t_2}$ - $s_{5t_2}$ ) to RuvB<sub>5</sub> in the center of the *converter* module revealed that its trajectory translates into a lifting motion of the RuvB motor, in which the individual areas of the hexamer lift proportionally to their distance from RuvB<sub>5</sub> (Fig. 3b, 5a). This causes the DNA binding interface to be lifted by a height of  $\sim 7.0$  Å away from the RuvA-HJ core. As this distance corresponds to the translocation of two base pairs, our data provides evidence that RuvB motors act as molecular levers, which convert the energy obtained from ATP hydrolysis into a pulling force to physically move the DNA (RuvB motor “pulling”) and thereby achieve DNA recombination (Fig. 5b-c, movie 8-9). The largest conformational changes in the *converter* module of the RuvB motor are associated with the recruitment of RuvA<sub>2</sub><sup>D3</sup> ( $s_{1t_2}$ → $s_{2t_2}$ ) and the nucleotide exchange process ( $s_{4t_2}$ → $s_{5t_2}$ ), indicating that these two events contribute the most to DNA translocation (Extended Data Fig. 14b-c).

Consistently, motions that are associated with nucleotide exchange have recently also been proposed as a force-generating step in the AAA+ motor of the 26S proteasome<sup>52,53</sup>. Based on our findings, we posit that RuvA functions as a fulcrum, which enables RuvB motors to facilitate branch migration by producing a powerstroke that pulls the DNA through the RuvA core (Fig. 5c). Following the lever action, the RuvB hexamer performs a *cluster switch* to enable the motor to walk on the DNA. As this event also marks the transition into the next ATP hydrolysis cycle, the *cluster switch* enables RuvB motors to generate iterative powerstrokes and, thus, constitutes a mechanistic necessity for continuous branch migration. (Fig. 5g, Fig. 6, Extended Data Fig. 16b, movie 10).

### **Time-resolved cryo-EM reveals potential entry pathways into the hydrolytic cycle**

In addition to the RuvAB-HJ particles from which we obtained the ATP hydrolysis cycle states ( $s_{1t_2}$ - $s_{5t_2}$ ), our data also contained RuvB-HJ particles. Reconstruction of these particles gave

rise to a RuvA<sup>D3</sup>-free state  $s_{0t_2}^{-A}$ . Assessing the nucleotide configuration of state  $s_{0t_2}^{-A}$  showed that RuvB<sub>1-4</sub> are complexed with ATP $\gamma$ S, while RuvB<sub>5-6</sub> are bound to ADP (Extended Data Fig. 4,15a). Moreover, at high map thresholds, the density corresponding to the nucleotide in the RuvB<sub>6</sub> NBP shows remnants of the  $\gamma$ -phosphate as well as the Mg<sup>2+</sup> ion, suggesting that asymmetric RuvB motors may assemble with as many as five ATP-bound RuvB protomers (Extended Data Fig. 15a-b). Further, this indicates that ATP hydrolysis may not be restricted to the interface between clusters A and F but can eventually also be carried out by the two DNA-disengaged RuvB protomers in clusters F and E. Interestingly, a structurally highly similar state ( $s_{0t_2}^{+A}$ ) with identical nucleotide configuration could also be reconstructed from RuvAB-HJ particles (Fig. 5d, Extended Data Fig. 4,15a-b,19). Having previously established that ATP hydrolysis precedes the acquisition of a new ATP molecule in the ATP hydrolysis cycle, the simultaneous presence of ATP in cluster A (RuvB<sub>1</sub>) and cluster D (RuvB<sub>4</sub>) suggests that state  $s_{0t_2}^{+A}$  is not part of this cycle. We therefore refer to this state as an initiation state.

Comparing the *converter* module in state  $s_{0t_2}^{+A}$  with those in the ATP hydrolysis cycle states ( $s_{1t_2}$ - $s_{5t_2}$ ) revealed that the ATP hydrolysis interface (clusters A/F) displays highest similarity to the corresponding interface in state  $s_{1t_2}$ , whereas the nucleotide exchange interface (clusters D/C) is most similar to the one in state  $s_{5t_2}$  (Fig. 5d, Extended Data Fig. 19). Thus, when RuvB<sub>1</sub> and RuvB<sub>4</sub> both contain ATP, the *converter* module assumes a hybrid conformation, which is from any of the conformations seen in the ATP hydrolysis cycle. To substantiate these observations and investigate the initiation of the ATP hydrolysis cycle, we performed time-resolved cryo-EM on RuvAB-HJ particles that were incubated for 0.5 instead of 6 hours (dataset: t1) (Extended Data Fig. 1e). Strikingly, we could only reconstruct two states ( $s_{0t_1}^{+A}$ ,  $s_{1t_1}$ ) from this dataset, each of which yielded a map with a resolution of  $\sim 3.3$  Å. In both states, the RuvB motor is only connected to RuvA<sup>D3</sup>, providing evidence that i) the states  $s_{2t_2}$  to  $s_{5t_2}$  are actively generated by a slowly-progressing ATP hydrolysis cycle, ii) confirming that the RuvAB-HJ complexes (dataset: t2) were vitrified in the process of active branch migration and iii) suggesting that RuvA<sup>D3</sup> is involved in RuvB motor assembly. Consistently, state  $s_{0t_1}^{+A}$  is structurally highly similar to the initiation state  $s_{0t_2}^{+A}$  (Fig. 5d, Extended Data Fig. 19), but contains a fifth ATP molecule in RuvB<sub>6</sub>, indicating that  $s_{0t_2}^{+A}$  may indeed be derived from  $s_{0t_1}^{+A}$  through ATP

hydrolysis in RuvB<sub>6</sub>. (Extended Data Fig. 15a-b). Intriguingly, state s<sub>11</sub> shares high structural similarity and the nucleotide configuration with the ATP hydrolysis cycle state s<sub>12</sub>, indicating that the initiation states (s<sub>01</sub><sup>+A</sup>, s<sub>02</sub><sup>+A</sup>) and the ATP hydrolysis cycle states (s<sub>11</sub>, s<sub>12</sub>) represent two independent RuvB motor assembly pathways in our *in vitro* reconstitution experiment. However, given that ATP levels typically exceed those of ADP in bacterial cells, it appears likely that, *in vivo*, RuvB motors first assemble initiation states to then enter the ATP hydrolysis cycle (s<sub>0</sub>→s<sub>1</sub>) to promote processive branch migration.

## Discussion

Our work reveals the critical role for substrate-disengaged RuvB protomers, whose highly coordinated motions control the ATP hydrolysis cycle in the RuvB hexamer. These protomers are part of a so-called *converter* module through which the binding of RuvA<sup>D3</sup> can stimulate long-range interprotomer signaling, leading to ATP hydrolysis and nucleotide exchange. Interestingly, DNA-disengaged protomers are a unifying feature across most ring-forming AAA+ motors<sup>31,35,54</sup>, suggesting that variations of the *converter* module likely also operate other AAA+ ATPases. To be able to repeatedly exert their critical function on a rotating RuvB motor, RuvA<sup>D3</sup> domains need to constantly release from the RuvB hexamer and bind to newly generated binding interfaces that are produced by the ATP hydrolysis cycle. Although the driving force behind this rotation remains to be identified, it appears reasonable that the energy for this motion is derived from the ATP hydrolysis cycle. As the DNA substrate already refolds into double helix within the confinement of the RuvA core, we propose that the RuvB motor rotation is powered by the rewinding of the translocating DNA (movie 9).

With five distinctive states, our data establishes structurally that the ATP hydrolysis cycle progresses around the ring in RuvB motors, providing proof of concept for a believed-to-be conserved core mechanistic principle in the field of hexameric AAA+ translocases<sup>35</sup>. In the context of the RuvAB-HJ complex, the sequential ATP hydrolysis cycle of the rotating RuvB motor causes the *converter* module to be maintained in the same area with respect to the central RuvA complex.

As a result, a single RuvA tetramer could potentially control the ATP hydrolysis cycles in each of the two RuvB motors within the RuvAB-HJ machinery. In non-rotational AAA+ motors, sequential ATP hydrolysis events should cause the corresponding substrate-disengaged protomers to progress around the ring. To operate the ATP hydrolysis cycle in these motors, putative *converter* module-interactors must therefore be able to reach every protomer in the AAA+ motor, or, alternatively, the function of RuvA may be carried out directly by the substrate. This may provide a rationale as to why ring-shaped AAA+ motors are often found to be intimately embedded within multimeric scaffolds such as in the proteasome.

Further, we reveal that the ATP hydrolysis cycle is a spatiotemporal continuum of conformational changes through which RuvB motors convert the chemical energy retained in ATP into a lever-like action. The RuvA<sup>D3</sup>-bound protomers in the *converter* module are at the heart of this process as their physical connection to the RuvA complex generates the fulcrum that is needed to turn the RuvB motor into a molecular lever. Importantly, while the DNA is levered, it remains associated with its binding interface and, thus, our data allows us to decompose the lever action (during the ATP hydrolysis cycle) from the *cluster switch* (following the ATP hydrolysis cycle). This reveals that the ATP hydrolysis cycle serves to promote DNA pulling, while also priming the RuvB hexamer for a *cluster switch*. The latter event, which is not part of the ATP hydrolysis cycle, is critical for enabling the propagation of the ATP hydrolysis cycle around the ring and, consequently, for continuous DNA translocation (Fig. 6, Extended Data Fig. 16). Notably, hexameric nucleic acid as well as protein AAA+ translocases share a conserved asymmetric spiral organization around their cognate substrates and are furthermore believed to share a similar translocation rate per hydrolysed ATP molecule<sup>36,54–56</sup>.

Likewise, the pulling of DNA, RNA and protein substrates is thought to be powered by a common sequential ATP hydrolysis cycle<sup>31,53,57–60</sup>. Based on these shared geometrical and mechanistic properties, our findings suggests that not only RuvB motors but the majority of ring-shaped AAA+ motor translocases function as molecular levers, which convert the conformational changes associated with their ATP hydrolysis cycles into a defined lift-height of their central pores as a shared basic mechanism to facilitate substrate translocation.

Finally, our findings reveal that RuvB motors are most variable in the *converter* module, which changes from a hybrid conformation in the initiation states to the spatiotemporal continuum observed in the ATP hydrolysis cycle. As a functional DNA damage response allows intracellular bacterial pathogens to cope with the oxidative environment inside our cells, state-specific targeting of the *converter* module may thus provide a promising new avenue for the inhibition of RuvB motors and, hence, HR by small molecule interference.

## Glossary

*Cluster switch:* A *cluster switch* follows the ATP hydrolysis cycle in the RuvB hexamer and represents the moment when all RuvB subunits simultaneously undergo a register shift. When observing the RuvB hexamer from the top, *cluster switches* progress in clockwise direction. In practical terms this means that, following a register shift, the conformations that characterize the RuvB protomers in e.g. cluster A at the top of the staircase are no longer assumed by RuvB<sub>1</sub> but by RuvB<sub>2</sub>. As a consequence of the *cluster switch*, RuvB<sub>1</sub> assumes the conformations associated with cluster F.

*Converter module:* A multidomain module built by the protomers found in clusters F, E and the large ATPase domain of the protomer in cluster D, which functions to relay interprotomer signaling. Binding of RuvA<sub>2</sub><sup>D3</sup> to the protomer in cluster E of the *converter module* stimulates long-range interprotomer signaling, leading to ATP hydrolysis in cluster A via cluster F and nucleotide exchange in cluster D. Further, immobilization of the *converter module* protomer in cluster E turns the RuvB motor into a molecular lever. Hence, the name *converter module*.

*Substrate Rotation:* Being stably bound to the RuvB protomers in the clusters A-D, the substrate rotates together with the RuvB hexamer in the ATP hydrolysis cycle. Hence, from the perspective of conformational clusters, the DNA substrate rotates counterclockwise. In addition, the substrate is subject to an oscillating motion, which occurs as a result of the *cluster switch*, when the DNA is relocated from RuvB<sub>1-4</sub> to RuvB<sub>2-5</sub>.

*Powerstroke:* Lever-like motion of the RuvB motor, which is a consequence of the immobilization of the *converter module* protomer in cluster E by the RuvA<sup>D3</sup> domain. The powerstroke evolves over the five ATP hydrolysis states and causes substrate translocation in the RuvA core complex. From the perspective of the protomers in clusters B and C, substrate translocation is not noticeable, however from the perspective of substrate-disengaged protomers in clusters E and F the DNA substrate is translocated through the RuvB motor pore.

*ATP hydrolysis cycle:* The ATP hydrolysis cycle describes the conformational changes and events that are associated with a complete ATP hydrolysis reaction in cluster A and the successful exchange of the nucleotide in cluster D. ATP hydrolysis evolves over 4 states (s1<sub>t2</sub>-s4<sub>t2</sub>), while nucleotide exchange is facilitated over all five states. The ATP hydrolysis cycle maintains a constant ratio of 3 ATP versus 3 ADP molecules in the RuvB hexamer (s1<sub>t2</sub> vs. s5<sub>t2</sub>) and, thus, provides the mechanistic basis for continuous substrate translocation by sequential ATP hydrolysis events.

## References

1. Holliday, R. A mechanism for gene conversion in fungi. *Genetics Research* **5**, 282–304 (1964).
2. Otsuji, N., Iyehara, H. & Hideshima, Y. Isolation and Characterization of an Escherichia coli ruv Mutant Which Forms Nonseptate Filaments After Low Doses of Ultraviolet Light Irradiation. *Journal of Bacteriology* **117**, 337 (1974).
3. Shinagawa, H. *et al.* Structure and regulation of the Escherichia coli ruv operon involved in DNA repair and recombination. *Journal of Bacteriology* **170**, 4322 (1988).
4. Lloyd, R. G., Benson, F. E. & Shurvinton, C. E. Effect of ruv mutations on recombination and DNA repair in Escherichia coli K12. *Molecular and General Genetics MGG 1984 194:1* **194**, 303–309 (1984).
5. Shiba, T., Iwasaki, H., Nakata, a & Shinagawa, H. SOS-inducible DNA repair proteins, RuvA and RuvB, of Escherichia coli: functional interactions between RuvA and RuvB for ATP hydrolysis and renaturation of the cruciform structure in supercoiled DNA. *Proceedings of the National Academy of Sciences of the United States of America* **88**, 8445–8449 (1991).
6. Hiom, K. & West, S. C. Branch migration during homologous recombination: assembly of a RuvAB-holliday junction complex in vitro. *Cell* **80**, 787–793 (1995).
7. Iwasaki, H., Takahagi, M., Nakata, A. & Shinagawa, H. Escherichia coli RuvA and RuvB proteins specifically interact with Holliday junctions and promote branch migration. *Genes and Development* **6**, 2214–2220 (1992).
8. Tsaneva, I. R., Müller, B. & West, S. C. ATP-dependent branch migration of Holliday junctions promoted by the RuvA and RuvB proteins of E. coli. *Cell* **69**, 1171–1180 (1992).
9. Parsons, C. A., Tsaneva, I., Lloyd, R. G. & West, S. C. Interaction of Escherichia coli RuvA and RuvB proteins with synthetic Holliday junctions. *Proceedings of the National Academy of Sciences of the United States of America* **89**, 5452–5456 (1992).
10. Taylor, A. F. Movement and resolution of Holliday junctions by enzymes from E. coli. *Cell* **69**, 1063–1065 (1992).

11. Mitchell, A. H. & West, S. C. Hexameric Rings of Escherichia coli RuvB Protein.: Cooperative Assembly, Processivity and ATPase Activity. *Journal of Molecular Biology* **243**, 208–215 (1994).
12. Parsons, C. A., Stasiak, A., Bennett, R. J. & West, S. C. Structure of a multisubunit complex that promotes DNA branch migration. *Nature* **374**, 375–378 (1995).
13. Yu, X., West, S. C. & Egelman, E. H. Structure and subunit composition of the RuvAB-Holliday junction complex. *Journal of Molecular Biology* **266**, 217–222 (1997).
14. Rafferty, J. B. *et al.* Crystal Structure of DNA Recombination Protein RuvA and a Model for Its Binding to the Holliday Junction. *Science* **274**, 415–421 (1996).
15. Roe, S. M. *et al.* Crystal Structure of an Octameric RuvA–Holliday Junction Complex. *Molecular Cell* **2**, 361–372 (1998).
16. Mayanagi, K., Fujiwara, Y., Miyata, T. & Morikawa, K. Electron microscopic single particle analysis of a tetrameric RuvA/RuvB/Holliday junction DNA complex. *Biochemical and Biophysical Research Communications* **365**, 273–278 (2008).
17. Ohnishi, T., Hishida, T., Harada, Y., Iwasaki, H. & Shinagawa, H. Structure-function analysis of the three domains of RuvB DNA motor protein. *Journal of Biological Chemistry* **280**, 30504–30510 (2005).
18. Miyata, T. *et al.* Two different oligomeric states of the RuvB branch migration motor protein as revealed by electron microscopy. *Journal of Structural Biology* **131**, 83–89 (2000).
19. Nishino, T. *et al.* Modulation of RuvB function by the mobile domain III of the Holliday junction recognition protein RuvA. *Journal of Molecular Biology* **298**, 407–416 (2000).
20. Yamada, K. *et al.* Crystal structure of the RuvA-RuvB complex: A structural basis for the Holliday junction migrating motor machinery. *Molecular Cell* **10**, 671–681 (2002).
21. Ariyoshi, M., Nishino, T., Iwasaki, H., Shinagawa, H. & Morikawa, K. Crystal structure of the Holliday junction DNA in complex with a single RuvA tetramer. *Proceedings of the National Academy of Sciences of the United States of America* **97**, 8257–8262 (2000).
22. Han, Y. W. *et al.* A Unique  $\beta$ -Hairpin Protruding from AAA+ ATPase Domain of RuvB Motor Protein Is Involved in the Interaction with RuvA DNA Recognition Protein for Branch Migration of Holliday Junctions. *Journal of Biological Chemistry* **276**, 35024–35028 (2001).

23. Wyatt, H. D. M. & West, S. C. Holliday junction resolvases. *Cold Spring Harbor Perspectives in Biology* **6**, (2014).
24. Yamada, K., Ariyoshi, M. & Morikawa, K. Three-dimensional structural views of branch migration and resolution in DNA homologous recombination. *Current Opinion in Structural Biology* **14**, 130–137 (2004).
25. Liu, Y. & West, S. C. Happy Hollidays: 40th anniversary of the Holliday junction. *Nature Reviews Molecular Cell Biology* 2004 5:11 **5**, 937–944 (2004).
26. Nishino, T., Ariyoshi, M., Iwasaki, H., Shinagawa, H. & Morikawa, K. Functional analyses of the domain structure in the Holliday junction binding protein RuvA. *Structure* **6**, 11–21 (1998).
27. Han, Y. W. *et al.* A Unique  $\beta$ -Hairpin Protruding from AAA+ ATPase Domain of RuvB Motor Protein Is Involved in the Interaction with RuvA DNA Recognition Protein for Branch Migration of Holliday Junctions. *Journal of Biological Chemistry* **276**, 35024–35028 (2001).
28. van Gool, A. J., Hajibagheri, N. M. A., Stasiak, A. & West, S. C. Assembly of the Escherichia coli RuvABC resolvosome directs the orientation of Holliday junction resolution. *Genes and Development* **13**, 1861–1870 (1999).
29. Han, Y.-W. *et al.* Direct observation of DNA rotation during branch migration of Holliday junction DNA by Escherichia coli RuvA-RuvB protein complex. *Proceedings of the National Academy of Sciences* **103**, 11544–11548 (2006).
30. Yamada, K. *et al.* Crystal structure of the Holliday junction migration motor protein RuvB from Thermus thermophilus HB8. *Proceedings of the National Academy of Sciences* **98**, 1442–1447 (2001).
31. Gates, S. N. & Martin, A. Stairway to translocation: AAA+ motor structures reveal the mechanisms of ATP-dependent substrate translocation. *Protein Science* **29**, 407–419 (2020).
32. Enemark, E. J. & Joshua-Tor, L. Mechanism of DNA translocation in a replicative hexameric helicase. *Nature* **442**, 270–275 (2006).
33. Itsathitphaisarn, O., Wing, R. A., Eliason, W. K., Wang, J. & Steitz, T. A. The Hexameric Helicase DnaB Adopts a Nonplanar Conformation during Translocation. *Cell* **151**, 267–277 (2012).

34. Kelch, B. A., Makino, D. L., O'Donnell, M. & Kuriyan, J. How a DNA Polymerase Clamp Loader Opens a Sliding Clamp. *Science* **334**, 1675–1680 (2011).
35. Puchades, C., Sandate, C. R. & Lander, G. C. The molecular principles governing the activity and functional diversity of AAA+ proteins. *Nature Reviews Molecular Cell Biology* *2019 21:1* **21**, 43–58 (2019).
36. Nyquist, K. & Martin, A. Marching to the beat of the ring: polypeptide translocation by AAA+ proteases. *Trends in Biochemical Sciences* **39**, 53–60 (2014).
37. Hishida, T., Iwasaki, H., Yagi, T. & Shinagawa, H. Role of Walker Motif A of RuvB Protein in Promoting Branch Migration of Holliday Junctions. *Journal of Biological Chemistry* **274**, 25335–25342 (1999).
38. Iwasaki, H. *et al.* *Mutational analysis of the functional motifs of RuvB, an AAA 1 class helicase and motor protein for Holliday junction branch migration. Molecular Microbiology* vol. 36 (2000).
39. George, H., Mézard, C., Stasiak, A. & West, S. C. Helicase-defective RuvBD113E promotes RuvAB-mediated branch migration in Vitro. *Journal of Molecular Biology* **293**, 505–519 (1999).
40. Yamada, K., Fukuoh, A., Iwasaki, H. & Shinagawa, H. Novel properties of the *Thermus thermophilus* RuvB protein, which promotes branch migration of Holliday junctions. *Molecular and General Genetics MGG* *1999 261:6* **261**, 1001–1011 (1999).
41. Rzechorzek, N. J., Hardwick, S. W., Jatikusumo, V. A., Chirgadze, D. Y. & Pellegrini, L. CryoEM structures of human CMG–ATP $\gamma$ S–DNA and CMG–AND-1 complexes. *Nucleic Acids Research* **48**, 6980–6995 (2020).
42. Eickhoff, P. *et al.* Molecular Basis for ATP-Hydrolysis-Driven DNA Translocation by the CMG Helicase of the Eukaryotic Replisome. *Cell Reports* **28**, 2673-2688.e8 (2019).
43. Yuan, Z. *et al.* DNA unwinding mechanism of a eukaryotic replicative CMG helicase. *Nature Communications* *2020 11:1* **11**, 1–10 (2020).
44. Baretić, D. *et al.* Cryo-EM Structure of the Fork Protection Complex Bound to CMG at a Replication Fork. *Molecular Cell* **78**, 926-940.e13 (2020).

45. Meagher, M., Epling, L. B. & Enemark, E. J. DNA translocation mechanism of the MCM complex and implications for replication initiation. *Nature Communications* 2019 10:1 **10**, 1–13 (2019).
46. Ripstein, Z. A., Vahidi, S., Houry, W. A., Rubinstein, J. L. & Kay, L. E. A processive rotary mechanism couples substrate unfolding and proteolysis in the ClpXP degradation machinery. *eLife* **9**, (2020).
47. Fei, X. *et al.* Structures of the ATP-fueled ClpXP proteolytic machine bound to protein substrate. *eLife* **9**, (2020).
48. Lopez, K. E. *et al.* Conformational plasticity of the ClpAP AAA+ protease couples protein unfolding and proteolysis. *Nature Structural and Molecular Biology* **27**, 406–416 (2020).
49. Deville, C., Franke, K., Mogk, A., Bukau, B. & Saibil, H. R. Two-Step Activation Mechanism of the ClpB Disaggregase for Sequential Substrate Threading by the Main ATPase Motor. *Cell Reports* **27**, 3433-3446.e4 (2019).
50. Rizo, A. N. *et al.* Structural basis for substrate gripping and translocation by the ClpB AAA+ disaggregase. *Nature Communications* 2019 10:1 **10**, 1–12 (2019).
51. Gates, S. N. *et al.* Ratchet-like polypeptide translocation mechanism of the AAA+ disaggregase Hsp104. *Science* **357**, 273–279 (2017).
52. Dong, Y. *et al.* Cryo-EM structures and dynamics of substrate-engaged human 26S proteasome. *Nature* 2018 565:7737 **565**, 49–55 (2018).
53. Peña, A. H. de la, Goodall, E. A., Gates, S. N., Lander, G. C. & Martin, A. Substrate-engaged 26S proteasome structures reveal mechanisms for ATP-hydrolysis–driven translocation. *Science* **362**, (2018).
54. Jessop, M., Felix, J. & Gutsche, I. AAA+ ATPases: structural insertions under the magnifying glass. *Current Opinion in Structural Biology* **66**, 119–128 (2021).
55. O’Shea, V. L. & Berger, J. M. Loading strategies of ring-shaped nucleic acid translocases and helicases. *Current Opinion in Structural Biology* **25**, 16–24 (2014).
56. Seraphim, T. v. & Houry, W. A. AAA+ proteins. *Current Biology* **30**, R251–R257 (2020).
57. Dong, Y. *et al.* Cryo-EM structures and dynamics of substrate-engaged human 26S proteasome. *Nature* **565**, 49–55 (2019).
58. Tsai, F. T. & Hill, C. P. Same structure, different mechanisms? *eLife* **9**, (2020).

59. Glynn, S. E., Kardon, J. R., Mueller-Cajar, O. & Cho, C. AAA+ proteins: converging mechanisms, diverging functions. *Nature Structural & Molecular Biology* 2020 27:6 **27**, 515–518 (2020).
60. Miller, J. M. & Enemark, E. J. Fundamental Characteristics of AAA+ Protein Family Structure and Function. *Archaea* **2016**, (2016).

## Materials and Methods

### Protein engineering, expression and purification

RuvA from *Salmonella typhimurium* was fused to a C-terminal tetra-histidine tag and cloned into the pET-52b(+) expression vector (Novagen), using the NcoI and SacI restriction sites. Recombinant protein expression was performed in *E. coli* strain BL21(DE3). Bacterial cells were grown at 37°C in LB medium supplemented with 100 µg ml<sup>-1</sup> ampicillin to an optical density (OD) at 600 nm of about 0.6. Expression of RuvA was induced by the addition of 1 mM isopropyl β-D-1-thiogalactopyranoside (IPTG) and cultures were further incubated at 37°C for 3 hours. Cells were then pelleted at 4250 × g for 10 min at 4 °C, washed in 20 mM NaCl, 1 mM EDTA, 20 mM Tris-HCl pH 8 buffer (buffer 1), resuspended in 100 mM NaCl, 10% glycerol, 100 mM Tris-HCl pH 8 buffer (buffer 2) and stored at -80°C. For protein purification, the cell suspension was thawed, supplemented with a complete<sup>TM</sup> protease inhibitor cocktail (Sigma Aldrich), lysed by sonication and the resulting cell lysate was cleared by centrifugation (37,000 rpm, 1 h, 4°C). The supernatant was applied onto a 5 ml HisTrap column (GE Healthcare) equilibrated with buffer 2 and immobilized proteins were recovered by gradient elution using buffer 2 supplemented with 500 mM imidazole. Peak fractions were pooled, dialyzed against buffer 2 and loaded onto a Superdex 200 10/300GL size exclusion column (GE Healthcare) equilibrated in 100 mM NaCl, 1 mM EDTA, 0.5 mM DTT, 15% glycerol, 100 mM Tris-HCl pH 8 buffer (buffer 3). The peak fraction containing RuvA was collected, snap-frozen in liquid nitrogen and stored at -80°C. N-terminally truncated RuvB (16-333) from *Streptococcus thermophilus* was C-terminally fused to a tobacco etch virus (TEV) protease cleavage site, followed by a linker and a HA tag, and cloned into the pProEX HTB expression vector (ThermoFisher Scientific), using the NcoI and HindIII restriction sites. Recombinant protein expression was performed in *E. coli* strain BL21(DE3). Protein expression and purification were performed as described for RuvA. The TEV cleavage was performed during the dialysis step. The purity of recombinant RuvA and RuvB proteins was assessed by SDS-PAGE followed by staining with Coomassie R-250 and was estimated to be higher than >95% (Extended Data Fig. 1a-b).

## **DNA substrates**

Holliday junctions (HJ) with mobile (X26)<sup>1</sup> and immobile (Y2Ap modified from Y2A<sup>2</sup>) cores were prepared by annealing synthetic oligonucleotides (Sigma Aldrich) following the protocol provided in Table 4. In brief, the oligonucleotides were purified by agarose gel electrophoresis and mixed in appropriate ratios in 25 mM NaCl, 10 mM Tris-HCl pH 8 annealing buffer (buffer 4). The annealing reaction was performed in a 0.2 ml tube and covered with a thin layer of mineral oil to prevent water evaporation. The mixture was heated to 95°C for 10 min, and the temperature was subsequently decrease in 10 °C temperature steps every 10 minutes. To obtain homogenous four-way HJ preparations, the annealing reaction was supplemented with a DNA sample buffer (New England Biolabs) and separated by native PAGE. Bands corresponding to four-way HJs were cut out from the gel and eluted by incubation in 5 mM Tris-HCl pH 8. For DNA-binding and branch migration activity assays, one oligonucleotide strand was labelled with radioactive <sup>32</sup>P (3000 (Ci/mmol) at the 5' end prior to annealing.

## **RuvAB-HJ *in vitro* reconstitution**

RuvAB-HJ particles were reconstituted as discribed previously<sup>2</sup> with minor modifications: Purified HJ and RuvA were mixed and supplemented with 5 mM MgCl<sub>2</sub>. The mixture was incubated at 37°C for 30 minutes and applied to size exclusion chromatography on a Superdex 200 10/300GL column equilibrated with 100 mM NaCl, 2% glycerol and 5 mM MgCl<sub>2</sub>, 5 mM Tris-HCl pH 8 buffer (buffer 5). The peak fraction containing RuvA-HJ complexes was mixed with purified RuvB in the presence of 10 mM MgCl<sub>2</sub> and an equimolar ratio of ATPγS and ADP (1 mM). To form RuvAB-HJ complexes, the mixture was incubated at 37°C for 10 min and then cooled to 4°C. Prior to vitrification, all samples were analyzed for RuvAB-HJ complex formation by negative stain electron microscopy.

### **Branch migration activity assay**

Branch migration activity was measured as previously described<sup>3</sup>. Briefly, the branch migration reaction (20  $\mu$ l) contained various amounts of 5'-<sup>32</sup>P-labeled synthetic HJ-X26 and purified RuvA/RuvB proteins in 15mM MgCl<sub>2</sub>, 1mM DTT, 100  $\mu$ g/ml BSA, 2 mM ATP, Tris-HCl pH 8 buffer (buffer 6). Following an incubation at 37°C for 35 min, RuvA/RuvB proteins were digested by proteinase K treatment (2 mg/ml) and 0.5 % SDS at 37°C for 15 min. DNA sample buffer (New England Biolabs) was added to the reaction and branch migration was assayed by electrophoresis (4 °C at 135 V for 35 minutes, TAE buffer) in a 7.5 % polyacrylamide gel. Bands corresponding to HJ and HJ derivatives were visualized by autoradiography.

### **Electromobility shift gel assay (EMSA)**

Varying amounts of purified RuvA protein were incubated with 5'-<sup>32</sup>P-labeled synthetic Holliday junction HJ-Y2Ap for 30 min at 37 °C in 5mM EDTA, 1mM DTT, 100  $\mu$ g/ml BSA, 30mM Tris-HCl 8 buffer (buffer 7). DNA sample buffer (New England Biolabs) was added to the reaction and the complex formation was assayed by electrophoresis in a 6 % polyacrylamide gel (1x TAE). Electrophoresis was carried out at 4 °C at 150 V for 1.5 hour in a 0.5 x TAE buffer. Gels were dried, and DNA bands were visualized by autoradiography.

### **Negative staining EM**

Before sample application, grids were positively glow discharged for 30 sec. at 25 mA using a GloQube® Plus Glow Discharge System (Electron Microscopy Sciences). 4  $\mu$ l of freshly prepared RuvAB-HJ complexes were applied to carbon-coated copper grids and incubated for 30 seconds. The sample was blotted off, and then stained with 4  $\mu$ l of the staining solution (2 % Uranyl Acetate) for 30 sec. Excess stain was blotted off and the grids were air-dried for at least 2 min. Grids were imaged using a Thermo Fisher Scientific Talos L120C TEM with a 4K Ceta CEMOS camera.

## Cryo-EM sample preparation and data collection

Freshly *in-vitro* reconstituted RuvAB-HJ complexes were incubated on ice for 30 min (dataset: t1) or ~5 hours (dataset: t2) prior to vitrification. N-Dodecyl-beta-Maltoside (DDM) was added to a concentration of 0.005% prior to application of the protein sample to the grid. 4  $\mu\text{l}$  of the final RuvAB-HJ sample was applied twice onto glow-discharged (30 sec, 25 mA) gold Quantifoil grids (2/2 300 mesh) containing a thin layer (1 – 1.5 nm) of amorphous carbon (made in-house). In brief, after the first sample application at 4 °C for 1 min in a horizontal position, the liquid was blotted off from the side. The procedure was repeated and the sample was plunge-frozen into a propane/ethane mixture using a Vitrobot Mark V (Thermo Fisher Scientific) set to 100% humidity and 4°C. Blotting times ranged from 4-7 sec. Vitrified samples were imaged on a Thermo Fisher Scientific Titan Krios TEM operating at 300 kV, equipped with a field emission gun (XFEG) and a Gatan Bioquantum energy filter with slit of 10 eV (re-centered slit every 6 hours) and a Gatan K3 electron detector. For the t1 dataset, a total of 10057 micrographs were recorded in electron counting mode at  $\times 81,000$  nominal magnification (1.1  $\text{\AA}/\text{pixel}$  at the specimen level) consisting of 33 frames over 3 sec (total electron exposure of of 53  $e^{-}/\text{\AA}^2$  corresponding to 1.6  $e^{-}/\text{\AA}^2/\text{frame}$ ) using the Thermo Fisher Scientific EPU data collection software. The defocus range was set between -0.3 – 3  $\mu\text{m}$ . For the t2 dataset, 30053 micrographs at  $\times 130,000$  nominal magnification (1.09  $\text{\AA}/\text{pixel}$  at the specimen level) consisting of 20 or 25 frames, respectively, were recorded with a Gatan K2 Summit direct electron detector operated in electron-counting mode and Gatan energy filter with slit of 10 eV (re-centered slit every 6 hours). The accumulated electron exposure was 30.7  $e^{-}/\text{\AA}^2$  (corresponding to 1.24 or 1.55  $e^{-}/\text{\AA}^2/\text{frame}$ ) during a 5 s exposure at - 0.3 – 4  $\mu\text{m}$  defocus range (Table 1).

## Cryo-EM image processing and atomic model building

Single particle analyses (SPA) were performed using Relion (v3.0b and v3.1)<sup>4,5</sup>. Micrograph frames (movies) were motion-corrected using MOTIONCOR2 (implemented in Relion)<sup>6</sup>, dose-weighted (using 1.24 or 1.55  $e^{-}/\text{\AA}^2/\text{frame}$  for t2 and 1.55  $e^{-}/\text{\AA}^2/\text{frame}$  for t1) and

the contrast transfer function (CTF) parameters were estimated with CTFFIND4 (v4.1.14)<sup>7</sup>. Particles were automatically picked from the motion-corrected micrographs either using CrYOLO (v1.4)<sup>8</sup>, Gautomatch (v0.56)<sup>9</sup> and Relion Autopick trained with a subset of manually picked particles. In the t1 dataset, approximately 4 million coordinates were picked. Particle images were extracted with a box size of 80 px (bin=4) and subjected to multiple rounds of 2D classifications. Only particles present in homogeneous classes were kept, amounting to 948,812 particles (after duplicate removal). Focussed classifications were performed by re-extracting particles with a box size of 360 px, centered around the RuvB rings (1,881,624 particles) and the central RuvA-HJ (948,812 particles) part. Subsequently, three rounds of refinement, per-particle CTF and Bayesian polishing were performed. Additionally, for the RuvA-HJ reconstruction, signals emerging for the RuvB rings were subtracted. For the t2 dataset, approximately 9 million coordinates were used to extract particles, which were subsequently subjected to 4-times binning and multiple rounds of 2D classifications, leading to a total of 1,786,669 particles. From these, three groups of particles were identified and three particle subsets were generated: 1) Tripartite RuvAB-HJ particles (717,780) containing two RuvB motors, 2) bipartite RuvAB-HJ particles containing one RuvB motor (549,364 particles) and 3) RuvB-HJ complexes lacking RuvA (519,525 particles). For the reconstruction of the tripartite RuvAB-HJ complex only particles from group 1 were used. At first, an *ab initio* model was created in Relion using a smaller subset of particles (n = 50,000). Subsequent classifications and refinements lead to a consensus reconstruction yielding a resolution of ~8 Å. Particles from group 2 were used to reconstruct the bipartite RuvAB-HJ structure and were merged with the group 1 particles after subtraction of the signal corresponding to one RuvB motor to generate pseudo bipartite particles. The combined particle stack (bipartite + pseudo bipartite particles) resulted in a reconstruction of the bipartite RuvAB-HJ complex yielding a resolution of ~5 Å. Focussed reconstruction procedures were performed as described for the t1 dataset, and which resulted in 3D reconstructions of the RuvB motor and the central RuvA-HJ subcomplexes, respectively. The RuvA-HJ subcomplex was reconstructed using particles from the combined particle stack (group 1+2). For the RuvB structures, a total of approximately 2.3 million RuvB motors were extracted (from all three groups), centered, 3D classified, and subsets were independently refined. Subsequently, per-particle CTF, Bayesian polishing, and 3D refinements were performed twice. Applying this procedure resulted in 9 distinctive RuvB motor structures,

ranging from 2.9 to 4.1 Å in resolution. Local resolution estimates, gold-standard resolution (Fourier shell correlation (FSC) = 0.143) and sharpened maps (B-factor range: 30-80/focused refinements) were calculated using Relion 3.1.

Model building started by generating homology models for RuvA and RuvB with SWISS-MODEL<sup>10</sup>. For RuvA, Protein Data Bank (PDB) entry 1BVS served as a structural template, and PDB entry 1HQC<sup>11</sup> served as a reference model for RuvB. Models were fitted into EM maps using the *fit-in-map* tool in UCSF Chimera (v1.13)<sup>12</sup>. Initial model refinements were performed with Rosetta (v3.12)<sup>13</sup> controlled via StarMap v.1.1.12 (manuscript in preparation). Further interactive refinement was carried out in ISOLDE (v1.1.2)<sup>14</sup>, a molecular dynamics-guided structure refinement tool within UCSF ChimeraX (v1.2.5)<sup>15</sup>. Finally, the resulting coordinate files were refined with Phenix.real\_space\_refine (v1.19.1-4122)<sup>16</sup> using reference model restraints, strict rotamer matching and disabled grid search settings. MolProbity server<sup>17</sup>, EMringer<sup>18</sup> (via phenix) and Z-Score were used to validate model geometries and *model-to-map* fits.

### **Visualization, analysis and deposition**

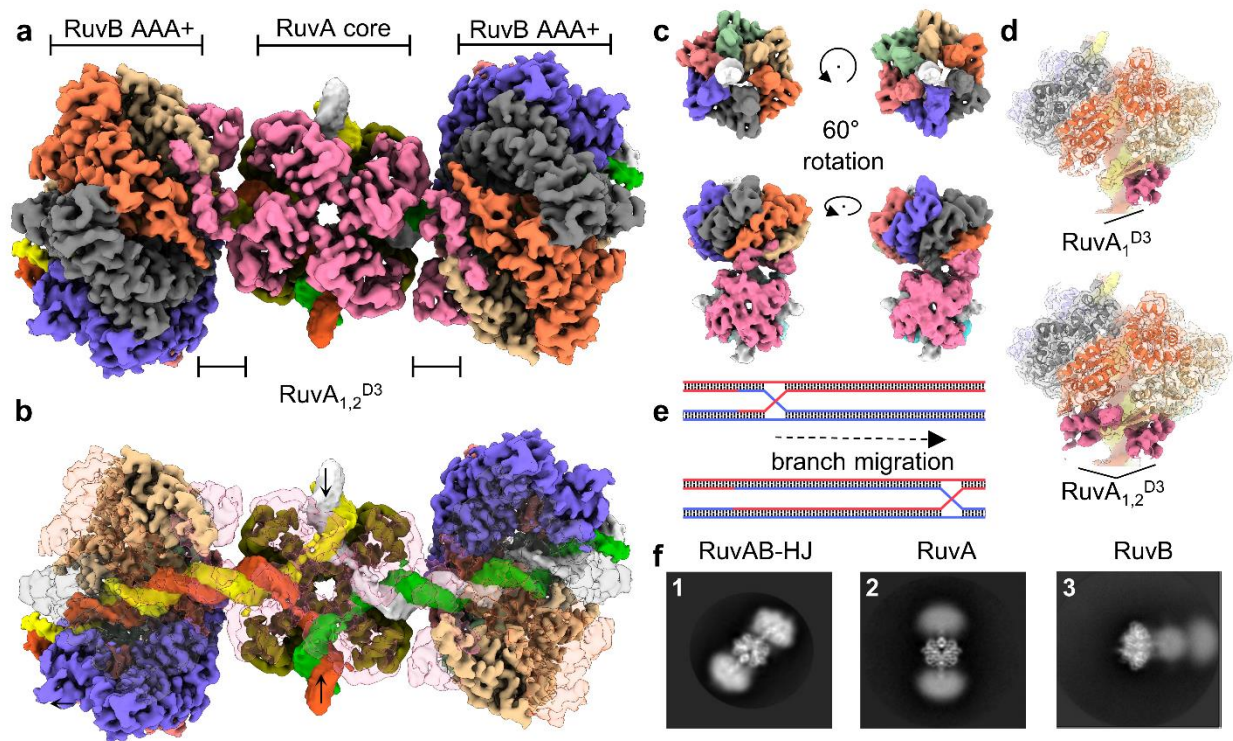
UCSF Chimera (1.13)<sup>12</sup>, ChimeraX (v1.2.5)<sup>15</sup> and PyMOL (2.4.1) were used for visualizations. The EM maps and corresponding atomic model have been deposited at the Electron Microscopy Data Bank and Protein Data Bank under accession numbers EMD-13294, EMD-13295, EMD-13296, EMD-13297, EMD-13298, EMD-13299, EMD-13300, EMD-13301, EMD-13302, EMD-13303, EMD-13304, EMD-13305, EMD-13306 and PDB: 7PBL, 7PBM, 7PBN, 7PBO, 7PBP, 7PBQ, 7PBR, 7PBS, 7PBT, 7PBU, 7PBV.

## References

1. Shah, R., Bennett, R. J. & West, S. C. Activation of RuvC holliday junction resolvase in vitro. *Nucleic Acids Research* **22**, 2490–2497 (1994).
2. Mayanagi, K., Fujiwara, Y., Miyata, T. & Morikawa, K. Electron microscopic single particle analysis of a tetrameric RuvA/RuvB/Holliday junction DNA complex. *Biochemical and Biophysical Research Communications* **365**, 273–278 (2008).
3. Constantinou, A. & West, S. C. Holliday junction branch migration and resolution assays. *Methods in molecular biology (Clifton, N.J.)* **262**, 239–253 (2004).
4. Zivanov, J. *et al.* New tools for automated high-resolution cryo-EM structure determination in RELION-3. *eLife* **7**, (2018).
5. Zivanov, J., Nakane, T. & Scheres, S. H. W. Estimation of high-order aberrations and anisotropic magnification from cryo-EM data sets in RELION-3.1. *IUCrJ* **7**, 253 (2020).
6. Zheng, S. Q. *et al.* MotionCor2: anisotropic correction of beam-induced motion for improved cryo-electron microscopy. *Nature Methods* **14**, 331–332 (2017).
7. Rohou, A. & Grigorieff, N. CTFIND4: Fast and accurate defocus estimation from electron micrographs. *Journal of Structural Biology* **192**, 216–221 (2015).
8. Wagner, T. & Raunser, S. The evolution of SPHIRE-cRYOLO particle picking and its application in automated cryo-EM processing workflows. *Communications Biology* **2020 3:1** **3**, 1–5 (2020).
9. Zhang, K., L. M. & S. F. Gautomatch: an efficient and convenient gpu-based automatic particle selection program. (2011).
10. Bordoli, L. *et al.* Protein structure homology modeling using SWISS-MODEL workspace. *Nature Protocols* **2009 4:1** **4**, 1–13 (2008).
11. Yamada, K. *et al.* Crystal structure of the Holliday junction migration motor protein RuvB from *Thermus thermophilus* HB8. *Proceedings of the National Academy of Sciences* **98**, 1442–1447 (2001).
12. Pettersen, E. F. *et al.* UCSF Chimera—A visualization system for exploratory research and analysis. *Journal of Computational Chemistry* **25**, 1605–1612 (2004).
13. DiMaio, F., Leaver-Fay, A., Bradley, P., Baker, D. & André, I. Modeling Symmetric Macromolecular Structures in Rosetta3. *PLOS ONE* **6**, e20450 (2011).
14. Croll, T. I. ISOLDE: a physically realistic environment for model building into low-resolution electron-density maps. *Acta Crystallographica. Section D, Structural Biology* **74**, 519 (2018).

15. Pettersen, E. F. *et al.* UCSF ChimeraX: Structure visualization for researchers, educators, and developers. *Protein Science* **30**, 70–82 (2021).
16. Liebschner, D. *et al.* Macromolecular structure determination using X-rays, neutrons and electrons: recent developments in Phenix. *Acta Crystallographica. Section D, Structural Biology* **75**, 861 (2019).
17. Williams, C. J. *et al.* MolProbity: More and better reference data for improved all-atom structure validation. *Protein Science* **27**, 293–315 (2018).
18. Barad, B. A. *et al.* EMRinger: side chain–directed model and map validation for 3D cryo-electron microscopy. *Nature Methods* 2015 12:10 **12**, 943–946 (2015).

**Figure 1. Cryo-EM structure of the RuvAB-HJ branch migration complex.**



a, Cryo-EM composite map of the fully-assembled RuvAB complex bound to a four-way Holliday junction. The dimensions of the dumbbell-like shaped complex are 23 x 12 nm. The stoichiometry is 8:12 for RuvA:RuvB. The two RuvA tetramers are individually colored (pink/olive). Each protomer in the RuvB homohexamer has been assigned a different color.

b, Composite map of the fully-assembled RuvAB-HJ complex in which substrate-disengaged RuvB protomers and one RuvA tetramer are transparent to visualize the HJ crossover and the interaction of each RuvB motor with its cognate DNA substrate.

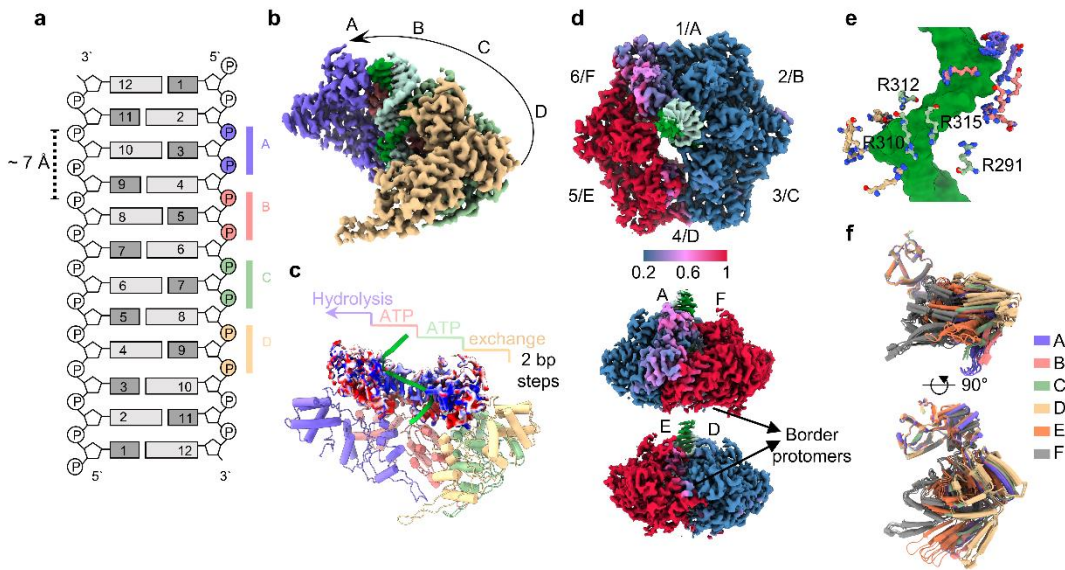
c, 3D-classes of the bipartite particles (front and side views), highlighting the 60° rotation of the RuvB motor and the interacting RuvA<sup>D3</sup> domains with respect to the RuvA-HJ core.

d, RuvB motors bind to one or two RuvA<sup>D3</sup> domains. The two RuvA<sup>D3</sup> domains bind to adjacent RuvB protomers in the RuvB motor.

e, Schematic diagram of the Holliday junction branch migration.

f, Representative 2D-classes illustrating the enormous flexibility between each of the three complexes in the tripartite particle. (1) Focused on the entire tripartite RuvAB-HJ particle, (2) focused on the RuvA-HJ core, (3) focused on one RuvB AAA+ motor.

**Figure 2. Architecture and conformational variability of the RuvB AAA+ motor.**



(RuvB<sub>1-4</sub>) and the DNA substrate. RuvB protomers engage the DNA substrate every two base pairs. The distance between 3 consecutive bases in the double-stranded DNA substrate is  $\sim 7 \text{ \AA}$ .

b, Cryo-EM map highlighting the formation of a spiral staircase by the DNA-interacting protomers RuvB<sub>1-4</sub> in clusters A-D.

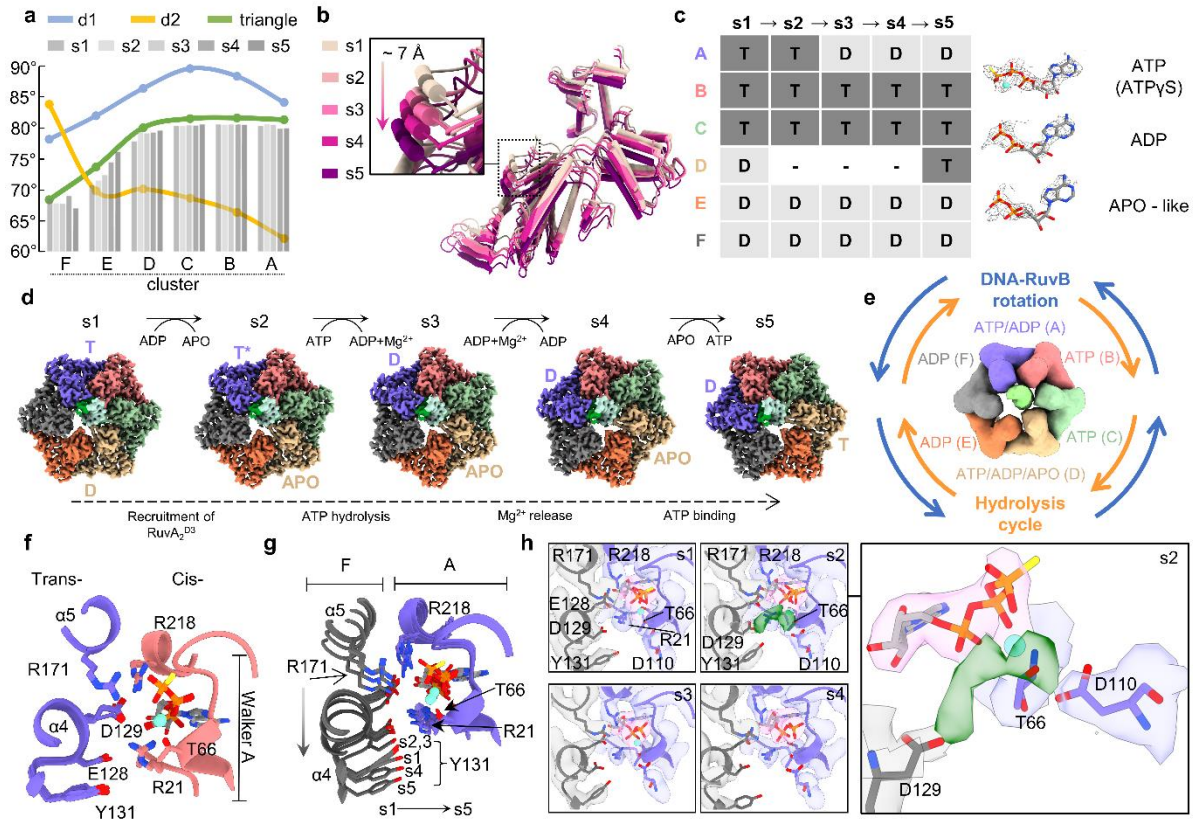
c, Surface charge representation of the pit-like composite DNA-binding interface that is formed by the winged-helix motif in the head domains of staircase RuvB<sub>1-4</sub>. The spiral staircase formed by RuvB<sub>1-4</sub> is indicated. The nucleotide configuration, ATP hydrolysis position and nucleotide exchange position are highlighted in respect to the staircase.

d, Cryo-EM map of a RuvB motor colored according to the distance (in  $\text{\AA}$ ) of  $C_{\alpha}$  atoms between similarly-positioned RuvB protomers (variance) across the states s1<sub>12</sub> to s5<sub>12</sub>. Atomic models were aligned to the DNA substrate. The variance analysis divides the RuvB hexamer into a rigid (blue; variance  $< 0.2 \text{ \AA}$ ) and a flexible (red; variance  $> 1 \text{ \AA}$ ) area, connected by the border protomers RuvB<sub>1</sub> (cluster A) and RuvB<sub>4</sub> (cluster D).

e, Spiral staircase organization of the conserved arginine residues located in the head domains of RuvB<sub>1-4</sub>.

f, Superposition of RuvB protomers extracted from the five RuvB motor states  $s1_{t2}$  to  $s5_{t2}$ . RuvB protomers were aligned to the head domain of RuvB. Colors and labels represent conformational clusters.

**Figure 3. Dynamics and nucleotide pocket analysis of the RuvB AAA+ motor conformations.**



a, Geometrical analysis of the RuvB protomers. Average dihedral angles (d1, d2) of RuvB protomers from states  $s_{12}$  to  $s_{52}$  were measured between RuvB<sup>S</sup> and RuvB<sup>L</sup> domains (blue line) and RuvB<sup>H</sup> and RuvB<sup>S</sup> domains (yellow line). The corresponding average triangle angle was measured using the three mass centers of RuvB<sup>L</sup>, RuvB<sup>S</sup> and RuvB<sup>H</sup> (green line). Columns represent the triangle angle of individual RuvB protomers across the states  $s_{12}$  to  $s_{52}$ .

b, Unidirectional trajectory of RuvB<sub>5</sub> in conformational cluster E, covering an average distance of  $\sim 7$  Å. To visualize the trajectory, RuvB hexamers were superimposed on the rigid RuvB<sub>2+3</sub> protomers in the clusters B and C.

c, Table highlighting the nucleotide in each RuvB protomer across the states  $s_{12}$  to  $s_{52}$ . The states are ordered from  $s_1$ - $s_2$ - $s_3$ - $s_4$ - $s_5$ , according to the trajectory observed for RuvB<sub>5</sub> in cluster E. The same order is consistent with the progression of the ATP hydrolysis reaction (cluster A) and the

chronology of the nucleotide exchange event (cluster E). T = ATP $\gamma$ S, D = ADP, dash = APO-like. Cryo-EM densities are shown as representative examples for each nucleotide, including an ADP modeled into an APO-like density.

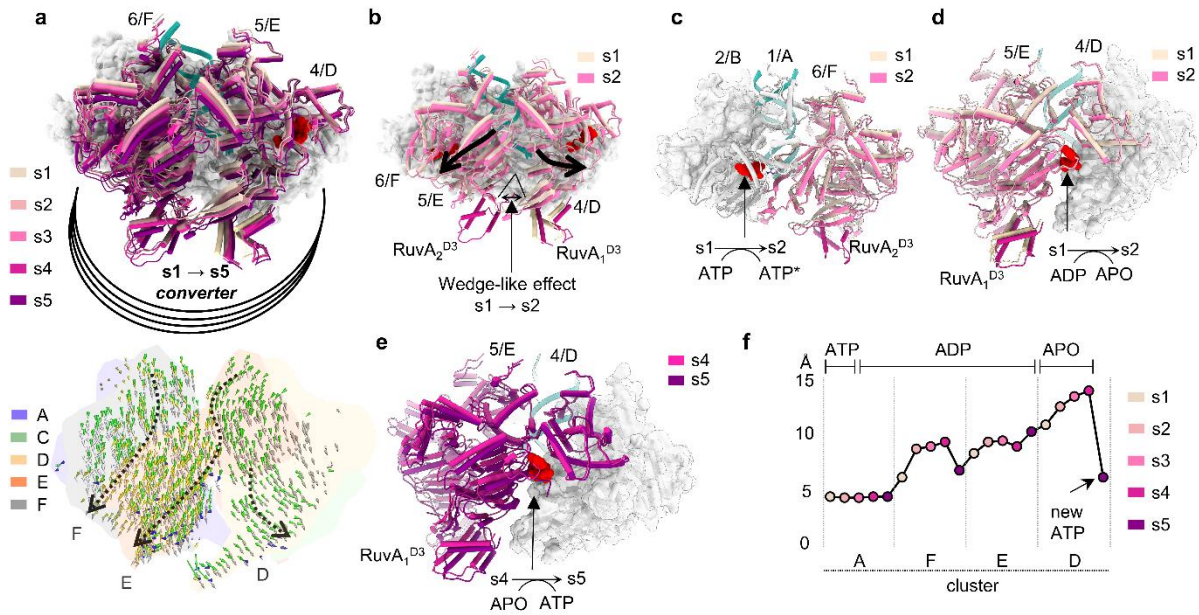
d, ATP hydrolysis reaction and nucleotide exchange shown as they occur during the progression from state s1<sub>t2</sub> to state s5<sub>t2</sub> in the RuvB *motor*. Colors represent conformational clusters. The 60° rotation (from s1<sub>t2</sub> to s5<sub>t2</sub>) of the RuvB hexamer emphasizes the counterclockwise motion of the RuvB motor observed during branch migration. T = ATP $\gamma$ S, D = ADP. Asterisks indicate ordered water molecules in the RuvB<sub>1</sub> NBP of cluster A.

e, Schematic highlighting the opposing directionalities of the RuvB motor rotation (blue arrows) and the ATP hydrolysis cycle (orange arrows).

f, Superposition of the five interfaces that form between the non-hydrolysing RuvB<sub>2</sub> NBP (cluster B) and RuvB<sub>1</sub> (cluster A) from the ATP hydrolysis cycle states s1<sub>t2</sub> to s5<sub>t2</sub>.

g-h, Superposition of the five interfaces that form between the ATP-hydrolysing RuvB<sub>1</sub> NBP (cluster A) and RuvB<sub>6</sub> (cluster F) from the ATP hydrolysis cycle states s1<sub>t2</sub> to s5<sub>t2</sub>. A gradual displacement of the RuvB<sub>6</sub> alpha helices  $\alpha$ 4 and  $\alpha$ 5 results in a reorganization of the electrostatic network in the RuvB<sub>1</sub> NBP, leading to ATP hydrolysis. Magnification highlights unmodeled cryo-EM density (green density) in state s2<sub>t2</sub>, which likely corresponds to ordered water molecules initiating the nucleophilic attack on the ATP  $\gamma$ -phosphate in course of the ATP hydrolysis reaction. *Cis*-Asp110 and *trans*-Asp129 have both been shown to be critical for ATP hydrolysis in RuvB.

**Figure 4. RuvA operates the ATP hydrolysis cycle in the RuvB motor through binding to the converter module.**



a, Cartoon representation of the RuvB protomers RuvB<sub>6</sub> (cluster F), RuvB<sub>5</sub> (cluster E) and RuvB domain RuvB<sub>4</sub><sup>L</sup> (cluster D), which, together, build the *converter* module in the RuvB motor. The remaining RuvB protomers and domains are shown in surface representation. RuvA<sub>1</sub><sup>D3</sup> and RuvA<sub>2</sub><sup>D3</sup> domains are shown in cartoon representation. Colors correspond to the five ATP hydrolysis cycle states (s<sub>1t2</sub>-s<sub>5t2</sub>). Lines emphasize the downwards-directed motion of the *converter* module with respect to the DNA substrate.

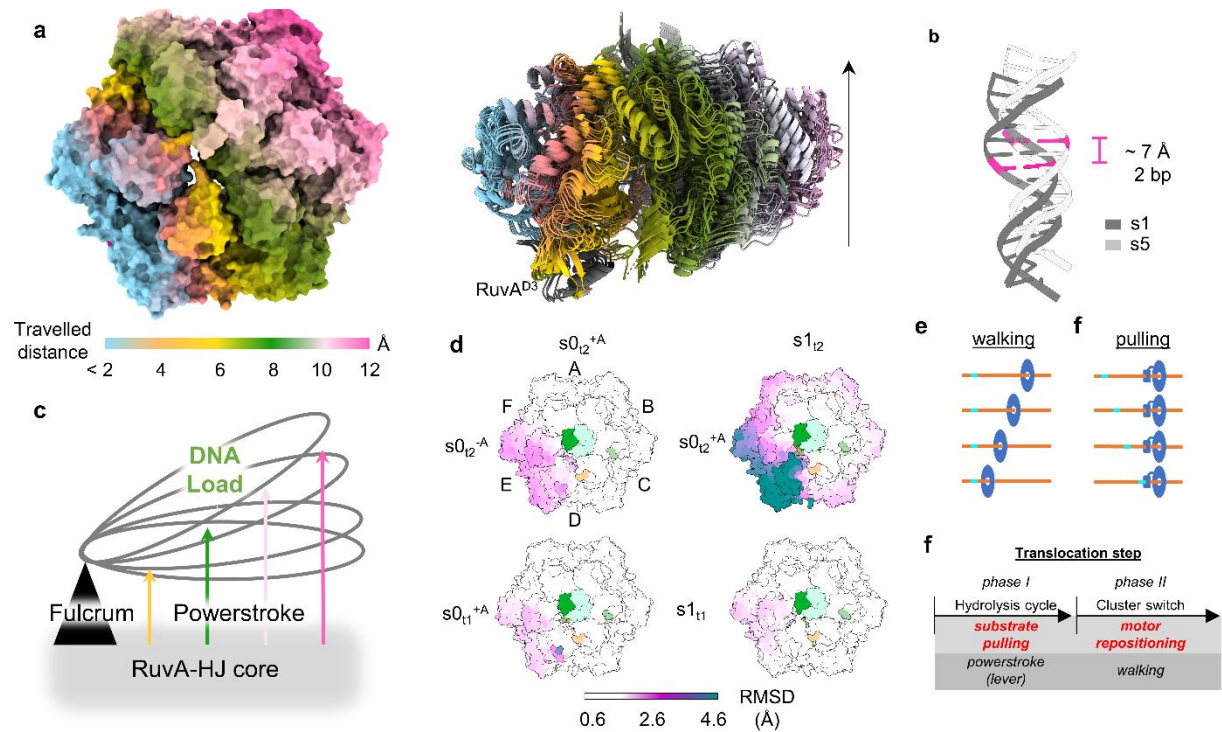
b, RuvA<sub>2</sub><sup>D3</sup>-induced wedge-like effect on the *converter* module in the RuvB motor. Colors correspond to ATP hydrolysis cycle states (s<sub>1t2</sub>-s<sub>2t2</sub>). Arrows indicate the displacement of the domain cores of RuvB<sub>4</sub><sup>L</sup> and RuvB<sub>5</sub><sup>L</sup>.

c-d, Long-range interprotomer signaling triggered by RuvA<sub>2</sub><sup>D3</sup> binding, leading to the formation of ordered water between the ATP in the RuvB<sub>1</sub> NBP (cluster A) and RuvB<sub>6</sub> (cluster F) prior to ATP hydrolysis in the transition from ATP hydrolysis cycle state s<sub>1t2</sub> to s<sub>2t2</sub> (c), and simultaneous opening of the RuvB<sub>4</sub> NBP, leading to the release of the ADP molecule (d). Colors correspond to the ATP hydrolysis cycle states (s<sub>1t2</sub>-s<sub>2t2</sub>).

e, Conformational changes in the *converter module* associated with the completion of nucleotide exchange in the transition from ATP hydrolysis cycle state  $s_{4t2}$  to  $s_{5t2}$ . Colors correspond to the states  $s_{4t2}$  and  $s_{5t2}$ .

f, Distance ( $\text{\AA}$ ) between the *cis*-acting Arg21 and *trans*-acting Glu110 as a measure for the gate-opening and gate-closing motions of the RuvB N terminus during the ATP hydrolysis cycle of the RuvB motor. Gate-opening of a RuvB protomer starts in cluster F, continues in cluster E and reaches its maximum opening in cluster D, which results in the release of ADP.

**Figure 5. RuvB motors facilitate substrate translocation by a lever mechanism.**



a-b, Superposition of RuvB motor states on RuvB<sub>5</sub>, illustrating the change of height is proportional to the distance to RuvB<sub>5</sub>. The travelled height distance (Å) is represented by color (a). Ribbon diagram of the DNA substrate before (s1<sub>12</sub>) and after the lever action (s5<sub>12</sub>). Scale bar indicates the traveled height of 7 Å corresponds to one translocation step of two base pairs.

c, Schematic of the RuvB motor lever mechanism. Binding of RuvA<sup>D3</sup> to substrate-disengaged RuvB<sub>5</sub> generates a fulcrum, which enables RuvB motors to convert the energy contained in ATP into a lever action. The resulting lift of the DNA binding interface causes the translocation of the substrate. Hence, The RuvAB-HJ machinery uses the basis principle of a lever machine to gain mechanical advantage. According to this principle, the input energy needed for the lift remains constant (energy conservation law), however, the required force decreases proportionally with the distance between the load (DNA) and the fulcrum (RuvA).

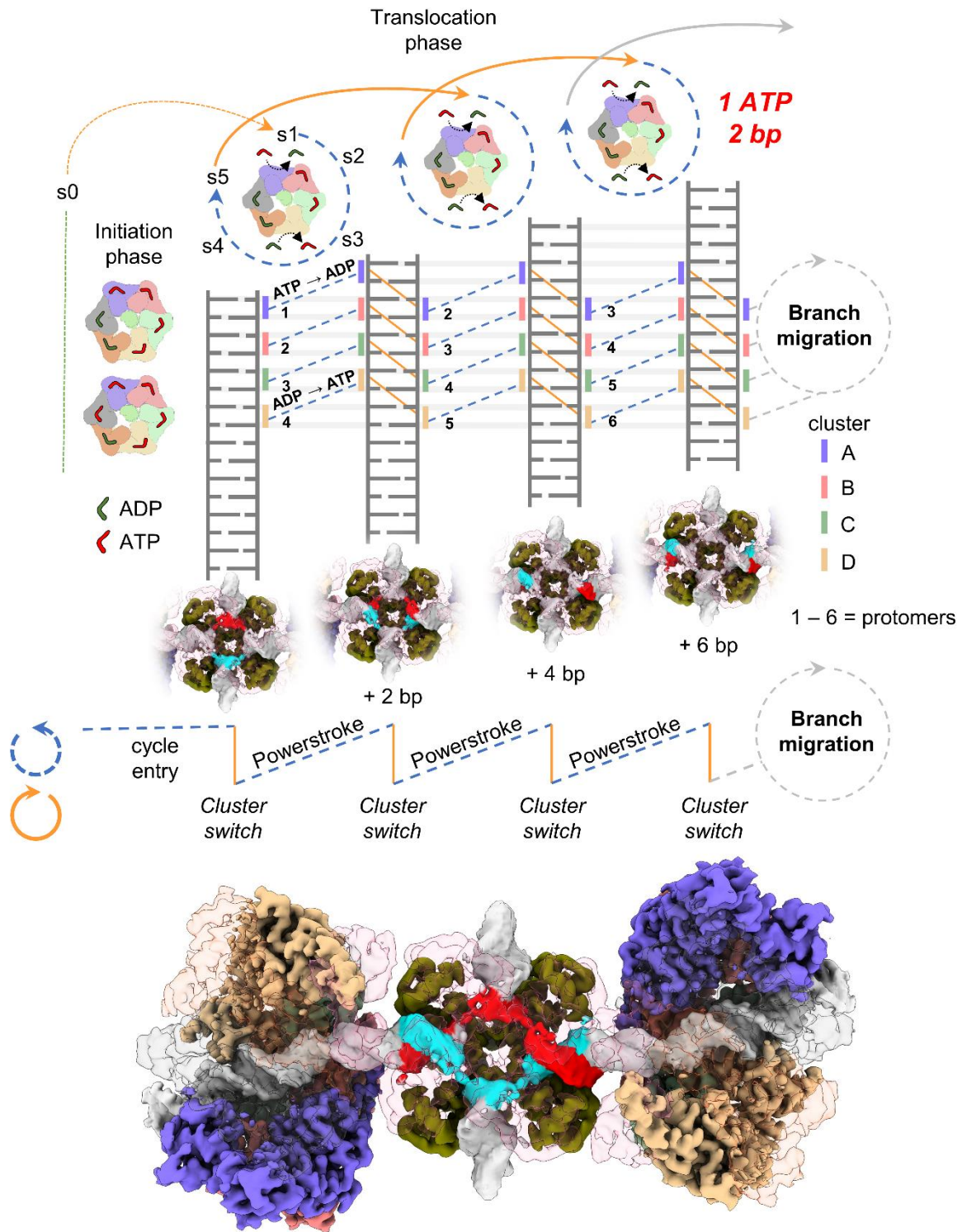
d, Structural similarity of the *converter* module measured by the RMSD<sub>Cα</sub> (in Å) between the initiation states (s0<sub>11</sub><sup>+A</sup>, s0<sub>12</sub><sup>+A</sup>), ATP hydrolysis cycle states (s1<sub>11</sub>, s1<sub>12</sub>) and the RuvA<sup>D3</sup>-free state

$s0_{t2}^{-A}$ , obtained from the two datasets t1 and t2. States were aligned to the DNA. The t2 dataset states  $s0_{t2}^{+A}$  and  $s1_{t2}$  served as a reference. Colors indicate the  $RMSD_{C\alpha}$  (in Å).

e, Illustration of the difference between walking of the AAA+ motor on the substrate and AAA+ motor pulling the substrate.

f, Separation of one translocation step during branch migration into two phases.

**Figure 6. Model for HJ branch migration through continuous DNA translocation mediated by RuvAB.**



Initiation states containing either five ( $s_{0t_1}^{+A}$ ) or four ( $s_{0t_2}^{+A}$ ) ATP molecules provide a potential entry pathway ( $s_0$  to  $s_1$ ) into the ATP hydrolysis cycle, which starts with state  $s_1$  (for simplification, initiation states are summarized under the label  $s_0$ ). The ATP hydrolysis cycle is represented by the five states  $s_{1t_2}$  to  $s_{5t_2}$ . During this cycle, the energy contained in ATP is converted into a lever action or powerstroke, causing DNA translocation of two base pairs per hydrolysed ATP molecule (blue dashed lines). This is also indicated by the translocating base pairs (cyan/red colors) of the HJ crossover. *Cluster switches*, in which RuvB protomers undergo register shifts, cause the hand over of the DNA substrate in the central pore. This enables RuvB motors to generate iterative powerstrokes, and, thus, provides the mechanistic basis for continuous branch migration.

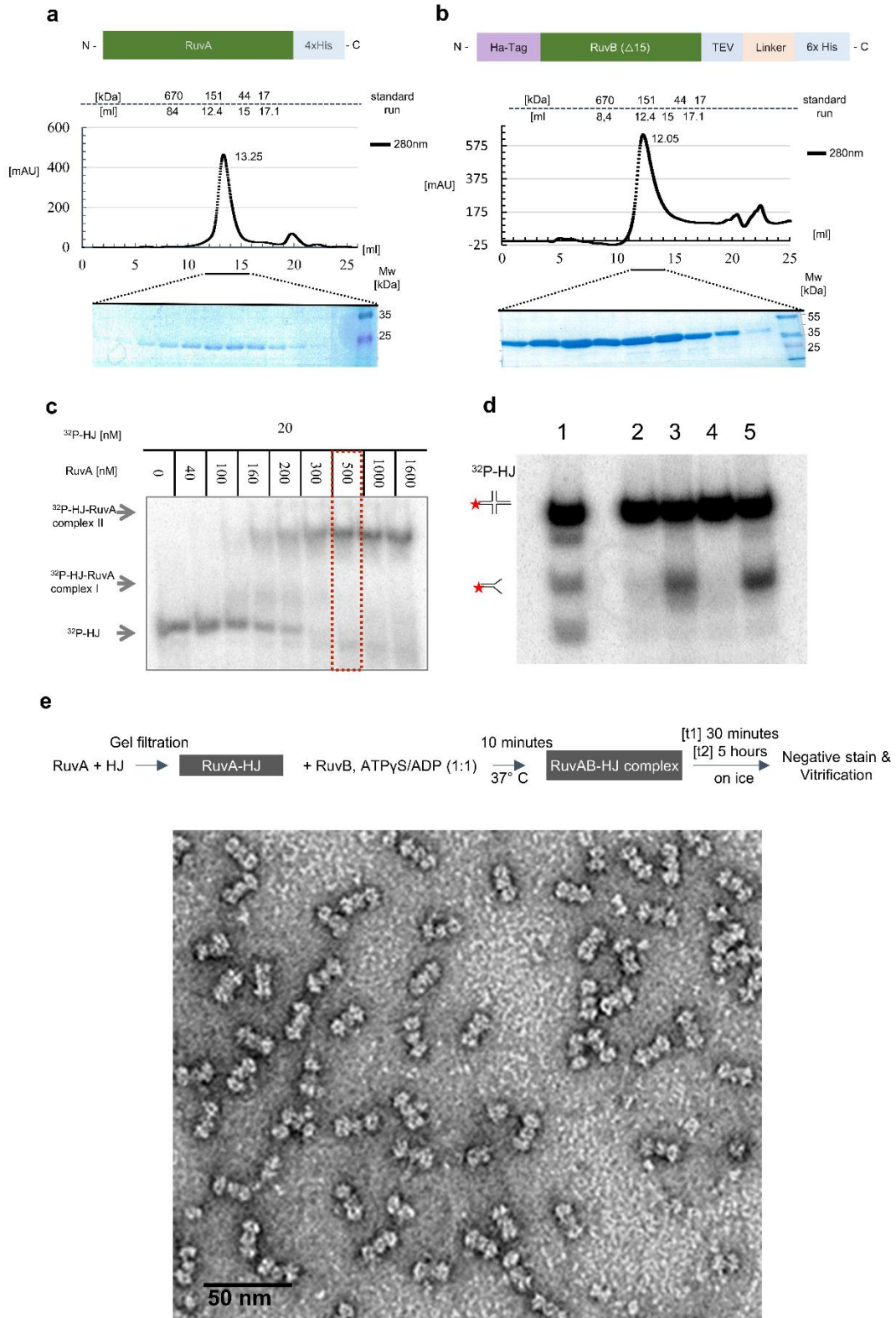
# **Supplementary Information for Chapter 1**

## **Architecture and operating principles of the RuvAB Holliday junction branch migration complex**

*Manuscript submitted for review, August 2021*

Jiri Wald, Dirk Fahrenkamp, Nikolaus Gössweiner-Mohr, Wolfgang Lugmayr, Luciano Ciccarelli, Oliver Vesper, and Thomas C. Marlovits

# Extended Data Figure 1



**Extended Data Fig 1. Protein purification and *in vitro* reconstitution of the RuvAB-HJ complex.**

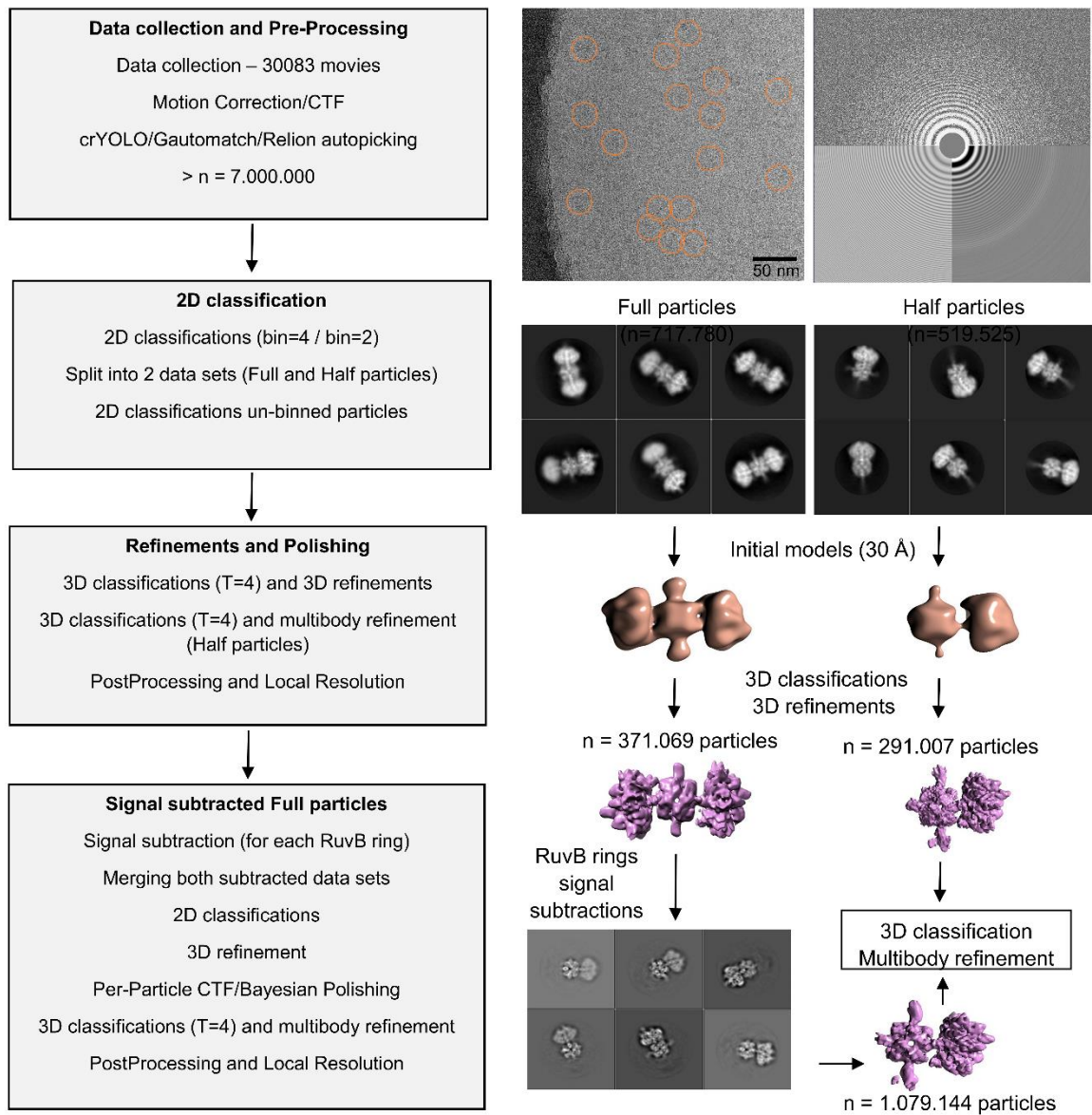
a-b, Domain organization and purification of the RuvA (a) and RuvB (b) constructs used in this study. Shown is the final gel filtration and the corresponding protein staining. The retention time of RuvA (13.25 ml) corresponds to the predicted size of a RuvA tetramer (4 x 24 kDa), while the corresponding retention time of RuvB (12.05 ml) corresponds to a mixture of oligomeric stains, likely containing dimers (2 x 37 kDa), trimers (3 x 37 kDa) and tetramers (4 x 37 kDa). Molecular weights were approximated by comparing the retention times with those of a gel filtration standard.

c, Electrophoretic mobility shift assay (EMSA) using constant amounts of <sup>32</sup>P-labeled HJ (Y2AP) and increasing amounts of recombinant RuvA to confirm its HJ binding capacity (for details, see *Materials and methods*).

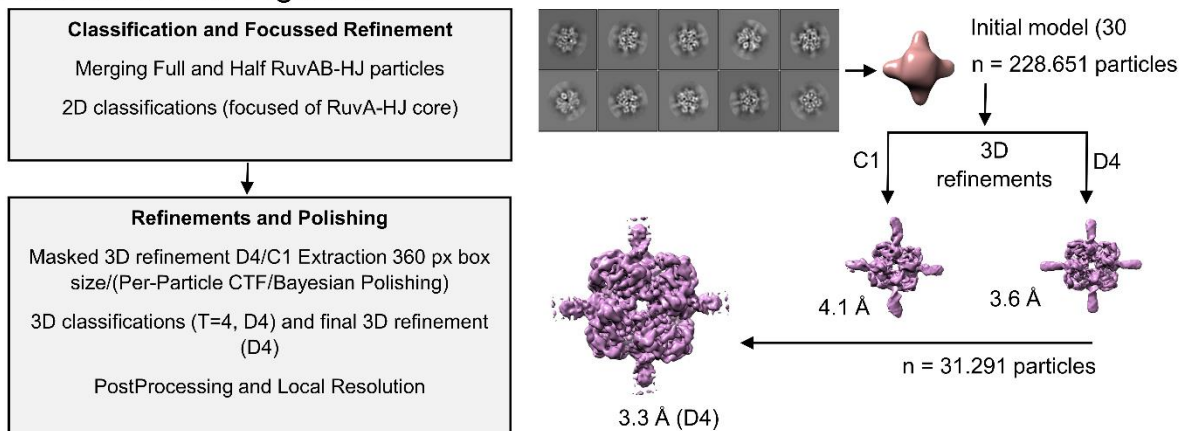
d, Comparison of the HJ branch migration activities using recombinant *Salmonella typhimurium* RuvA and either recombinant *Salmonella typhimurium* RuvB (lanes 2-3) or recombinant *Streptococcus Thermophilus* RuvB (lanes 4-5). Branch migration of both complexes was assessed with (lanes 3, 5) or without (lanes 2, 4) the addition of ATP. No recombinant proteins were added in the reference sample (lane 1). Branch migration assay was performed with <sup>32</sup>P-labeled (red star) HJ (X26) at 37°C. The HJ contains a 26-base pair homologous core with heterologous sequences in the shoulders to impair spontaneous branch migration.

e, Schematic of the *in vitro* reconstitution strategy applied in this study, together with a representative micrograph of the negatively-stained RuvAB-HJ branch migration complex.

## Extended Data Figure 2



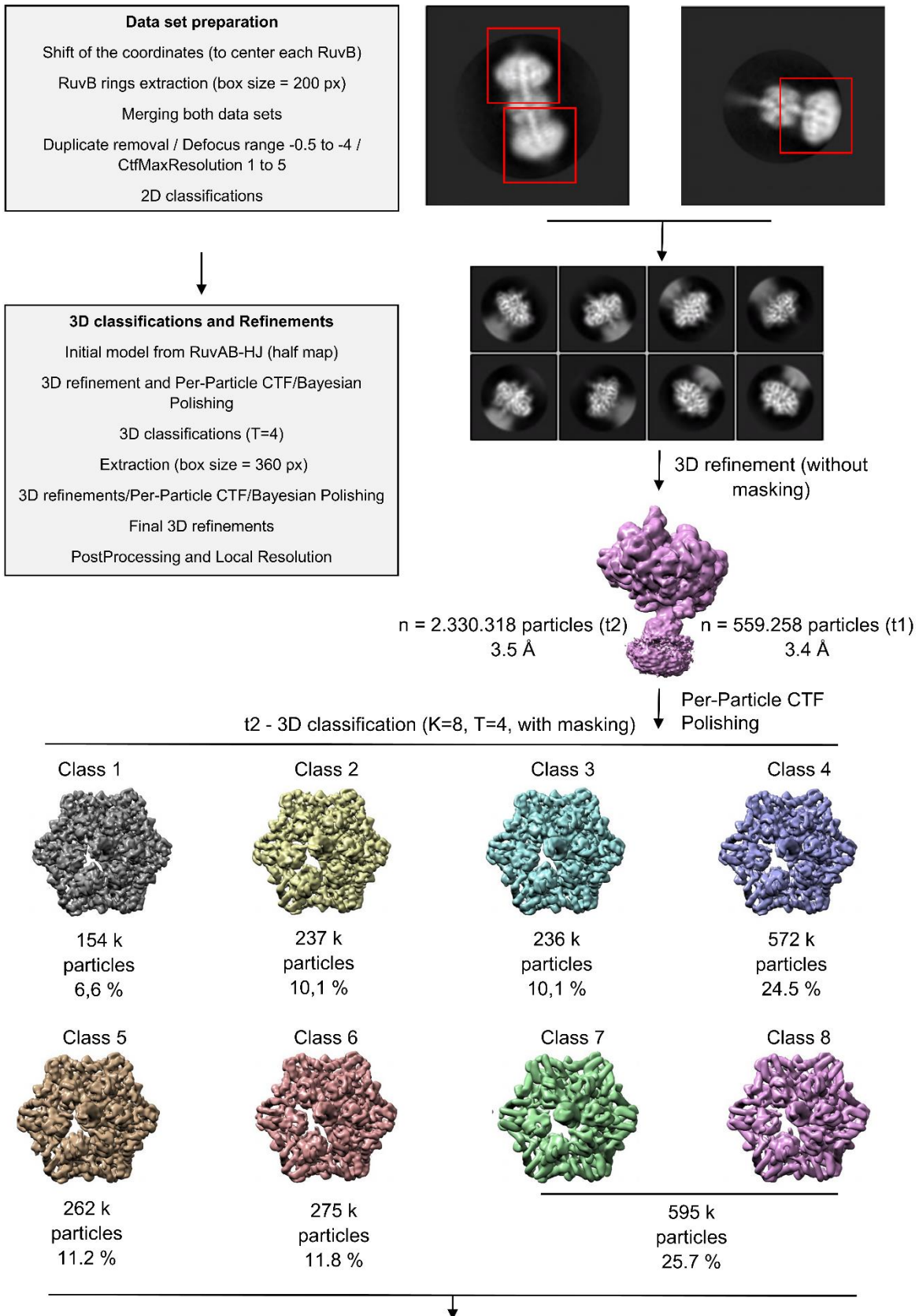
## Extended Data Figure 3

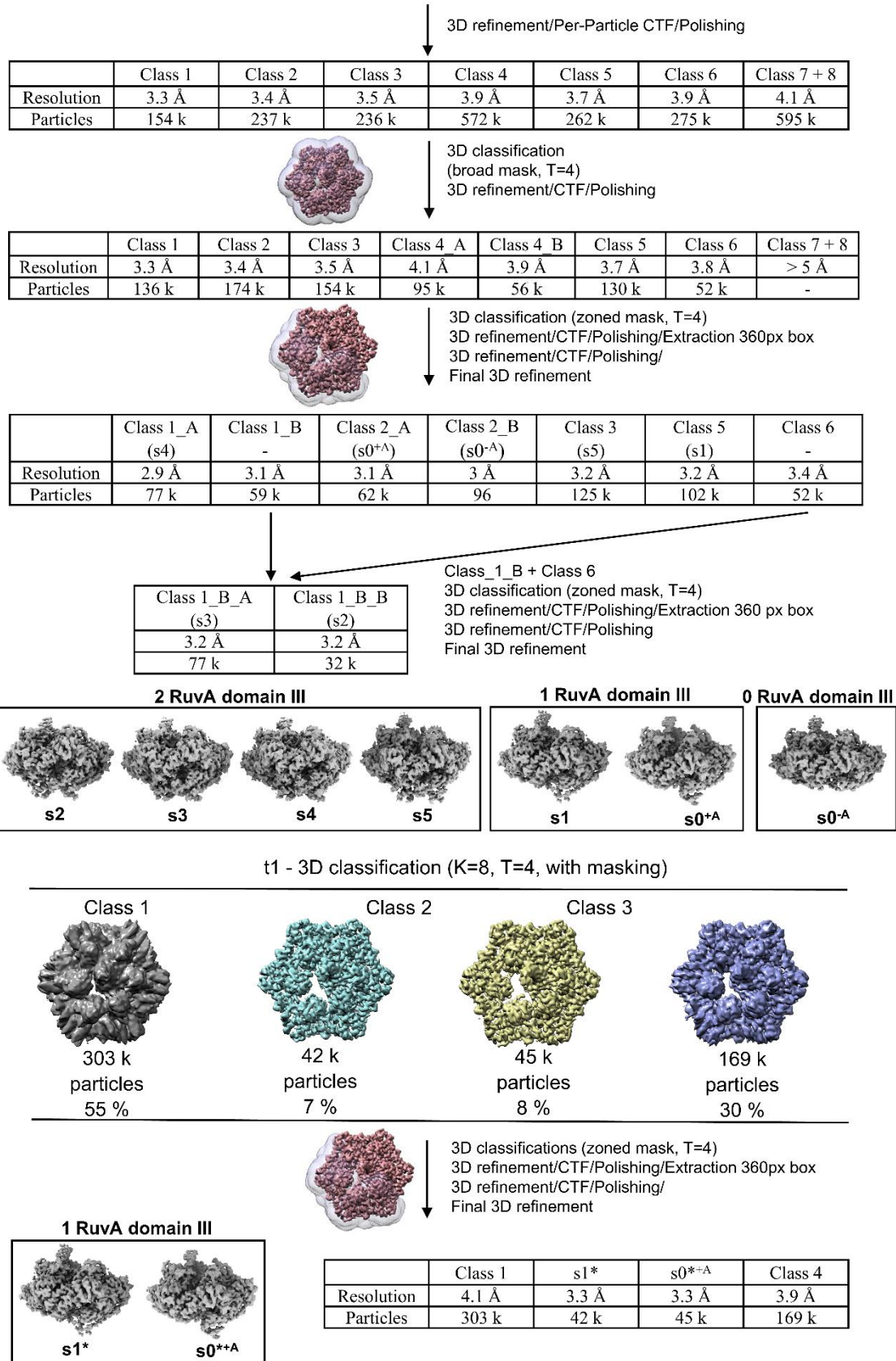


**Extended Data Fig 2. Cryo-EM data collection and single particle reconstruction procedure of the tripartite and bipartite RuvAB-HJ complexes.**

**Extended Data Fig 3. Cryo-EM data collection and single particle reconstruction procedure of RuvA-HJ core complexes.**

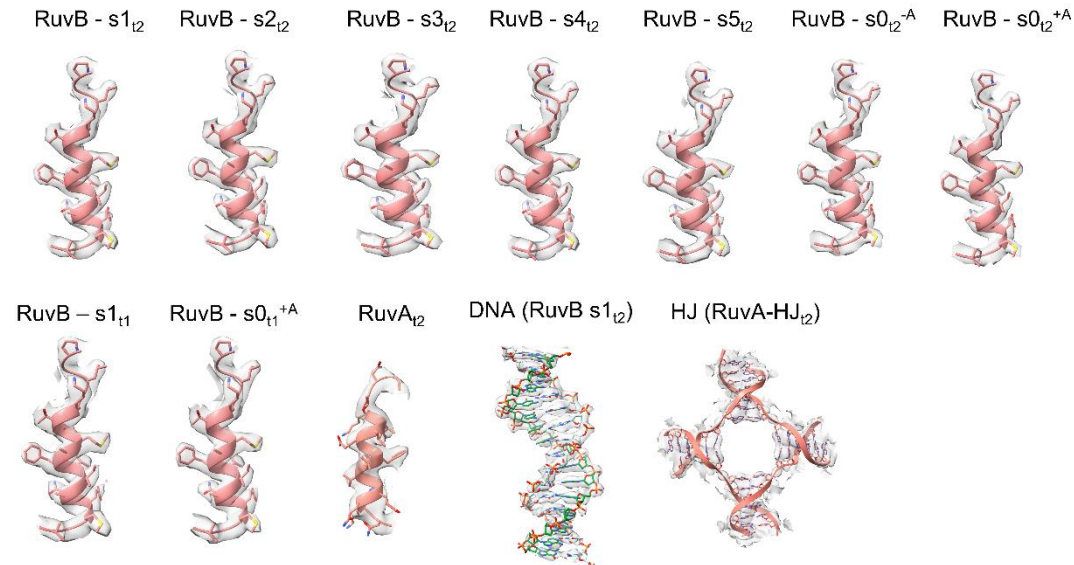
## Extended Data Figure 4



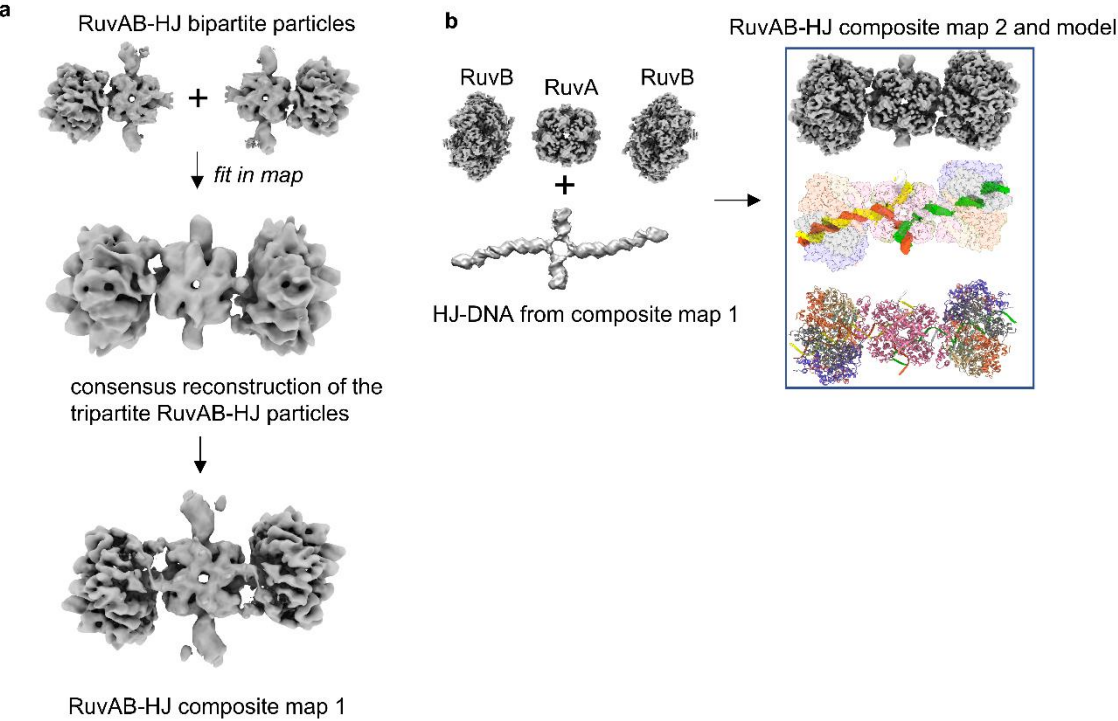


**Extended Data Fig 4. Cryo-EM data collection and single particle reconstruction procedure of RuvB-HJ complexes.**

### Extended Data Figure 5



### Extended Data Figure 6



**Extended Data Fig 5. Example cryo-EM density.**

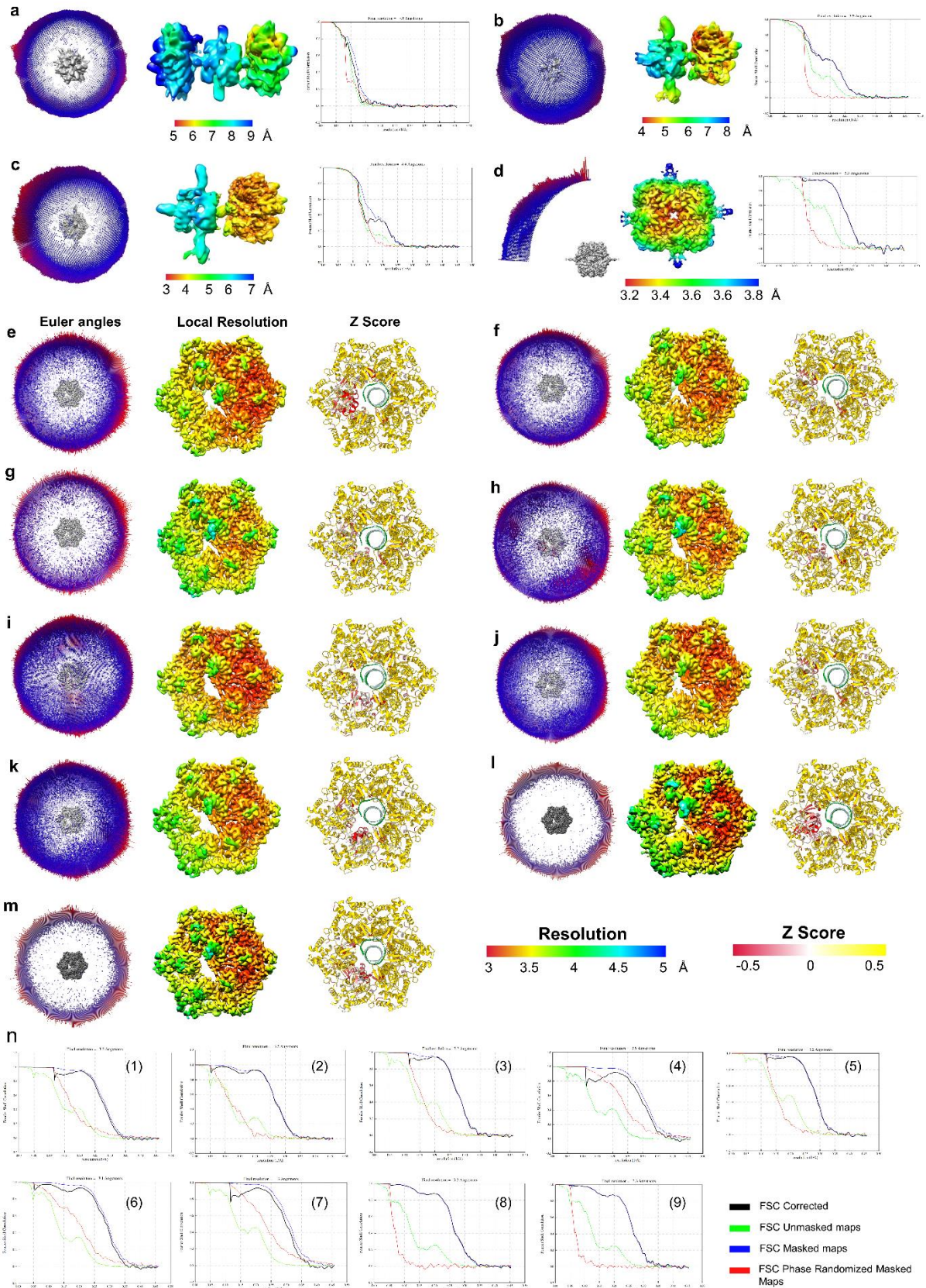
Models are shown in ribbon cartoons with stick representation.

**Extended Data Fig 6. Assembly strategy of the low and high resolution composite maps.**

a, 3D-reconstructed pseudo bipartite particles (top) were rigid body-fitted into the consensus reconstruction of the tripartite RuvAB-HJ particle (middle) using the *fit in map* tool in ChimeraX. Individual maps were then combined into one composite map (bottom), using the *volume add* tool ChimeraX.

b, To generate the high-resolution composite map, four components were used: the cryo-EM density corresponding to the HJ in composite map 1, two focus-refined RuvB motors (s2t2) and the focus-refined RuvA-HJ complex, lacking the HJ. The four components were fitted into composite map 1 and then combined as described before.

# Extended Data Figure 7



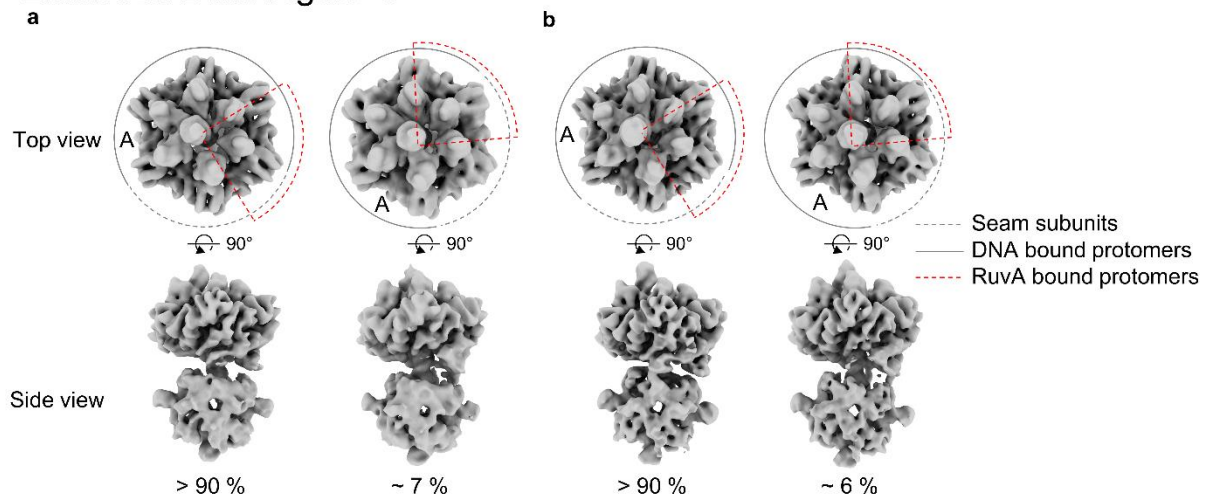
### **Extended Data Fig 7. Single particle reconstructions.**

a-d, Angular distribution plots, local resolution estimations and Fourier Shell Correlation (FSC) plots of C1 reconstruction of the tripartite RuvAB-HJ complex (a), the pseudo-bipartite RuvAB-HJ complex (b), the bipartite RuvAB-HJ complex (c) and the RuvA-HJ core complex (d) from the t2 dataset.

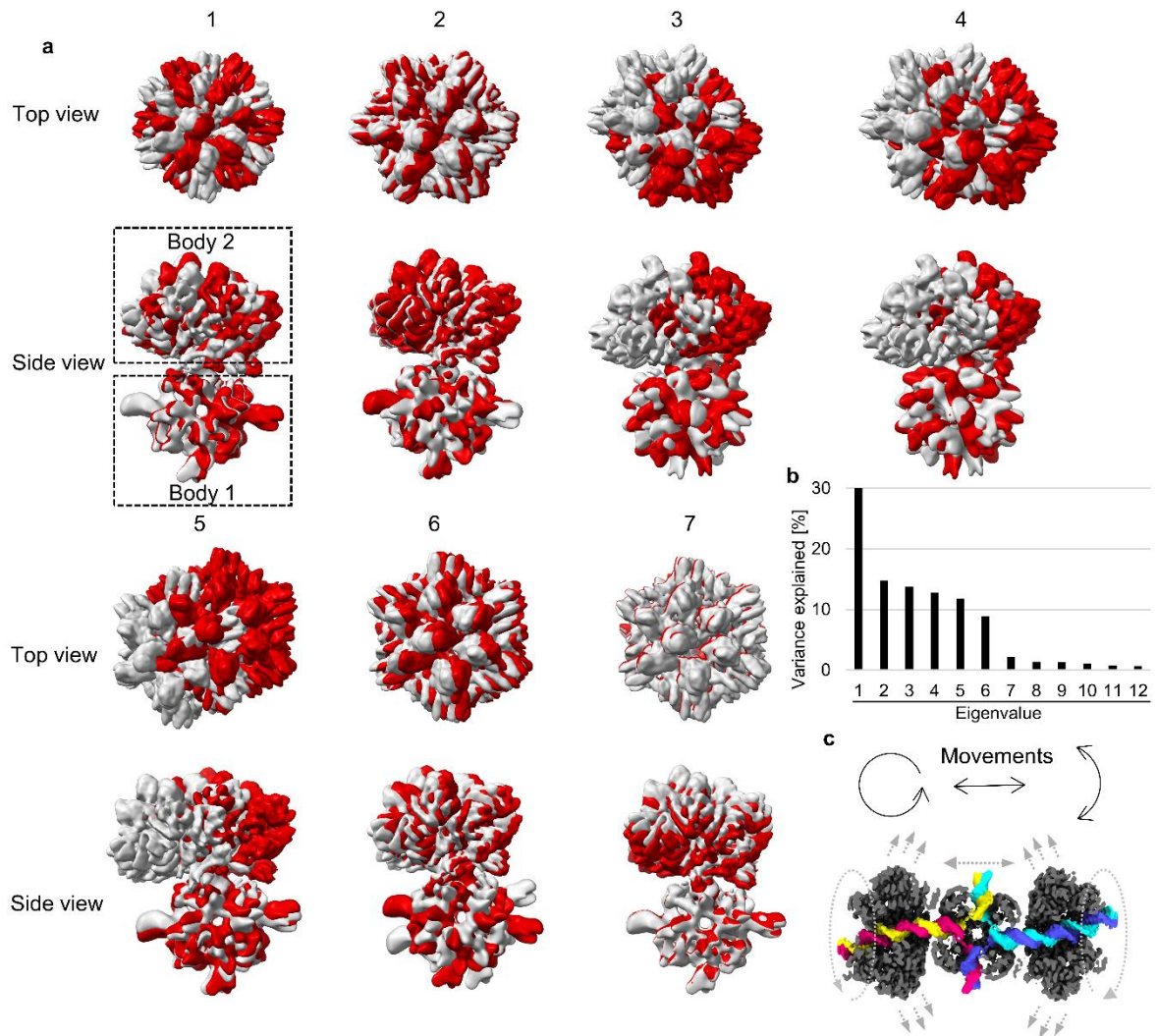
e-m, Angular distribution plots, local resolution estimations and Z-scores of the RuvB motor states: s1<sub>t2</sub> (e), s2<sub>t2</sub> (f), s3<sub>t2</sub> (g), s4<sub>t2</sub> (h), s5<sub>t2</sub> (i), s0<sub>t2</sub><sup>+A</sup> (j), s0<sub>t2</sub><sup>-A</sup> (k), s1<sub>t1</sub> (l) and s0<sub>t1</sub><sup>+A</sup> (m).

n, Fourier Shell Correlation (FSC) plots of the RuvB motor reconstructions: s1<sub>t2</sub> (1), s2<sub>t2</sub> (2), s3<sub>t2</sub> (3), s4<sub>t2</sub> (4), s5<sub>t2</sub> (5), s0<sub>t2</sub><sup>+A</sup> (6), s0<sub>t2</sub><sup>-A</sup> (7), s1<sub>t1</sub> (8) and s0<sub>t1</sub><sup>+A</sup> (9).

## Extended Data Figure 8



## Extended Data Figure 9



**Extended Data Fig 8. 3D classes showing the rotation of the RuvB motor.**

a, 3D class containing ~7 % of the bipartite RuvAB-HJ particles that show the 60° counterclockwise rotation of the RuvB motor with respect to the RuvA-HJ core complex.

b, 3D class containing ~6 % of the pseudo-bipartite RuvAB-HJ particles that show the 60° counterclockwise rotation of the RuvB motor with respect to the RuvA-HJ core complex.

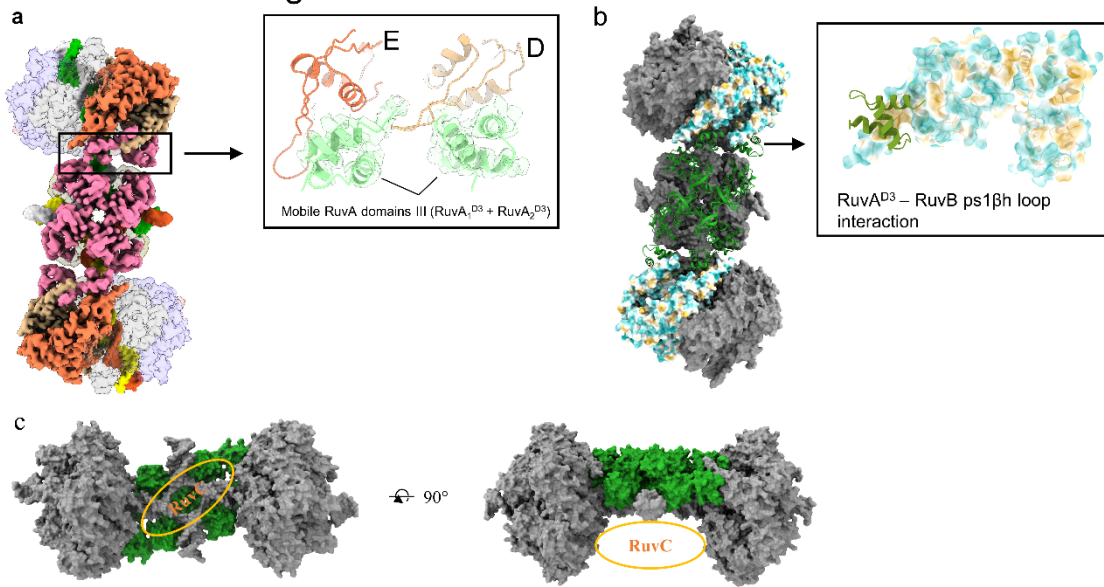
**Extended Data Fig 9. 3D Multibody refinement analysis of the highly-flexible bipartite RuvAB-HJ particles.**

a, Following the principal component analysis, maps corresponding to the seven most abundant eigenvectors were generated using the *multibody refinement* tool in RELION3<sup>49</sup>. Two maps are shown for each of the seven motions with the grey and red colors representing the start and end point of these movements, respectively. Since the eigenvectors represent relative motions between RuvA-HJ (Body 1) and RuvB (Body 2), e.g. maps 1 and 2 represent comparable motions.

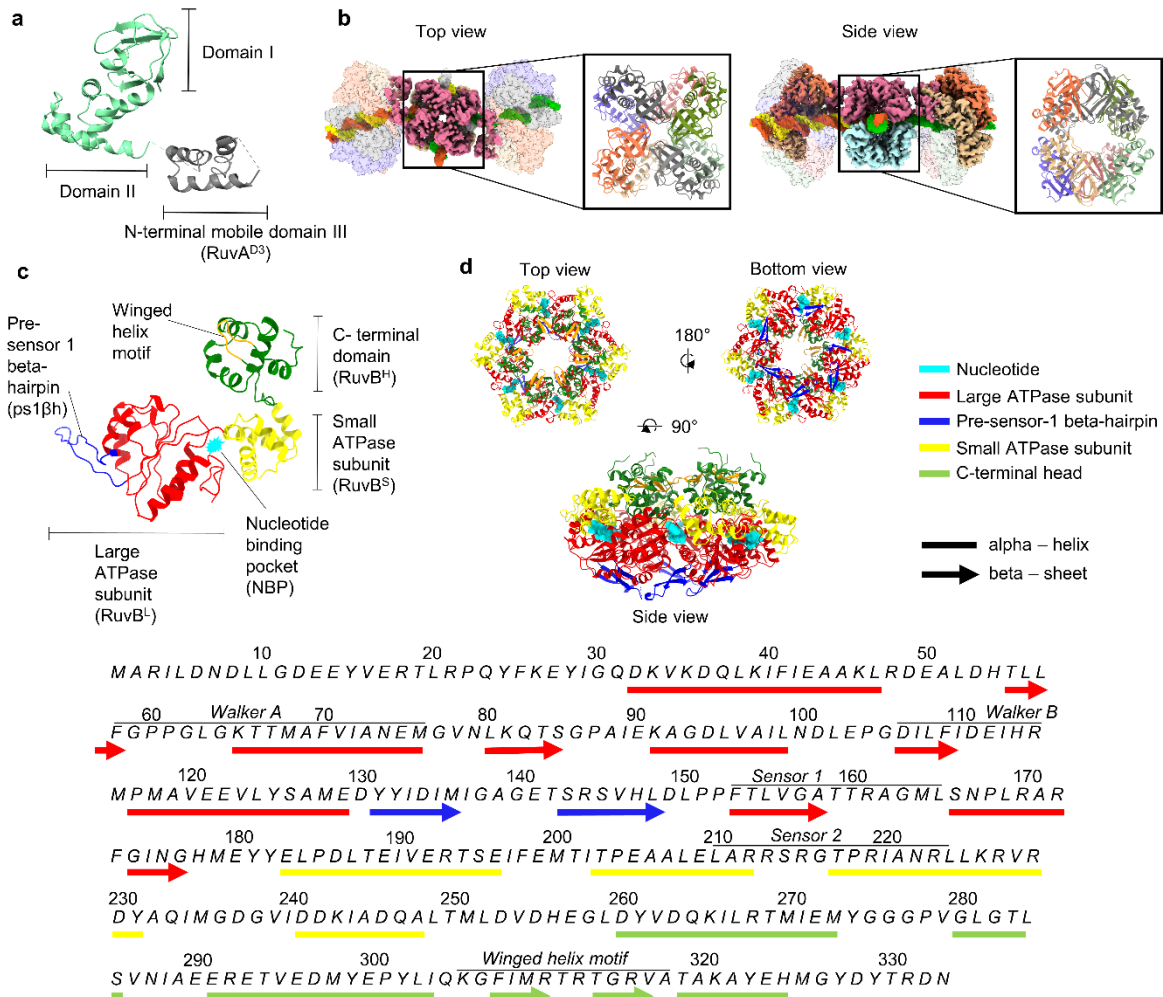
b, Contribution of each of the twelve eigenvectors to the overall variance (in %). The first 7 eigenvectors cover ~95 % of all movements. The rotational motions of eigenvectors 1 and 2, together, cover ~45 % of the variance. A wobbling motion of the RuvB motor with respect to the RuvA core is represented by the eigenvectors 3-6 and amount to ~47.5 % of the variance. The motion increasing the gap size (bouncing) between the two bodies (eigenvector 7) covers ~2.5 % of the observed variance.

c, Illustration of the directionalities corresponding to the three predominant trajectories: rotation (45 %), wobbling (47.5 %) and bouncing (2.5 %).

## Extended Data Figure 10



## Extended Data Figure 11



**Extended Data Fig 10. Two RuvA<sup>D3</sup> domains bind to the adjacent RuvB protomers.**

a, RuvAB-HJ composite map, highlighting the RuvA tetramer sitting on top of the HJ crossover. The four RuvA<sup>D3</sup> domains localize to the same side of the HJ crossover, suggesting that one RuvA tetramer might be sufficient to operate the RuvAB-HJ machinery. RuvA proteins are depicted in purple. RuvB protomers RuvB<sub>4</sub> (cluster D) and RuvB<sub>5</sub> (cluster E) are shown in orange and beige, respectively. The magnification highlights the two adjacently-located binding interfaces.

b, A hydrophobic interaction of RuvA<sup>D3</sup> is established with the helix  $\alpha 3$  and the presensor-1  $\beta$  hairpin (ps1 $\beta$ h) of RuvB<sup>15</sup>. Surface representation of RuvB with hydrophilic amino acids shown in turquoise and hydrophobic residues shown in sepia. A cartoon model of only one RuvA<sup>D3</sup> domain is shown.

c, Putative model of the RuvABC-HJ resolvosome, in which one RuvA tetramer binds the HJ crossover and operates both RuvB motors simultaneously. A dimer of the RuvC resolvase would bind the HJ crossover in the location otherwise occupied by the second RuvA tetramer.

**Extended Data Fig 11. RuvA and RuvB protomers and their oligomeric organization within the RuvAB-HJ branch migration complex.**

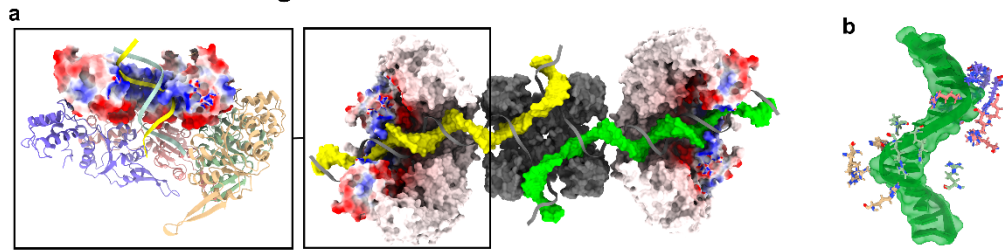
a, RuvA consists of three domains. Domains I and II (green) are responsible for binding the HJ and the oligomerization into tetramers, whereas domain III (grey) binds to the RuvB motor.

b, Double-tetrameric organization of the RuvA core complex containing only the RuvA domains I and II, suggesting that in the operational RuvAB-HJ machinery all eight RuvA<sup>D3</sup> domains are dislodged from the central core complex. Magnifications highlight the individual RuvA protomers constituting the central core by different colors.

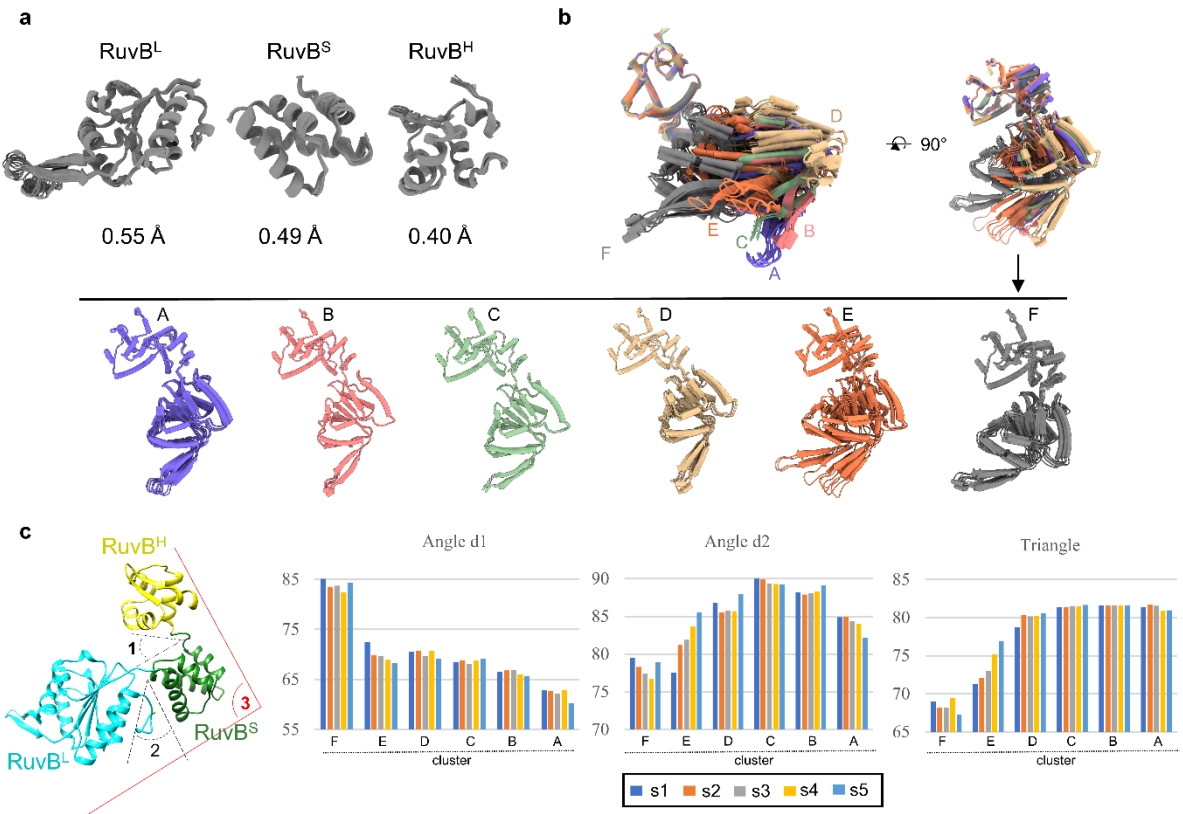
c, RuvB consists of two domains. A large (RuvB<sup>L</sup>) and a small (RuvB<sup>S</sup>) ATPase subdomain, together forming the ATP-binding domain, and a C-terminal “head” domain (RuvB<sup>H</sup>) binding the DNA substrate via a winged-helix motif.

d, Hexameric assembly of the RuvB motor, using the domain color code in c. Akin to other hexameric AAA+ translocases, the nucleotide binding pocket (NBP) is located between adjacent protomers to enable nucleotide-dependent interprotomer signaling.

### Extended Data Figure 12



### Extended Data Figure 13



**Extended Data Fig 12. Spiral staircase organization of the DNA binding interface in RuvB motors.**

a, Charge distribution representation of the RuvB<sup>H</sup> domains in the RuvB motor staircase. The RuvB<sup>H</sup> domains of protomers RuvB<sub>1-4</sub> (clusters A-D) form a positively-charged pit to stably accommodate one strand of the double-stranded DNA substrate. One strand of each DNA substrate (green/yellow) is processed by one RuvB motor.

b, Superposition analysis of the five ATP hydrolysis cycle states (s<sub>1t2</sub>-s<sub>5t2</sub>), highlighting the almost invariable DNA binding interface formed by the conserved arginine residues (Arg291, Arg310, Arg312 and Arg315) in the RuvB<sup>H</sup> domains.

**Extended Data Fig 13. Superposition and geometrical analysis of RuvB protomers.**

a, Superposition of RuvB<sup>L</sup>, RuvB<sup>S</sup> and RuvB<sup>H</sup> domains. Domains belong to the RuvB protomers of the RuvB motor states obtained in the t2 dataset (s<sub>1t2</sub>-s<sub>5t2</sub>, s<sub>0t2</sub><sup>+A</sup> and s<sub>0t2</sub><sup>-A</sup>). Low RMSD<sub>C $\alpha$</sub>  values demonstrate that RuvB domains move as rigid bodies in the ATP hydrolysis cycle of the RuvB motor.

b, Superposition of the RuvB protomers on the RuvB<sup>H</sup> domain including the protomers from the states s<sub>1t2</sub>-s<sub>5t2</sub>, s<sub>0t2</sub><sup>+A</sup> and s<sub>0t2</sub><sup>-A</sup> in the t2 dataset. The analysis reveals RuvB protomers form conformational clusters, which reflect their position in the RuvB hexamer. Colors indicate conformational clusters (A-F). Notably, RuvB<sub>5</sub> of the initiation states s<sub>0t2</sub><sup>+A</sup> and s<sub>0t2</sub><sup>-A</sup> groups into cluster F instead of cluster E, highlighting the hybrid conformation of the *converter* module in these states.

c, Angle measurements in the RuvB protomers from the ATP hydrolysis cycle states (s<sub>1t2</sub>-s<sub>5t2</sub>) in the t2 dataset. Two dihedral angles (d1 between RuvB<sup>L</sup> and RuvB<sup>S</sup> and d2 between RuvB<sup>S</sup> and RuvB<sup>H</sup>) and one triangle angle (between the mass centers of RuvB<sup>L</sup>:RuvB<sup>S</sup>:RuvB<sup>H</sup>) are plotted. Averaged values of the d1 and 2 angles are shown Fig. 3a. When reading from the left (cluster F) to the right (cluster A), the plotted angular changes correspond to the conformational changes of a RuvB protomer, running through the ATP hydrolysis cycle in the RuvB motor. Bar colors correspond to the ATP hydrolysis cycle states.



**Extended Data Fig 14. Sequential movements of the *converter* module in the ATP hydrolytic cycle.**

a, Superposition of the ATP hydrolysis cycle states (s1<sub>t2</sub>-s5<sub>t2</sub>) on almost invariable RuvB<sub>3</sub> (cluster C), highlighting the conformational changes in the *converter* module RuvB protomers RuvB<sub>6</sub>, RuvB<sub>5</sub> and RuvB<sub>4</sub><sup>L</sup>.

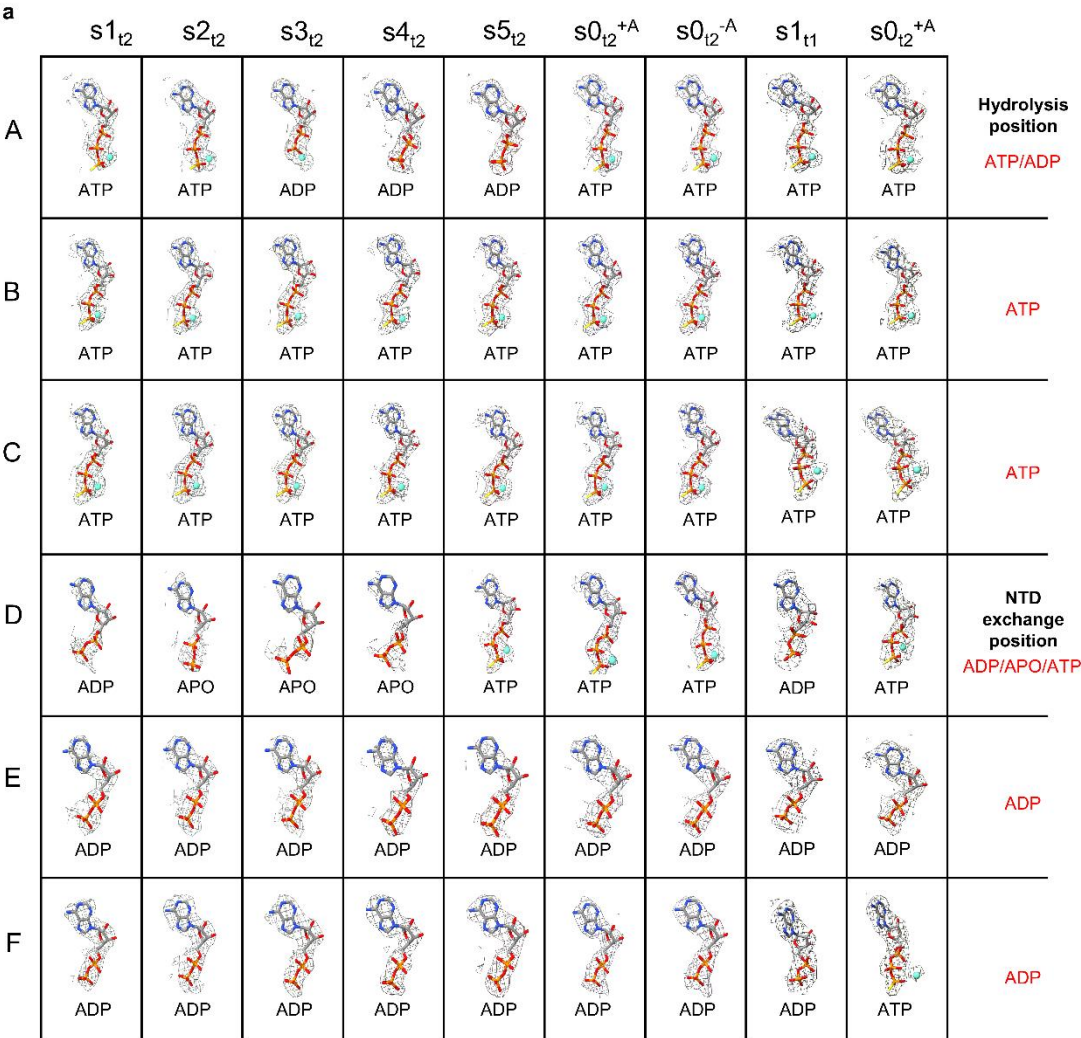
b, Motion analysis of the *converter* module based on the superposition shown in a. Arrows indicate the magnitude (distance in Å) and directionality of the motion between matching C<sub>α</sub>-atom pairs. For improved visibility a cut-off of 1 Å was chosen and arrows are shown only for C<sub>α</sub>-atom pairs corresponding to every second residue. Arrows in the transition from s1<sub>t2</sub> to s2<sub>t2</sub> highlight the wedge-like effect occurring between RuvB<sub>4</sub> (cluster D) and RuvB<sub>5</sub> (cluster E) and resulting in the long-range interprotomer signaling that is needed to stimulate ATP hydrolysis and nucleotide exchange. Arrows in the transition from s3<sub>t2</sub> to s4<sub>t2</sub> emphasise the retrograde interprotomer signaling corresponding to the loss of the Mg<sup>2+</sup> ion in the RuvB<sub>1</sub> NBP upon completion of the ATP hydrolysis reaction. Retrograde signaling affects mainly RuvB<sub>6</sub> (cluster F) and RuvB<sub>5</sub> (cluster E) and is associated with retraction of the N terminus from the RuvB<sub>5</sub> in preparation of this RuvB protomer for nucleotide exchange in the next translocation step. Arrows in the transition from s4<sub>t2</sub> to s5<sub>t2</sub> highlight the interprotomer signaling associated with the acquisition of a new ATP molecule, which affects the entire *converter* module. RuvB<sub>5</sub> (cluster E), located in the center of the *converter* module, is framed with a red line to aid visibility.

c, Plotted distances (in Å) of matching C<sub>α</sub>-atom pairs in the RuvB protomers RuvB<sub>4</sub>, RuvB<sub>5</sub> and RuvB<sub>6</sub> of clusters D, E and F, respectively, measured based on the superposition shown in a. The analysis reveals that the RuvB<sub>4</sub><sup>S</sup> and RuvB<sub>4</sub><sup>H</sup> domains are not part of the *converter* module. The box indicates the unidirectional trajectory observed for RuvB<sub>5</sub> in cluster E. RuvB<sub>1</sub> (cluster A) is shown to highlight the motions of RuvB<sub>1</sub><sup>S</sup> and RuvB<sub>1</sub><sup>H</sup>, that are associated with the progressing ATP hydrolysis reaction in the RuvB<sub>1</sub> NBP and contribute to the priming of the RuvB motor for a *cluster switch*.

d, Motions of the RuvB<sub>1</sub><sup>S</sup> and RuvB<sub>1</sub><sup>H</sup> domains (cluster A) during the ATP hydrolysis cycle (s1<sub>t2</sub>-s5<sub>t2</sub>), assessed using the superposition shown in a. RuvB<sub>1</sub><sup>H</sup> approaches substrate-disengaged RuvB<sub>6</sub>, indicating ATP hydrolysis functions to prime RuvB<sub>1</sub> for substrate release.

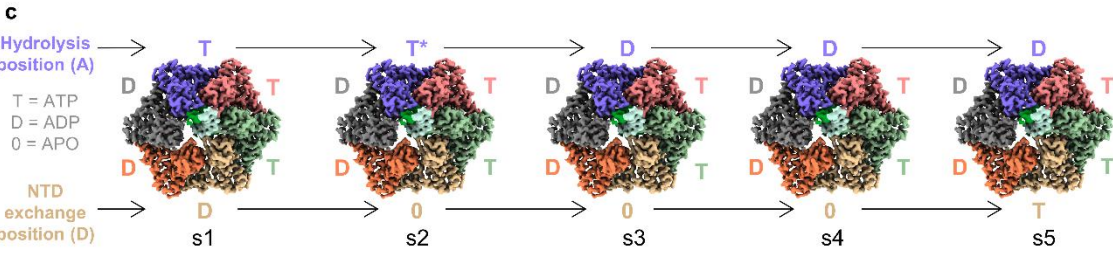
e, Motion of the RuvB5<sup>H</sup> domain (cluster E) during the ATP hydrolysis cycle (s1<sub>t2</sub>-s5<sub>t2</sub>), assessed using the superposition shown in a. The RuvB5<sup>H</sup> domain approaches the minor groove of the DNA substrate, indicating that the ATP hydrolysis cycle primes RuvB<sub>5</sub> for substrate binding.

# Extended Data Figure 15



**b**

	s1	s2	s3	s4	s5	s0 <sup>+A</sup>	s0 <sup>-A</sup>	s5* (t1)	s0 <sup>+A</sup> (t1)
<b>A/1</b>	ATP	ATP	ADP	ADP	ADP	ATP	ATP	ADP	ATP
<b>B/2</b>	ATP	ATP	ATP	ATP	ATP	ATP	ATP	ATP	ATP
<b>C/3</b>	ATP	ATP	ATP	ATP	ATP	ATP	ATP	ATP	ATP
<b>D/4</b>	ADP	APO	APO	APO	ATP	ATP	ATP	ATP	ATP
<b>E/5</b>	ADP	ADP	ADP	ADP	ADP	ADP	ADP	ADP	ADP
<b>F/6</b>	ADP	ADP	ADP	ADP	ADP	ADP	ADP	ADP	ATP*



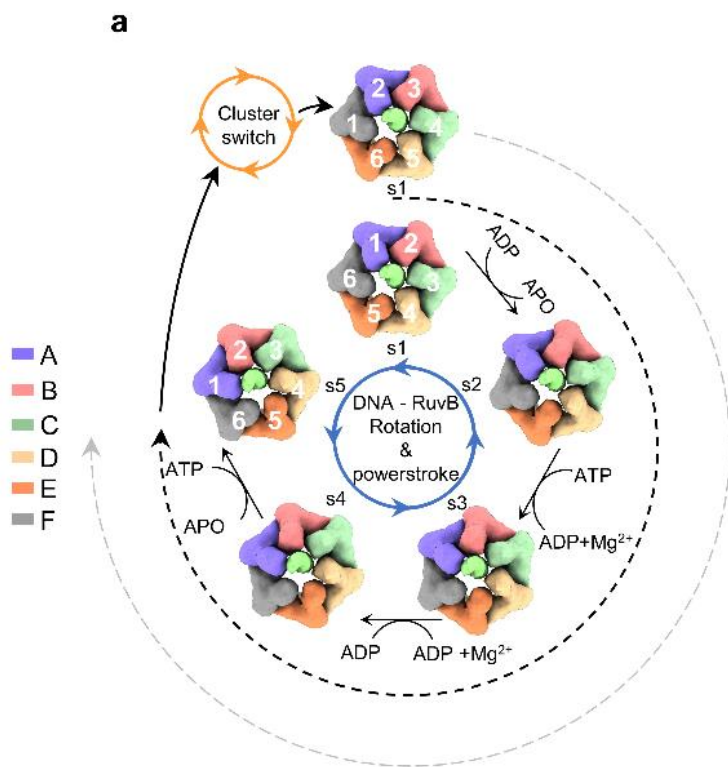
**Extended Data Fig 15. Coexisting nucleotides in the different RuvB motor states.**

a, Modelled nucleotides and their corresponding cryo-EM densities in the nucleotide binding pockets of the RuvB motor states corresponding to the t2 dataset ( $s_{1t2}$ ,  $s_{2t2}$ ,  $s_{3t2}$ ,  $s_{4t2}$ ,  $s_{5t2}$ ,  $s_{0t2}^{+A}$ ,  $s_{0t2}^{-A}$ ) and the t1 dataset ( $s_{1t1}$  and  $s_{0t1}^{+A}$ ). Note that, although nucleotides are labeled with ATP, ATP $\gamma$ S has been used in this study and has been modeled.

b, Table listing the nucleotides in the RuvB NBPs, according to the RuvB protomer/cluster and the RuvB motor state. The table exemplifies that the ATP hydrolysis cycle ( $s_{1t2}$ - $s_{5t2}$ ) completes in state  $s_{5t2}$ , when the three RuvB protomers RuvB<sub>2-4</sub>, instead of RuvB<sub>1-3</sub>, are complexed with ATP.

c, Linear representation of the ATP hydrolysis cycle ( $s_{1t2}$ - $s_{5t2}$ ), visualizing its clockwise progression through the RuvB hexamer. To simplify the process, the counterclockwise rotation of the RuvB motor has been neglected.

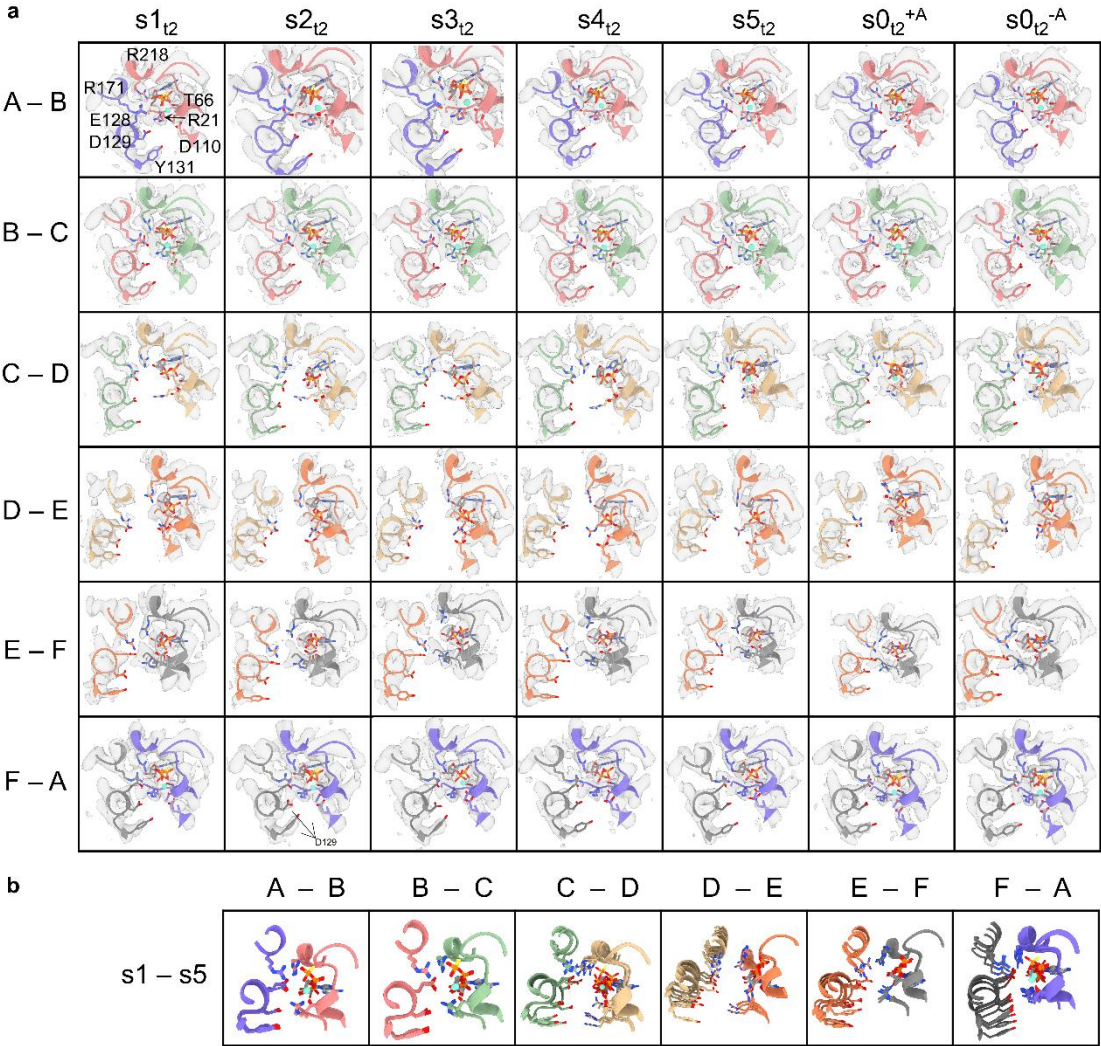
## Extended Data Figure 16



### Extended Data Fig 16. Model of one translocation step in the RuvB motor.

a, Circular representation of one translocation step in the RuvB motor. During the events of the ATP hydrolysis cycle ( $s_{1_{12}}-s_{5_{12}}$ ), the RuvB motor undergoes a counterclockwise rotation. Therefore, at the end of the rotational motion in  $s_{5_{12}}$ , RuvB motors take the position of their counterclockwise-adjacent neighbors (e.g. RuvB<sub>1</sub> in  $s_{1_{12}}$  rotates into the position RuvB<sub>6</sub>). The completion of the ATP hydrolysis cycle in  $s_{5_{12}}$  not only provides the nucleotide configuration that is necessary to run the next ATP hydrolysis cycle, but also primes the RuvB motor to perform a *cluster switch*. The *cluster switch* coincides with the hand over of the DNA inside the inner pore from RuvB<sub>1-4</sub> to RuvB<sub>2-5</sub>. This enables RuvB motors to perform the next ATP hydrolysis cycle with ATP hydrolysis and nucleotide exchange occurring in the RuvB<sub>2</sub> NBP and the RuvB<sub>5</sub> NBP, respectively. Colors indicate conformational clusters.

# Extended Data Figure 17

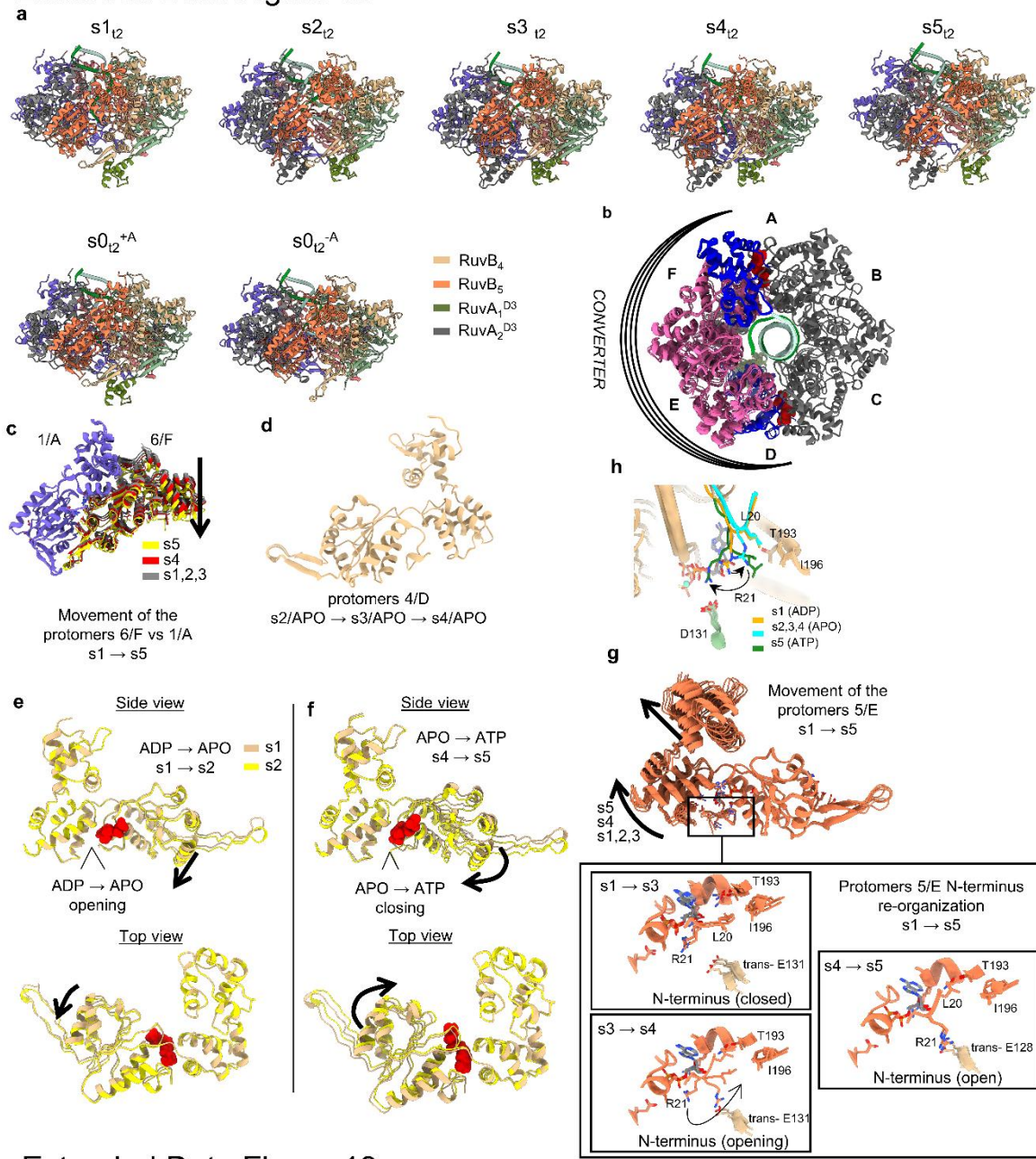


**Extended Data Fig 17. Opening and closing motions of the RuvB NBP interprotomer interface during the ATP hydrolysis cycle.**

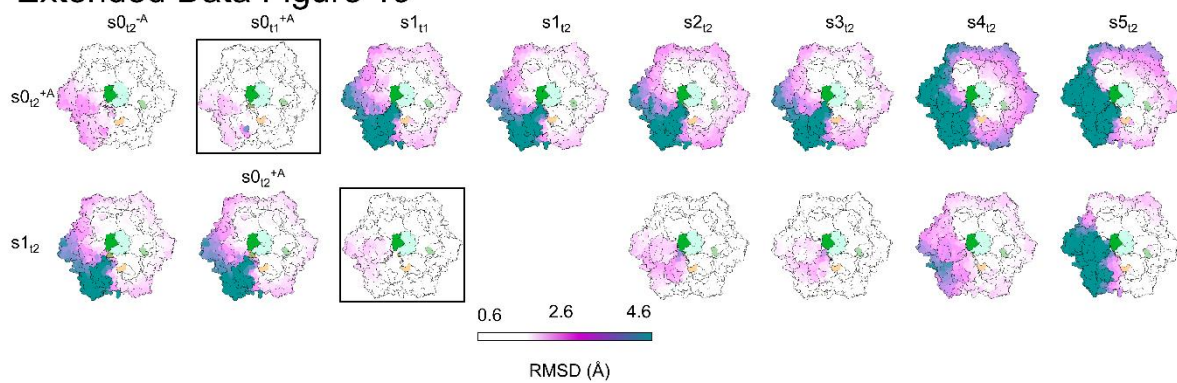
a, Cryo-EM density (grey) and corresponding atomic models (cartoons) of all RuvB NBP interprotomer interfaces determined in this study. The cryo-EM density has been contoured at the threshold level of 0.026. Residues contributing to ATP-binding and ATP hydrolysis are shown in stick representation.

b, Superpositions of the RuvB NBP interprotomer interfaces according to their clusters (A-F), using the respective nucleotide-bound *cis*-protomer from state s1<sub>12</sub> as an alignment reference to illustrate the movement of both protomers contributing to the interface across the five ATP hydrolysis cycle states (s1<sub>12</sub>-s5<sub>12</sub>). The interfaces between clusters A-B and clusters B-C are almost invariant. The interface between cluster F and A highlights the motion of RuvB<sub>6</sub>, which triggers ATP hydrolysis in cluster A. The higher variability of the remaining interfaces reflects the plasticity of the substrate-disengaged RuvB protomers and RuvB<sub>4</sub> in cluster D, which together form the *converter* module.

# Extended Data Figure 18



# Extended Data Figure 19



**Extended Data Fig 18. Conformational changes in the *converter* module.**

a, Side-by-side comparison of the atomic models corresponding to the RuvB motors states in the ATP hydrolysis cycle ( $s_{1t2}$ - $s_{5t2}$ ) and the initiation states ( $s_{0t2}^{-A}$ ,  $s_{0t2}^{+A}$ ) obtained from dataset t2.

b, Superposition of the RuvB motor states  $s_{1t2}$ - $s_{5t2}$  (top view) on the almost invariant RuvB protomer RuvB<sub>3</sub> (cluster C). Colors correspond to the variance analysis shown in Fig. 2d with grey (RuvB<sub>1</sub><sup>L</sup>, RuvB<sub>2</sub>, RuvB<sub>3</sub>, RuvB<sub>4</sub><sup>S+H</sup>), blue (domains of border protomers RuvB<sub>1</sub><sup>S+H</sup> and RuvB<sub>4</sub><sup>L</sup>) and purple (RuvB<sub>5</sub> and RuvB<sub>6</sub>) representing a low, medium and high variance, respectively. The *converter* module connects the ATP-hydrolysing NBP of RuvB<sub>1</sub> (cluster A) with the nucleotide-exchanging NBP of RuvB<sub>4</sub> (cluster D). Lines indicate the downwards-directed motion of the *converter* module during the ATP hydrolysis cycle. The nucleotides in the NBPs of RuvB<sub>1</sub> and RuvB<sub>4</sub> are shown in surface representation and highlighted in red.

c, Unidirectional motion of RuvB<sub>6</sub> (cluster F) with respect to RuvB<sub>1</sub> (cluster A) during the ATP hydrolysis cycle. The largest motion occurs in the transition from state  $s_{4t2}$  (yellow) to  $s_{5t2}$  (red), when the ATP hydrolysis reaction is completed and the Mg<sup>2+</sup> has dissociated from the ADP in the RuvB<sub>1</sub> NBP in cluster A.

d, Superposition analysis of the nucleotide exchange facilitating RuvB<sub>4</sub> (cluster D) from states  $s_{2t2}$ ,  $s_{3t2}$  and  $s_{4t2}$ . A low average RMSD<sub>C $\alpha$</sub>  of 0.3 Å reveals that RuvB<sub>4</sub> protomers remain almost invariable during the three APO states.

e-f, Domain rearrangements associated with nucleotide exchange in RuvB<sub>4</sub> (cluster D) in the transition from state  $s_{1t2}$  to  $s_{2t2}$  (ADP→APO) and from state  $s_{4t2}$  to  $s_{5t2}$  (APO→ATP). Nucleotides are shown in surface representation and highlighted in red. To visualize the motions, RuvB protomers were superimposed on the RuvB<sub>4</sub><sup>H</sup> domain.

g-h, Opening (g) and closing (h) motion of the RuvB N terminus during the progression of the ATP hydrolysis cycle. Note that the opening motion is mainly visible in RuvB<sub>5</sub> (cluster E), while the closing motion is associated with the acquisition of a new ATP molecule and can therefore only be observed in RuvB<sub>4</sub> (cluster D). Hence, the motions of the RuvB N terminus occur over more than one translocation step.

## Extended Data Table 1

Sample vitrification	
Buffer	25 mM Tris-HCL pH 8, 100 mM NaCl, 10 mM MgCl <sub>2</sub> , 0.2 – 0.4 % glycerol, 0.005 % DDM, 0.5 mM ATPyS, 0.5 mM ADP
Grid	Quantifoil Au 2/1, 300 mesh, with ~1.2 nm thick floated carbon
Blotting	VitroBot Mark IV 4-6 seconds with 2 minutes pre-blotting incubation, 4° C, 100 % humidity,
Data collection	
Microscope	Thermo Fisher Scientific Titan Krios
Nominal magnification	81kx (t1) 130kx (t2)
Voltage (kV)	300
Detector	Gatan K3 (t1) Gatan K2 Summit (t2)
Energy filter slit (eV)	10
Pixel size (Å)	1.1 (t1) 1.09 (t2)
Total electron dose (e-/Å <sup>2</sup> )	53.3 (t1) 30.72 (t2)
Exposure time (sec)	3 (t1) 5 (t2)
Movie frames	33 (t1) 20/25 (t2)
Dose per frame (e-/Å <sup>2</sup> )	1.6 (t1) 1.23/1.54 (t2)
Defocus range (µm)	-0.5 to -3
Movies collected	10057 (t1) 30083 (t2)
Picked poordinates	> 4.000.000 (t1) > 7.000.000 (t2)

**Extended Data Fig 19. Plasticity of the *converter* module in the RuvB motor.**

Structural plasticity of the *converter* module measured by the  $\text{RMSD}_{C\alpha}$  (in Å) measured between all RuvB motor states obtained in this study (t1 and t2 dataset). States were aligned to the DNA. Colors indicate the  $\text{RMSD}_{C\alpha}$  (in Å). In the top panel, initiation state  $s_{0_{t2}^{+A}}$  served as a reference. The two most similar states are the states  $s_{0_{t1}^{+A}}$  (boxed) and the RuvA<sup>D3</sup>-free state  $s_{0_{t2}^{-A}}$ , obtained from RuvB-HJ particles. In the lower panel, ATP hydrolysis cycle state  $s_{1_{t2}}$  served as a reference. The most similar state is  $s_{1_{t1}}$  (boxed). In both cases, the comparison with states  $s_{2_{t2}}$ - $s_{5_{t2}}$  highlight that motions of RuvB protomers are largest in the *converter* module.

**Extended Data Table 1. Cryo-EM sample vitrification and data collection.**

**Extended Data Table 2. Cryo-EM Single-particle-analysis processing summary.**

**Extended Data Table 3. Model building summary.**

**Extended Data Table 4. List of DNA primers used in this study.**

## Extended Data Table 2

Data processing t2/t1 (RuvAB-HJ Full and Half)			
Map	RuvAB-HJ (Full)	RuvAB-HJ (Half subtracted)	RuvAB-HJ (half original)
Number of pre-cleaned particle images	635.000/948.812	1.3700.00	382.605/0
Number of final particles images	529.554	1.079.144	291.007
Map resolution (FSC 0.143)	8	4.4	3.9
Map sharpening B-factor (Å)	- 10 (manual)	- 20 (manual)	- 20 (manual)
symmetry	C1	C1	C1

Data processing t2 (RuvA and RuvB)								
Map	RuvA-HJ	RuvB s1	RuvB s2	RuvB s3	RuvB s4	RuvB s5	RuvB s0 <sup>+A</sup>	RuvB s0 <sup>-A</sup>
Number of pre-cleaned particle images	229000	~2.300.000						
Number of final particles images	31.291	102.619	32.612	77.587	77.356	125.425	62.542	96.370
Map resolution (FSC 0.143)	3.3	3.2	3.2	3.2	2.9	3.2	3.1	3
Map sharpening B-factor (Å)	- 79	- 45	- 41	- 50	- 33	- 46	- 35	- 30
symmetry	D4	C1	C1	C1	C1	C1	C1	C1

Data processing t1 (RuvA and RuvB)			
Map	RuvA-HJ	RuvB s1 (st1)	RuvB s0 <sup>+A</sup> (st2)
Number of pre-cleaned particle images	948.812	1.881.624	
Number of final particles images	430.000	41.209	45.834
Map resolution (FSC 0.143)	3.1	3.3	3.3
Map sharpening B-factor (Å)	- 132	- 43	- 47
symmetry	D4	C1	C1

Extended Data Table 3

	RuvA	RuvB s1	RuvB s2	RuvB s3	RuvB s4	RuvB s5	RuvB s0 <sup>+A</sup>	RuvB s0 <sup>-A</sup>	RuvB s1 <sup>*</sup>	RuvB s0 <sup>*+A</sup>
Model composition										
Non-hydrogen atoms	8342	1588 3	1626 4	1626 0	1625 9	1626 4	1588 8	15531	15965	15893
Protein residues	1063	1918	1968	1968	1968	1968	1918	1870	1918	1918
Ligands	-	30	30	30	30	30	30	30	30	30
B factors (Å <sup>2</sup> mean)										
Protein (mean)	83.68	79.68	61.73	64.67	63.03	73.46	68.80	67.48	82.51	86.97
Ligand	-	67.16	57.22	57.05	57.64	58.52	62.27	60.82	72.96	74.71
R.m.s. deviations										
Bond lengths (Å)	0.005	0.004	0.004	0.004	0.004	0.004	0.004	0.004	0.004	0.005
Bond angles (°)	0.781	0.695	0.715	0.726	0.739	0.726	0.717	0.717	0.705	0.712
Validation										
MolProbity score	0.66	0.88	0.83	0.83	0.83	0.89	0.88	0.88	0.81	0.91
Clashscore	0.47	1.43	1.15	1.18	1.24	1.49	1.43	1.43	1.05	1.59
Poor rotamers (%)	0	0.06	0.06	0.06	0.12	0.12	0.19	0.13	0.19	0.25
Ramachandran plot										
Favored (%)	99.04	98.84	98.92	98.97	98.97	99.03	98.79	99.19	99.0	99.26
Allowed (%)	0.96	1.16	1.08	1.03	1.03	0.97	1.21	0.81	1	0.74
Disallowed (%)	-	-	-	-	-	-	-	-	-	-
EMRinger Score	2.72	3.14	3.08	3.09	3.10	2.81	3.27	3.29	3.21	3.21
EMDB ID										
PDB ID										

Extended Data Table 4

Nr.	Name	Sequence (5' - 3')
1	wtRuvA_SB_1x - Fw	ATCTACGACCATGGTAGGCAGACTCAGAG
2	wtRuvA_SB_73ws1 Rw	GTGGCACCAGAGCGAGCTCTCAGTGATGGTGATGTAACGCGGC GCGTA
3	RuvB_Str_62b – Fw	ATCTAATGCCATGGTATACCCATACGATGTTCCAGATTACGCTGA GCGTACCCTTCGCCC
4	RuvB_Str_63 – Rw	AATTGTACAAGCTTTTAATTATCTCGAGTATAGTCATA
5	Hj-Y2ap_1	CTCATCGAGAATCTGCCGAGAGACCGAGCAGAATTCTATGTGTT TACCAAGCGCTG
6	Hj-Y2ap_2	CAGCGCTTGGTAAACACATAGAATTCTGCTCGGTCTGAGCCGTC TAAGAGACCTAG
7	Hj-Y2ap_3	CTAGGTCTCTTAGACGGCTCACTGGCTGTGGGATCCGAGCTGTC TAGAGACATCGA
8	Hj-Y2ap_4	TCGATGTCTCTAGACAGCTCGGATCCCACAGCCAGTCTCGGCAG ATTCTCGATGAG
9	HJ-X26	CCGCTACCAGTGATCACCAATGGATTGCTAGGACATCTTTGCC ACCTGCAGGTTCACCC
10	HJ-X26	TGGGTGAACCTGCAGGTGGGCAAAGATGTCCTAGCAATCCATTG TCTATGACGTCAAGCT
11	HJ-X26	GAGCTTGACGTCATAGACAATGGATTGCTAGGACATCTTTGCCG TCTTGTC AATATCGGC
12	HJ-X26	TGCCGATATTGACAAGACGGCAAAGATGTCCTAGCAATCCATTG GTGATCACTGGTAGCGG

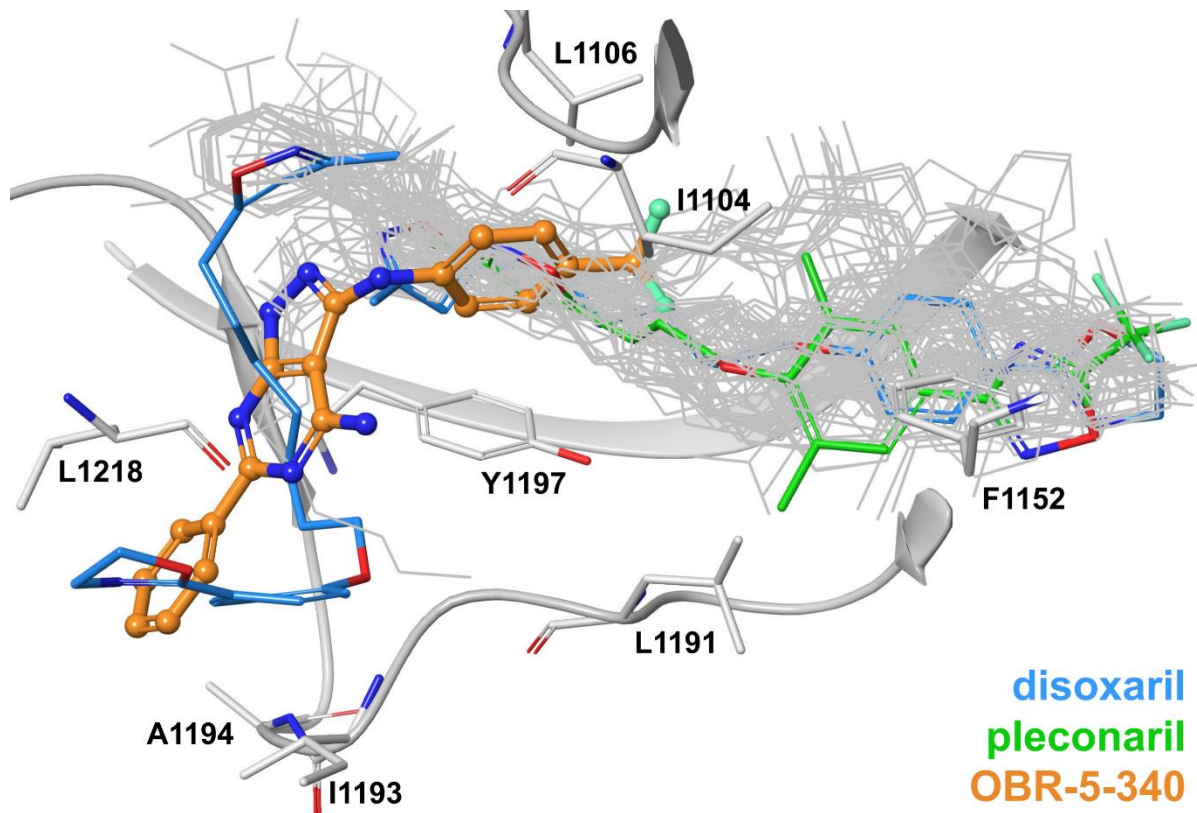


## Chapter 2:

# Cryo-EM structure of pleconaril-resistant rhinovirus-B5 complexed to the antiviral OBR-5-340 reveals unexpected binding site

*Published on September 17, 2019 as:*

**Jiri Wald**, Marion Pasin, Martina Richter, Christin Walther, Neann Mathai, Johannes Kirchmair, Vadim A. Makarov, Nikolaus Goessweiner-Mohr, Thomas C. Marlovits, Irene Zanella, Antonio Real-Hohn, Nuria Verdaguer, Dieter Blaas, and Michaela Schmidtke. (2019). Cryo-EM structure of pleconaril-resistant rhinovirus-B5 complexed to the antiviral OBR-5-340 reveals unexpected binding site. PNAS, 116 (38) 19109-19115, <https://doi.org/10.1073/pnas.1904732116>



# **Cryo-EM Structure of Pleconaril-Resistant Rhinovirus-B5 Complexed to the Antiviral OBR-5-340 Reveals Unexpected Binding Site**

Jiri Wald<sup>1,\*</sup>, Marion Pasin<sup>2,\*</sup>, Martina Richter<sup>3,\*</sup>, Christin Walther<sup>3,\*</sup>, Neann Mathai<sup>4</sup>, Johannes Kirchmair<sup>4</sup>, Vadim A. Makarov<sup>5</sup>, Nikolaus Gössweiner-Mohr<sup>6</sup>, Thomas C. Marlovits<sup>1</sup>, Irene Zanella<sup>2</sup>, Antonio Real-Hohn<sup>2</sup>, Nuria Verdaguer<sup>7</sup>, Dieter Blaas<sup>2,\*\*</sup>, and Michaela Schmidtke<sup>3,\*\*</sup>

1. Centre for Structural Systems Biology (CSSB), D-22607 Hamburg, Germany & University Medical Center, Hamburg-Eppendorf (UKE), Institute for Structural and Systems Biology D-22607 Hamburg, Germany & German Electron Synchrotron Centre (DESY), D-22607 Hamburg, Germany,

2. Max F. Perutz Laboratories, Department of Medical Biochemistry, Medical University of Vienna, A-1030 Vienna, Austria,

3. Jena University Hospital, Department Medical Microbiology, Section Experimental Virology, D-07740 Jena, Germany,

4. Department of Chemistry, University of Bergen, N-5020 Bergen, Norway & Computational Biology Unit (CBU), University of Bergen, N-5020 Bergen, Norway & University Hamburg, Centre for Bioinformatics, D-20146 Hamburg, Germany,

5. Federal Research Center Fundamentals of Biotechnology RAS, 119071 Moscow, Russia,

6. Institute of Biophysics, Johannes Kepler University Linz, A-4020 Linz, Austria,

7. Structural Biology Unit, Institute of Molecular Biology of Barcelona IBMB-CSIC, E-08028 Barcelona, Spain

\*these authors contributed equally to this work

\*\*corresponding authors

## **Acknowledgements**

Funded by the Austrian Science Fund (FWF) project #27444 to Dieter Blaas. Marion Pasin and Irene Zanella were supported by Erasmus fellowships. Neann Mathai and Johannes Kirchmair are supported by the Bergen Research Foundation (BFS) [BFS2017TMT01]. Thomas C. Marlovits is supported by funds through the Behörde für Wissenschaft, Forschung und Gleichstellung of the city of Hamburg. Data of RV-B5 and RV-A89, both plus OBR-5-340, were collected at the Vienna Biocenter Electron Microscopy Facility. Data collection of the control sample (RV-B5 without OBR-5-340), was funded by iNEXT grant 5950; we thank Pavel Plevka for freezing and Jirka Novacek for collecting the corresponding data. We thank David Haselbach for advice and help with Phenix and Coot, and Irene Goesler for virus production and purification.

## **Author contributions**

JK, TCM, AR-H, NV, DB, MS – designed research.

JK, TCM, DB, MS – supervised research.

JW, MP, MR, CW, NM, JK, IZ, ARH, DB – performed research.

VAM – contributed new reagents/analytic tools.

JW, MP, MR, CW, NM, JK, NGM, ARH, DB, MS – analysed data.

DB – reconstructed and refined the cryo-EM data.

MP – reconstructed and refined the cryo-EM data and carried out the thermal stability assays.

MR, CW, MS – carried out the antiviral tests.

NM – analysed binding sites of all compounds.

IZ – carried out stability assays.

NV – critically assessed the manuscript.

NM, JK, DB, MS – wrote the paper.

## Significance

More than 160 rhinovirus (RV) types cause about a billion respiratory infections annually in the US alone, contributing to influenza-like illness. Their high diversity makes vaccination impractical. Existing small-molecular weight inhibitors target many RVs by binding to a hydrophobic pocket in the capsid but exhibit side effects, resistance, and/or mutational escape, impeding registration with drug administration agencies. The pyrazolopyrimidine OBR-5-340 acts like other capsid-binders via preventing conformational changes required for genome release. However, by using cryo-EM, we show that OBR-5-340 inhibits the naturally pleconaril-resistant RV-B5 by attaching close to the pocket entrance, a binding geometry different from that of most capsid-binders. Combinations of inhibitors with disparate binding modes might thus effectively combat RVs while reducing the risk of resistance development.

## Abstract

Inhibitors, such as pleconaril and varendavir target conserved regions in viral capsid proteins of rhinoviruses (RVs) and enteroviruses (EVs). Such inhibitors bind to a hydrophobic pocket in viral capsid protein 1 (VP1). In resistant RVs and EVs, bulky residues in this pocket prevent their binding. However, recently developed pyrazolopyrimidines inhibit pleconaril-resistant RVs and EVs and computational modelling suggested that they also bind to the hydrophobic pocket in VP1. By using one of the seven naturally pleconaril-resistant rhinoviruses, RV-B5, and 3-(4-trifluoromethylphenyl)amino-6-phenylpyrazolo[3,4-d]pyrimidine-4-amine (OBR-5-340) as an example, we studied the mechanism of inhibition of pleconaril-resistant RVs by a bioavailable pyrazolopyrimidine with proven *in vivo* activity and determined the 3D-structure of their complex to 3.6 Å with cryo-electron microscopy. Our data indicate that similar to other capsid binders, OBR-5-340 induces thermostability and inhibits viral adsorption and uncoating. However, we found that OBR-5-340 attaches closer to the entrance of the pocket than most other capsid-binding inhibitors whose viral complexes have been studied so far, showing only marginal overlaps of the attachment sites. Comparing the experimentally-determined 3D-structure with the control, RV-B5 incubated with solvent only and determined to 3.2 Å, revealed no gross conformational changes upon OBR-5-340 binding. The pocket of the naturally OBR-5-340 resistant RV-A89 likewise incubated with the compound and solved to 2.9 Å was empty. As rigid, small molecules, pyrazolopyrimidines might be less affected by entropy loss upon binding and interact with less-conserved regions than so far identified capsid binders. Therefore, they could be more suitable for the development of new inhibitors.

## Main

Rhinoviruses are the most common respiratory pathogens<sup>1</sup> including species A, B, and C within the genus *ENTEROVIRUS*, family *picornaviridae*<sup>2,3</sup>. RVs mainly cause the common cold and are adapted to optimally grow at 33 – 34 °C, the mean temperature of the upper respiratory tract<sup>4</sup>. However, some RVs can also efficiently replicate at 37 °C and cause pulmonary infections<sup>5</sup>.

Biology and pathogenesis of RVs is an active field of research due to their high medical and economic impact and lack of vaccines and efficient medication<sup>6,7</sup>. RVs are icosahedrons, with a protein shell of about 30 nm in diameter containing a ss(+)RNA genome of about 7,200 bases. The capsid is composed of 60 copies each of four proteins, VP1, VP2, VP3, and VP4 arranged in a pseudo T=3 lattice<sup>8</sup>; VP4 is ~ 7kD and located at the inner side, close to the RNA. VP1, VP2, and VP3 (~ 25 kD – 35 kD) at the capsid surface contain variable surface loops recognized by serotype-specific neutralizing antibodies; their barrels are each built from seven antiparallel sheets with sequence similarity. VP1, VP2, and VP3 interact with cell surface molecules (receptors) for viral attachment. Most RV-A and all RV-B exploit the intercellular adhesion molecule-1 (ICAM-1) as receptor<sup>9</sup>, twelve RV-A at least two members of the low-density lipoprotein receptor (LDLR) family<sup>10</sup>, and RV-C use the cadherin-related family member 3 (CDHR3)<sup>11</sup>. Whereas ICAM-1 binds into the canyon, a deep cleft encircling the star-shaped dome at the five-fold axes of symmetry<sup>12</sup>, members of the LDLR family rather bind to the dome itself, closer to the symmetry axis<sup>13</sup>. The binding site of CDHR3 on RV-C has not yet been disclosed.

Among the most conserved regions in the structural and non-structural proteins are a hydrophobic pocket in the capsid of RV-A and RV-B (RV-C lack a similar pocket<sup>14</sup>) and the active sites of the viral enzymes. Therefore, these regions are obvious targets of inhibitors acting against a broad spectrum of RVs. However, due to insufficient efficacy, mutational escape, and/or side effects observed in clinical studies, none of these antivirals has been approved<sup>15-17</sup>. Recently, it was discovered that the small cellular phospholipase pla2g16, aids the transfer of the viral RNA genome into the cytosol<sup>18,19</sup>. It may be a potential host target for the treatment of RVs and EVs.

Nevertheless, a full understanding of its function in the uninfected cell will be necessary before inhibitors can be brought to the clinic.

Severe disease outbreaks caused by RV-related enteroviruses<sup>20</sup> re-stimulated the search for inhibitors<sup>21</sup>. Despite the ongoing quest for compounds targeting non-structural viral proteins and cellular factors, capsid-binders like pleconaril (Fig. S1) and vapedavir<sup>22</sup> have remained in the focus. Capsid-binders belong to a class of inhibitors binding into the hydrophobic pocket lined by amino acid residues from VP1, with some contribution of VP2 and VP3<sup>23</sup>. Most of the residues are highly conserved within the genus *ENTEROVIRUS*<sup>23,24</sup> enabling the inhibition of a broad-spectrum of RVs and EVs with capsid binders<sup>25</sup>. Capsid-binders can exert virucidal activity against RVs and EVs<sup>24,26</sup>, impede viral adsorption via modifying the conformation of the receptor binding site<sup>24,27,28</sup> and/or prevent structural changes required for RNA uncoating<sup>29</sup>. As shown exemplarily for pleconaril, occupancy of the hydrophobic pocket can be higher when the capsid-binder is introduced during viral assembly<sup>25</sup>.

Naturally occurring as well as experimentally selected resistance of RVs and EVs to capsid-binders is mainly based on a polymorphism of amino acid residues in the center of the hydrophobic binding pocket<sup>23,28,30-33</sup>. For example, in the pleconaril-resistant RV-B4, -B5, -B42, -B84, -B93, -B97 and -B99 [30] the amino acid residues F1152 and L1191 (first digit refers to the VP, i.e. “1” denotes VP1) were detected. In pleconaril-susceptible serotypes their respective positions are occupied by Y1152 and V/I/T1191<sup>34</sup>. It has been shown that the amino acid substitutions Y1152F and V1191L in VP1 of the naturally pleconaril-susceptible RV-B14 confer full resistance to pleconaril<sup>34</sup>. Three-dimensional structures of the pleconaril-susceptible RV-B14<sup>8</sup> and RV-A16<sup>25</sup> have been determined to atomic resolution by X-ray crystallography. The results suggest that the bulkier L1191 narrows the drug-binding pocket and sterically hinders pleconaril binding, in particular by interfering with its central ring<sup>34</sup>. A similar resistance mechanism was proposed for vapedavir and EV-68 and EV-71<sup>22,35</sup>. Accordingly, chemical modifications of the central ring of pleconaril led to a regain of its anti-enteroviral activity<sup>36</sup>. In addition, full pleconaril resistance was detected in coxsackievirus B3 (CVB3), another EV, following the substitutions I1207R/K near to the hydrophobic binding pocket<sup>37</sup>. As atomic structures of pleconaril-resistant RVs are lacking, the

differences in the capsid structure of pleconaril-susceptible and -resistant RVs remain to be determined.

Pyrazolopyrimidines are relatively new capsid-binding inhibitors with particularly strong activity against pleconaril-resistant EVs and RVs<sup>24</sup>. Like pleconaril and varendavir, they are three-ring compounds. The structural similarity and inhibition profile, together with results of computational modelling of CVB3 in complex with OBR-5-340 (Fig. S1), taken as an example, suggested that pyrazolopyrimidines would also bind to the hydrophobic pocket [24]. However, the differences in the spectrum of pleconaril- and OBR-5-340-susceptible RVs imply differences in the binding.

Here, we aimed to decipher the mechanism of inhibition of full pleconaril-resistant RVs<sup>30</sup> by pyrazolopyrimidines as well as the atomic structure of a RV-pyrazolopyrimidine complex. These studies were performed with the pleconaril-resistant RV-B5 and OBR-5-340, the most promising, orally bioavailable pyrazolopyrimidine. For comparison, the pleconaril-sensitive RV-A2 and RV-A89 and pleconaril were included in some of the experiments. The anti-RV-B5 activity of OBR-5-340 under single growth cycle conditions was confirmed. Steps of the replication cycle inhibited by OBR-5-340 were identified. Uncoating inhibition was confirmed by stabilization of RV-B5 by OBR-5-340 against temperature-dependent conversion into the permeable subviral A-particle, an uncoating intermediate. Since RV-B5 was found to grow poorly in spinner cultures, as employed for mass production of numerous other serotypes<sup>38</sup>, we solved the 3D-structure to 3.6 Å with the available small amounts of RV-B5 complexed to OBR-5-340 by using cryogenic electron microscopy (cryo-EM). For comparison, 3D-structures of RV-B5 (in the absence of OBR-5-340) and of naturally drug-resistant RV-A89 (in the presence of OBR-5-340) were determined at 3.2 and 2.9 Å, respectively. Unexpectedly, OBR-5-340 was found to bind closer to the entrance of the pocket than most capsid-binders studied so far, with only partial overlap of their binding sites. This suggests that suitable combinations of antivirals might alleviate resistance and allow to more efficiently fighting the common cold.

## Results

### Effect of OBR-5-340 on single-step growth of RV-B5.

Because RV-B5 is highly susceptible to OBR-5-340 in cytopathic effect (CPE) inhibition assays (50% inhibitory concentration,  $IC_{50}=0.08 \mu\text{M}$ ; compound 36 in the Supporting Information of ref. <sup>24</sup>) and fully resistant to pleconaril ( $IC_{50}>12.5 \mu\text{M}$ ; higher concentrations were cytotoxic) <sup>24,30</sup>, we selected it for the present study. Single-step growth curves with RV-B5 were recorded in the absence and presence of the highly-effective OBR-5-340 concentration of  $1 \mu\text{M}$  in HeLa cells. The time-dependent increase in infectious units (measured in a separate assay as 50% tissue culture infectious dose;  $TCID_{50}$ ) in the presence of OBR-5-340 was marginal whereas in the control without OBR-5-340 the virus titer increased by about 2.5 log units within 10 h, the time needed to complete a single growth cycle. The reduction in virus titer was thus about 1.5 log units (Fig. 1A).

### Mechanism of viral inhibition

We investigated which stage of the infection cycle was most affected by OBR-5-340 by using a previously established plaque-reduction assay<sup>24</sup>. OBR-5-340 ( $0.5 \mu\text{M}$ ) was added at different times before and after challenge of HeLa cells with RV-B5. As seen from the percent reduction in plaque numbers depicted in Fig. 1B, incubation of HeLa cells with OBR-5-340 before viral challenge (Fig. 1B,a), of RV-B5 prior challenge of HeLa cells (Fig. 1B,b), and during RV-B5 penetration (Fig. 1B,d), was ineffective. Formation of RV-B5-induced plaques was reduced by 40 - 50% when OBR-5-340 treatment was performed only during RV-B5 adsorption (2 h at  $4^{\circ}\text{C}$ ; Fig. 1B, c), during uncoating (2 h at  $33^{\circ}\text{C}$  after RV-B5 adsorption and penetration Fig. 1B, e), and during early replication (6 h at  $33^{\circ}\text{C}$  after RV-B5 adsorption and penetration; Fig. 1B, f). The strongest reduction of plaque formation was detected when OBR-5-340 was present for 72 h in the agar overlay and could act during multiple rounds of RV-replication. This is shown in Fig. 1B, g and h, where OBR-5-340 was added immediately after RV-B5 adsorption and kept till the end of the experiment or was present throughout the entire experiment, respectively.

**OBR-5-340 stabilizes RV-B5 against heat-triggered RNA exposure but RV-A2 and RV-A89 are unaffected.**

Several capsid-binders have been shown to stabilize the virion against the conformational associated with uncoating of the genomic RNA<sup>27,28,39-31</sup>. Conversion of the native virion into the expanded A-particle with holes for RNA exit is facilitated by expulsion of the natural pocket factor, probably a fatty acid<sup>42</sup>. Capsid binders stabilize the virion against the conversion into the permeable A-particle and thus block release of the RNA [43]. Heating to  $\geq 50$  °C also triggers this conversion and/or the release of the RNA, depending on the buffer composition<sup>44,45</sup>. This process is inhibited by capsid binders.

Results from time-of-addition and plaque-reduction assays showed inhibition of RV-B5 uncoating (Fig. 1, e). To further confirm this, RV-B5 was pre-incubated for 1 h at 37 °C with 1 mM of the respective inhibitor to allow for saturation of binding sites and displacement of natural factors that might reside in the pocket. Then, Syto-82, a dye becoming fluorescent upon binding to RNA, was added and the temperature was increased<sup>46</sup>. Syto-82 cannot penetrate into the native virion. However, upon conversion into subviral particles, the RNA is accessible for the dye – either through the holes in the shell - or upon its release into solution; both result in fluorescence. As seen in Fig. 2A, a fluorescence peak appeared at 51 °C when virus was heated in the absence of OBR-5-340. In its presence, this peak was shifted towards 55.5 °C. Decline of the signal upon further rise of the temperature is probably due to RNA unfolding. When the RNA had been released prior to the experiment, fluorescence at the start of temperature ramping was similar to the maximum attained with virus at around 51 °C and similarly diminished upon further temperature increase. Using bovine serum albumin as a control, no peaks were observed, excluding interaction between the dye and OBR-5-340 and/or the solvent DMSO (Fig. S2).

For better identification of the temperature of fluorescence onset, we plotted the 1<sup>st</sup> derivative against the temperature (Fig. 2, right panels). Accordingly, viral conversion was initiated at 48 °C in the absence of OBR-5-340 and at 53 °C in **its** presence (Fig. 2B). It is thus obvious that OBR-5-340 stabilizes RV-B5 against conversion into (permeable) subviral particles. As control,

we also studied the effect of pleconaril (Fig. 2, panels C, D). In agreement with RV-B5 being resistant against pleconaril<sup>34</sup>, no shift of the fluorescence signal towards higher temperature was observed. As additional controls we used the pleconaril-sensitive RV-A2 and RV-A89<sup>30,47</sup>. Several compounds have been shown to inhibit RV-A2 conversion into the A-particle/empty capsid by heat or low pH using other means of detection<sup>40,43</sup>. Fig. 2 (panels E, F) show that heat-triggered uncoating of RV-A2 is not affected by OBR-5-340 ( $IC_{50}=13.77 \mu\text{M}$ ; compound 36, Supporting Information<sup>24</sup>, as compared to  $IC_{50} \sim 0.08 \mu\text{M}$  for RV-B5). However, as expected<sup>48</sup>, RV-A2 was stabilized by pleconaril (panels Fig. 2, panels G, H). Additionally, we studied the pleconaril-sensitive RV-A89<sup>47</sup>. As seen in Fig. 2, panels I and J, OBR-5-340 also had no impact on its temperature sensitivity, which is consistent with its natural resistance against this compound, as was also confirmed in our CPE inhibition assays; no inhibitory activity of OBR-5-340 at  $100 \mu\text{M}$  was recorded for RV-A89. Conversely, RV-A89 was inhibited by pleconaril with  $IC_{50} 0.02 \pm 0.01 \mu\text{M}$  in the CPE inhibitory assay. Of note, OBR-5-340 stabilized RV-B5 somewhat at  $1 \mu\text{M}$  and strongly at  $10 \mu\text{M}$  and  $100 \mu\text{M}$ .

### Cryo-EM 3D-structures of RV-B5 and RV-A89

Poor growth of RV-B5 in suspension culture did not yield a quantity necessary for crystallization trials as required for X-ray analysis<sup>49</sup>. We thus collected cryo-EM data of the available small amounts of virus incubated with  $1 \text{ mM}$  OBR-5-340, the highest concentration achievable without exceeding 10% DMSO used as solvent. For direct comparability, incubation conditions were kept identical with those of the stabilization assays above, except that the virus concentration that was  $0.6 \text{ mg/ml}$ . Imposing icosahedral symmetry, we determined the 3D-structure of RV-B5 to  $3.6 \text{ \AA}$  based upon the FSC resolution criteria  $0.143$  (Fig. 3A, Table S1, Fig. S4, left panel). The quality of the maps was high (Fig. 3B, left). Residues included in the atomic model were for VP1 **Q1016-Y1288** (not visible: G1001-Q1015); VP2 **G2008-I2259** (not visible: S2001-C2007 and Q2230); VP3 **G3001-Q3231** (not visible: T3232); and VP4 **I4030-N4069** (not visible G1001-V4029 and S4070). Additional density not attributable to amino acid residues was identified in the hydrophobic pocket (Fig. 3C); this density accommodates OBR-5-340 well. In the

absence of OBR-5-340, RV-B5 shows very weak density of dissimilar shape in the deeper binding position (Fig. 3D, Table S1, Fig. S4). It might stem from a natural pocket factor being present at low occupancy. The pocket of the OBR-5-340 resistant RV-A89 identically incubated with OBR-5-340 and analyzed as an additional negative control (Fig. S4, Fig. S5, Table S1) was empty.

Strikingly, OBR-5-340 was observed to bind closer to the entrance of the hydrophobic pocket than most capsid-binders including pleconaril (Fig. 4 and Table S2). Only for the structure of CoxA9 modeled with two disoxaril (WIN51711) molecules, weak density has been reported at the entrance or ‘mouth’ of the hydrophobic pocket that could potentially stem from a synthetic compound. One bound in the deep parts of the hydrophobic pocket ( $\beta$ -barrel region) and one bound at the ‘mouth’ of the hydrophobic pocket (<sup>50</sup>; PDB 1D4M). Few structures of *ENTEROVIRUS* capsids have been deposited in the PDB where pocket factors protrude to the entry/mouth area of the binding site. The best examples are PDB 1MQT, where C8 ceramide is located mainly in the  $\beta$ -barrel region but elongates into the entry area, and PDB 1AYM, where lauric acid is straddled between the two regions. The small molecules observed or postulated to bind to the mouth of the hydrophobic pocket exhibit enormous conformational flexibility that is based on their long, aliphatic moieties. This makes their binding entropically unfavorable. In contrast, OBR-5-340 is a rigid molecule with few rotatable bonds. Therefore, it is expected to be less affected by loss of entropy upon binding and to be a more suitable template for the development of new drugs.

OBR-5-340 forms a tight network of interactions with the VPs. Its pyrazolopyrimidine core forms two hydrogen bonds with N1198; one with the amide NH and one with the amide carbonyl oxygen. The trifluorophenyl moiety forms an H-bond with Y1128. The ligand core and the trifluorophenyl moiety are engaged in pi-stacking interactions with Y1197. OBR-5-340 also forms hydrophobic interactions with I1104, L1106, I1193, A1194, and L1218.

In the absence of OBR-5-340, RV-B5 shows very weak density of dissimilar shape in the deeper binding position (Fig. 3D, Table S1, Fig. S5). It might originate from a natural pocket factor, presumably myristate, being present at low occupancy. The pocket of the OBR-5-340 resistant RV-

A89 identically incubated with OBR-5-340 and analyzed as additional negative control (Fig. S4, Table S1, Fig. S5, right panels) was empty.

## Discussion

We demonstrate that infection of HeLa cells by RV-B5, a naturally pleconaril-resistant rhinovirus, is strongly inhibited by OBR-5-340. This compound represents a novel class of pyrazolopyrimidines active against various picornaviruses of the genus *ENTEROVIRUS*<sup>24</sup>. In addition to RV-B5, OBR-5-340 also strongly inhibits other pleconaril-resistant RVs at low  $\mu\text{M}$  concentrations<sup>24</sup>. Whether the compound is similarly active against the remaining pleconaril-resistant RV-B4, -B84, -B93, -B97, and -B99<sup>34</sup> remains to be determined.

OBR-5-340 treatment for 2 h at 4°C inhibited RV-B5 adsorption to HeLa by 40 %. This agrees with the inhibition of RV-B14 adsorption by 8 other capsid-binders<sup>27</sup>. However, the strongest plaque reduction was observed when OBR-5-340 was present for 72 h (overall incubation time for the plaque assay), i.e. during multiple rounds of replication. In each round, inhibition of RV-B5 adsorption and uncoating can occur. Furthermore, it is possible that OBR-5-340, similar to pleconaril<sup>25</sup>, incorporates better into progeny viruses during assembly thereby increasing the antiviral effect. Zhang et al. observed lower incorporation of pleconaril into RV-B14 and RV-A16 crystals upon soaking, then when pleconaril was present during viral assembly<sup>25</sup>. The authors concluded that pleconaril acts more strongly on the infectivity of RV-A16 progeny virions than on the parent input virus. This was not studied here but might help to further explain our data.

The moderate inhibition of RV-B5 uncoating is in line with the low but detectable *in vitro* stabilization of RV-B5 by 1  $\mu\text{M}$  OBR-5-340 (Fig. S3). The binding site of OBR-5-340 overlaps only marginally with other capsid-binders as it localizes more closely to the entryway of the binding pocket (Fig. 4). Similar to other capsid-binding compounds, OBR-5-340 prevents conformational changes of the native virion that are essential for RNA release. Incubation of RV-B5 with OBR-5-340 at concentrations between 1  $\mu\text{M}$  and 1 mM stabilized the virion against heat-triggered exposure

of the RNA as indicated by *in vitro* uncoating occurring at up to 5 °C higher temperature as compared to virus without OBR-5-340 (Fig. 2A, Fig. S3). During viral replication OBR-5-340 might become incorporated into the capsid rendering progeny virus non-infectious and thus unable to spread.

Of note, the conformation of the pocket was virtually identical, regardless of the presence or absence of OBR-5-340 in RV-B5 (Fig. 3C, D). Hence, filling the pocket does not seem to result in major structural rearrangements as were observed upon binding of WIN 52035-2 to RV-B14<sup>28</sup>. Indeed, the pocket of RV-B5 is somewhat more open when compared to the one of RV-A89 (Fig. S3D); several residues in close proximity of OBR-5-340 in the complex with RV-B5 are different in RV-A89 (Fig. S6, Table S3). This might explain why OBR-5-340 is unable to bind to RV-A89, even at a concentration as high as 1 mM.

OBR-5-340 is the first drug-like compound with a rigid molecular scaffold that binds to the entrance of the hydrophobic pocket. This adds a new dimension to the quest for capsid-binding drugs and suggests that selected drug combinations might become useful in combating RV infections.

## **Materials and Methods**

### **Cells and viruses**

HeLa Ohio cells were used throughout. Virus stocks were grown from seed obtained from ATCC. Viral identity was verified via partial RNA and MSMS protein sequencing as well as by neutralization with ATCC type-specific antisera.

### **Effect of OBR-5-340 on single-step growth of RV-B5 in HeLa cells**

The time-dependent production of viral progeny without (control) and with addition of 1  $\mu$ M OBR-5-340 was recorded. At specified times, infected cells were subjected to three rounds of freeze-thawing to release intracellular virus and the titer was determined as TCID<sub>50</sub>.

### **Mechanism of action studies with RV-B5 and OBR-5-340 using a modified plaque reduction assay**

Cells or virus were preincubated with OBR-5-340 or OBR-5-340 was added and kept present for the different time periods as indicated and described previously for CVB3<sup>24</sup>. Three days p.i. cells were fixed and stained with a crystal violet-formalin solution and plaques were counted.

### **Temperature-dependent *in vitro* uncoating of native virus and its inhibition by drugs**

Temperature-stability assays were carried out similarly as for foot-and-mouth-disease-virus<sup>46</sup>. Virus +/- inhibitor was heated in the presence of Syto-82. The onset of fluorescence was taken as the temperature at which the virus was converted into the permeable A and/or B-particle with the RNA becoming accessible for the dye.

### **Cryo-EM analysis of RV-B5 OBR-5-340 complexes and of RV-A89 in presence of OBR-5-340**

The respective virus was either incubated with OBR-5-340 or with solvent, applied onto carbon-coated grids and flash-frozen with a Vitrobot. Movies were collected, submitted to drift-correction and the 3D-structure was determined with routine procedures by using Relion-3<sup>51</sup>. Fitting the coordinates was carried out with Phenix<sup>52</sup> and Coot<sup>53</sup>. The models were visualized with Chimera<sup>54</sup>.

### **Comparison of *ENTEROVIRUS*-ligand complexes in the PDB database with OBR-5-340 complexed to RV-B5**

The PDB (<https://www.rcsb.org> - accessed on February 22nd, 2019) was queried for any structures of enteroviral proteins using the Source Organism Browser. This resulted in 82 structures that we aligned with Maestro (release 2018-3, Schrödinger, LLC, New York, NY, 2019).

## References

1. Jacobs SE, Lamson DM, St George K, Walsh TJ. Human rhinoviruses. *Clin Microbiol Rev.* 2013;26(1):135-62. Epub 2013/01/09. doi: 10.1128/CMR.00077-12. PubMed PMID: 23297263; PubMed Central PMCID: PMC3553670.
2. Palmenberg AC, Spiro D, Kuzmickas R, Wang S, Djikeng A, Rathe JA, Fraser-Liggett CM, Liggett SB. Sequencing and analyses of all known human rhinovirus genomes reveal structure and evolution. *Science.* 2009;324(5923):55-9. Epub 2009/02/14. doi: 10.1126/science.1165557. PubMed PMID: 19213880; PubMed Central PMCID: PMC3923423.
3. Royston L, Tapparel C. Rhinoviruses and Respiratory Enteroviruses: Not as Simple as ABC. *Viruses.* 2016;8(1). Epub 2016/01/14. doi: 10.3390/v8010016. PubMed PMID: 26761027; PubMed Central PMCID: PMC4728576.
4. Tyrrell DA, Parsons R. Some virus isolations from common colds. III. Cytopathic effects in tissue cultures. *Lancet.* 1960;1(7118):239-42. Epub 1960/01/30. PubMed PMID: 13840115.
5. Papadopoulos NG, Sanderson G, Hunter J, Johnston SL. Rhinoviruses replicate effectively at lower airway temperatures. *J Med Virol.* 1999;58(1):100-4. Epub 1999/05/01. PubMed PMID: 10223554.
6. Papadopoulos NG, Megremis S, Kitsioulis NA, Vangelatou O, West P, Xepapadaki P. Promising approaches for the treatment and prevention of viral respiratory illnesses. *J Allergy Clin Immunol.* 2017;140(4):921-32. Epub 2017/07/26. doi: 10.1016/j.jaci.2017.07.001. PubMed PMID: 28739285.
7. Rollinger JM, Schmidtke M. The human rhinovirus: human-pathological impact, mechanisms of antirhinoviral agents, and strategies for their discovery. *Med Res Rev.* 2011;31(1):42-92. Epub 2009/08/29. doi: 10.1002/med.20176. PubMed PMID: 19714577.
8. Rossmann MG, Arnold E, Erickson JW, Frankenberger EA, Griffith JP, Hecht HJ, Johnson JE, Kamer G, Luo M, Mosser AG, et al. Structure of a human common cold virus and functional relationship to other picornaviruses. *Nature.* 1985;317(6033):145-53. Epub 1985/09/12. PubMed PMID: 2993920.

9. Greve JM, Davis G, Meyer AM, Forte CP, Yost SC, Marlor CW, Kamarck ME, McClelland A. The major human rhinovirus receptor is ICAM-1. *Cell*. 1989;56(5):839-47. Epub 1989/03/10. PubMed PMID: 2538243.
10. Hofer F, Gruenberger M, Kowalski H, Machat H, Huettinger M, Kuechler E, Blaas D. Members of the low density lipoprotein receptor family mediate cell entry of a minor-group common cold virus. *Proc Natl Acad Sci USA*. 1994;91(5):1839-42. Epub 1994/03/01. doi: 10.1073/pnas.91.5.1839. PubMed PMID: 8127891; PubMed Central PMCID: PMC43259.
11. Bochkov YA, Watters K, Ashraf S, Griggs TF, Devries MK, Jackson DJ, Palmenberg AC, Gern JE. Cadherin-related family member 3, a childhood asthma susceptibility gene product, mediates rhinovirus C binding and replication. *Proc Natl Acad Sci U S A*. 2015;112(17):5485-90. Epub 2015/04/08. doi: 10.1073/pnas.1421178112. PubMed PMID: 25848009; PubMed Central PMCID: PMC4418890.
12. Olson NH, Kolatkar PR, Oliveira MA, Cheng RH, Greve JM, McClelland A, Baker TS, Rossmann MG. Structure of a human rhinovirus complexed with its receptor molecule. *Proc Natl Acad Sci USA*. 1993;90(2):507-11. Epub 1993/01/15. doi: 10.1073/pnas.90.2.507. PubMed PMID: 8093643; PubMed Central PMCID: PMC45692.
13. Verdaguer N, Fita I, Reithmayer M, Moser R, Blaas D. X-ray structure of a minor group human rhinovirus bound to a fragment of its cellular receptor protein. *Nat Struct Mol Biol*. 2004;11(5):429-34. Epub 2004/04/06. doi: 10.1038/nsmb753. PubMed PMID: 15064754.
14. Liu Y, Hill MG, Klose T, Chen Z, Watters K, Bochkov YA, Jiang W, Palmenberg AC, Rossmann MG. Atomic structure of a rhinovirus C, a virus species linked to severe childhood asthma. *Proc Natl Acad Sci U S A*. 2016;113(32):8997-9002. Epub 2016/08/12. doi: 10.1073/pnas.1606595113. PubMed PMID: 27511920; PubMed Central PMCID: PMC4987780.
15. Bauer L, Lyoo H, van der Schaar HM, Strating JR, van Kuppeveld FJ. Direct-acting antivirals and host-targeting strategies to combat enterovirus infections. *Curr Opin Virol*. 2017;24:1-8. Epub 2017/04/16. doi: 10.1016/j.coviro.2017.03.009. PubMed PMID: 28411509.

16. Senior K. FDA panel rejects common cold treatment. *Lancet Infect Dis.* 2002;2(5):264. Epub 2002/06/14. PubMed PMID: 12062983.
17. Ulferts R, de Boer SM, van der Linden L, Bauer L, Lyoo HR, Mate MJ, Lichiere J, Canard B, Lelieveld D, Omta W, Egan D, Coutard B, van Kuppeveld FJ. Screening of a Library of FDA-Approved Drugs Identifies Several Enterovirus Replication Inhibitors That Target Viral Protein 2C. *Antimicrob Agents Chemother.* 2016;60(5):2627-38. Epub 2016/02/10. doi: 10.1128/AAC.02182-15. PubMed PMID: 26856848; PubMed Central PMCID: PMC4862474.
18. Elling U, Wimmer RA, Leibbrandt A, Burkard T, Michlits G, Leopoldi A, Micheler T, Abdeen D, Zhuk S, Aspalter IM, Handl C, Liebergesell J, Hubmann M, Husa AM, Kinzer M, Schuller N, Wetzel E, van de Loo N, Martinez JAZ, Estoppey D, Riedl R, Yang F, Fu B, Dechat T, Ivics Z, Agu CA, Bell O, Blaas D, Gerhardt H, Hoepfner D, Stark A, Penninger JM. A reversible haploid mouse embryonic stem cell biobank resource for functional genomics. *Nature.* 2017;550(7674):114-8. Epub 2017/09/28. doi: 10.1038/nature24027. PubMed PMID: 28953874; PubMed Central PMCID: PMC6235111.
19. Staring J, von Castelmur E, Blomen VA, van den Hengel LG, Brockmann M, Baggen J, Thibaut HJ, Nieuwenhuis J, Janssen H, van Kuppeveld FJ, Perrakis A, Carette JE, Brummelkamp TR. PLA2G16 represents a switch between entry and clearance of Picornaviridae. *Nature.* 2017;541(7637):412-6. Epub 2017/01/13. doi: 10.1038/nature21032. PubMed PMID: 28077878.
20. Willyard C. An unknown enemy: Drugs sought against EV-68 as paralysis link is explored. *Nat Med.* 2015;21(5):419-21. Epub 2015/03/31. doi: 10.1038/nm.3846. PubMed PMID: 25822590.
21. van der Linden L, Wolthers KC, van Kuppeveld FJ. Replication and Inhibitors of Enteroviruses and Parechoviruses. *Viruses.* 2015;7(8):4529-62. Epub 2015/08/13. doi: 10.3390/v7082832. PubMed PMID: 26266417; PubMed Central PMCID: PMC4576193.
22. Tijisma A, Franco D, Tucker S, Hilgenfeld R, Froeyen M, Leyssen P, Neyts J. The capsid binder Vapendavir and the novel protease inhibitor SG85 inhibit enterovirus 71 replication.

- Antimicrob Agents Chemother.* 2014;58(11):6990-2. Epub 2014/09/10. doi: 10.1128/AAC.03328-14. PubMed PMID: 25199773; PubMed Central PMCID: PMC4249361.
23. Badger J, Minor I, Kremer MJ, Oliveira MA, Smith TJ, Griffith JP, Guerin DM, Krishnaswamy S, Luo M, Rossmann MG, et al. Structural analysis of a series of antiviral agents complexed with human rhinovirus 14. *Proc Natl Acad Sci U S A.* 1988;85(10):3304-8. Epub 1988/05/01. PubMed PMID: 2835768; PubMed Central PMCID: PMC280197.
  24. Makarov VA, Braun H, Richter M, Riabova OB, Kirchmair J, Kazakova ES, Seidel N, Wutzler P, Schmidtke M. Pyrazolopyrimidines: Potent Inhibitors Targeting the Capsid of Rhino- and Enteroviruses. *ChemMedChem.* 2015;10(10):1629-34. Epub 2015/08/12. doi: 10.1002/cmdc.201500304. PubMed PMID: 26260222; PubMed Central PMCID: PMC4600222.
  25. Zhang Y, Simpson AA, Ledford RM, Bator CM, Chakravarty S, Skochko GA, Demenczuk TM, Watanyar A, Pevear DC, Rossmann MG. Structural and virological studies of the stages of virus replication that are affected by antirhinovirus compounds. *J Virol.* 2004;78(20):11061-9. Epub 2004/09/29. doi: 10.1128/JVI.78.20.11061-11069.2004. PubMed PMID: 15452226; PubMed Central PMCID: PMC521849.
  26. Andries K, Dewindt B, Snoeks J, Willebrords R, van Eemeren K, Stokbroekx R, Janssen PA. In vitro activity of pirodavir (R 77975), a substituted phenoxy-pyridazinamine with broad-spectrum antipicornaviral activity. *Antimicrob Agents Chemother.* 1992;36(1):100-7. Epub 1992/01/01. doi: 10.1128/aac.36.1.100. PubMed PMID: 1317142; PubMed Central PMCID: PMC189235.
  27. Pevear DC, Fancher MJ, Felock PJ, Rossmann MG, Miller MS, Diana G, Treasurywala AM, McKinlay MA, Dutko FJ. Conformational change in the floor of the human rhinovirus canyon blocks adsorption to HeLa cell receptors. *J Virol.* 1989;63(5):2002-7. Epub 1989/05/01. PubMed PMID: 2539499; PubMed Central PMCID: PMC250615.
  28. Shepard DA, Heinz BA, Rueckert RR. WIN 52035-2 inhibits both attachment and eclipse of human rhinovirus 14. *J Virol.* 1993;67(4):2245-54. Epub 1993/04/01. PubMed PMID: 8383239; PubMed Central PMCID: PMC240355.

29. Muckelbauer JK, Kremer M, Minor I, Diana G, Dutko FJ, Groarke J, Pevear DC, Rossmann MG. The structure of coxsackievirus B3 at 3.5 Å resolution. *Structure*. 1995;3(7):653-67. Epub 1995/07/15. PubMed PMID: 8591043.
30. Ledford RM, Patel NR, Demenczuk TM, Watanyar A, Herberitz T, Collett MS, Pevear DC. VP1 sequencing of all human rhinovirus serotypes: insights into genus phylogeny and susceptibility to antiviral capsid-binding compounds. *J Virol*. 2004;78(7):3663-74. Epub 2004/03/16. PubMed PMID: 15016887; PubMed Central PMCID: PMCPMC371056.
31. Pevear DC, Hayden FG, Demenczuk TM, Barone LR, McKinlay MA, Collett MS. Relationship of pleconaril susceptibility and clinical outcomes in treatment of common colds caused by rhinoviruses. *Antimicrob Agents Chemother*. 2005;49(11):4492-9. Epub 2005/10/28. doi: 10.1128/AAC.49.11.4492-4499.2005. PubMed PMID: 16251287; PubMed Central PMCID: PMCPMC1280128.
32. Schmidtke M, Hammerschmidt E, Schuler S, Zell R, Birch-Hirschfeld E, Makarov VA, Riabova OB, Wutzler P. Susceptibility of coxsackievirus B3 laboratory strains and clinical isolates to the capsid function inhibitor pleconaril: antiviral studies with virus chimeras demonstrate the crucial role of amino acid 1092 in treatment. *J Antimicrob Chemother*. 2005;56(4):648-56. Epub 2005/09/10. doi: 10.1093/jac/dki263. PubMed PMID: 16150864.
33. Heinz BA, Rueckert RR, Shepard DA, Dutko FJ, McKinlay MA, Fancher M, Rossmann MG, Badger J, Smith TJ. Genetic and molecular analyses of spontaneous mutants of human rhinovirus 14 that are resistant to an antiviral compound. *J Virol*. 1989;63(6):2476-85. Epub 1989/06/01. PubMed PMID: 2542566; PubMed Central PMCID: PMCPMC250706.
34. Ledford RM, Collett MS, Pevear DC. Insights into the genetic basis for natural phenotypic resistance of human rhinoviruses to pleconaril. *Antiviral Res*. 2005;68(3):135-8. doi: 10.1016/j.antiviral.2005.08.003. PubMed PMID: 16199099.
35. Sun L, Meijer A, Froeyen M, Zhang L, Thibaut HJ, Baggen J, George S, Vernachio J, van Kuppeveld FJ, Leyssen P, Hilgenfeld R, Neyts J, Delang L. Antiviral Activity of Broad-Spectrum and Enterovirus-Specific Inhibitors against Clinical Isolates of Enterovirus D68. *Antimicrob Agents Chemother*. 2015;59(12):7782-5. Epub 2015/09/16. doi: 10.1128/AAC.01375-15. PubMed PMID: 26369972; PubMed Central PMCID: PMCPMC4649165.

36. Schmidtke M, Wutzler P, Zieger R, Riabova OB, Makarov VA. New pleconaril and [(biphenyloxy)propyl]isoxazole derivatives with substitutions in the central ring exhibit antiviral activity against pleconaril-resistant coxsackievirus B3. *Antiviral Res.* 2009;81(1):56-63. Epub 2008/10/09. doi: 10.1016/j.antiviral.2008.09.002. PubMed PMID: 18840470.
37. Braun H, Kirchmair J, Williamson MJ, Makarov VA, Riabova OB, Glen RC, Sauerbrei A, Schmidtke M. Molecular mechanism of a specific capsid binder resistance caused by mutations outside the binding pocket. *Antiviral Res.* 2015;123:138-45. Epub 2015/09/24. doi: 10.1016/j.antiviral.2015.09.009. PubMed PMID: 26391975.
38. Weiss VU, Subirats X, Kumar M, Harutyunyan S, Gosler I, Kowalski H, Blaas D. Capillary electrophoresis, gas-phase electrophoretic mobility molecular analysis, and electron microscopy: effective tools for quality assessment and basic rhinovirus research. *Methods Mol Biol.* 2015;1221:101-28. Epub 2014/09/28. doi: 10.1007/978-1-4939-1571-2\_9. PubMed PMID: 25261310.
39. Reisdorph N, Thomas JJ, Katpally U, Chase E, Harris K, Siuzdak G, Smith TJ. Human rhinovirus capsid dynamics is controlled by canyon flexibility. *Virology.* 2003;314(1):34-44. PubMed PMID: 14517058.
40. Gruenberger M, Pevear D, Diana GD, Kuechler E, Blaas D. Stabilization of human rhinovirus serotype 2 against pH-induced conformational change by antiviral compounds. *J Gen Virol.* 1991;72 ( Pt 2):431-3. Epub 1991/02/01. doi: 10.1099/0022-1317-72-2-431. PubMed PMID: 1847178.
41. Dewindt B, van Eemeren K, Andries K. Antiviral capsid-binding compounds can inhibit the adsorption of minor receptor rhinoviruses. *Antiviral Res.* 1994;25(1):67-72. PubMed PMID: 7811059.
42. Garriga D, Pickl-Herk A, Luque D, Wruss J, Caston JR, Blaas D, Verdaguer N. Insights into minor group rhinovirus uncoating: the X-ray structure of the HRV2 empty capsid. *PLoS Pathog.* 2012;8(1):e1002473. doi: 10.1371/journal.ppat.1002473. PubMed PMID: 22241997; PubMed Central PMCID: PMC3252380.
43. Okun VM, Nizet S, Blaas D, Kenndler E. Kinetics of thermal denaturation of human rhinoviruses in the presence of anti-viral capsid binders analyzed by capillary

- electrophoresis. *Electrophoresis*. 2002;23(6):896-902. doi: 10.1002/1522-2683(200203)23:6<896::AID-ELPS896>3.0.CO;2-W. PubMed PMID: 11920874.
44. Korant BD, Lonberg-Holm K, Noble J, Stasny JT. Naturally occurring and artificially produced components of three rhinoviruses. *Virology*. 1972;48(1):71-86. PubMed PMID: 4335940.
  45. Lonberg-Holm K, Yin FH. Antigenic determinants of infective and inactivated human rhinovirus type 2. *J Virol*. 1973;12(1):114-23. Epub 1973/07/01. PubMed PMID: 4126195; PubMed Central PMCID: PMCPMC355237.
  46. Kotecha A, Zhang F, Juleff N, Jackson T, Perez E, Stuart D, Fry E, Charleston B, Seago J. Application of the thermofluor PaSTRy technique for improving foot-and-mouth disease virus vaccine formulation. *J Gen Virol*. 2016;97(7):1557-65. Epub 2016/03/24. doi: 10.1099/jgv.0.000462. PubMed PMID: 27002540; PubMed Central PMCID: PMCPMC5042063.
  47. Lacroix C, Laconi S, Angius F, Coluccia A, Silvestri R, Pompei R, Neyts J, Leyssen P. In vitro characterisation of a pleconaril/pirodavir-like compound with potent activity against rhinoviruses. *Virol J*. 2015;12:106. Epub 2015/07/15. doi: 10.1186/s12985-015-0330-4. PubMed PMID: 26169596; PubMed Central PMCID: PMCPMC4501209.
  48. Kaiser L, Crump CE, Hayden FG. In vitro activity of pleconaril and AG7088 against selected serotypes and clinical isolates of human rhinoviruses. *Antiviral Res*. 2000;47(3):215-20. Epub 2000/09/07. PubMed PMID: 10974374.
  49. Verdaguer N, Blaas D, Fita I. Structure of human rhinovirus serotype 2 (HRV2). *J Mol Biol*. 2000;300(5):1179-94. Epub 2000/07/25. doi: 10.1006/jmbi.2000.3943. PubMed PMID: 10903863.
  50. Hendry E, Hatanaka H, Fry E, Smyth M, Tate J, Stanway G, Santi J, Maaronen M, Hyypia T, Stuart D. The crystal structure of coxsackievirus A9: new insights into the uncoating mechanisms of enteroviruses. *Structure*. 1999;7(12):1527-38. Epub 2000/01/27. PubMed PMID: 10647183.
  51. Scheres SH. RELION: implementation of a Bayesian approach to cryo-EM structure determination. *J Struct Biol*. 2012;180(3):519-30. Epub 2012/09/25. doi:

- 10.1016/j.jsb.2012.09.006. PubMed PMID: 23000701; PubMed Central PMCID: PMC3690530.
52. Adams PD, Afonine PV, Bunkoczi G, Chen VB, Davis IW, Echols N, Headd JJ, Hung LW, Kapral GJ, Grosse-Kunstleve RW, McCoy AJ, Moriarty NW, Oeffner R, Read RJ, Richardson DC, Richardson JS, Terwilliger TC, Zwart PH. PHENIX: a comprehensive Python-based system for macromolecular structure solution. *Acta Crystallogr D Biol Crystallogr.* 2010;66(Pt 2):213-21. Epub 2010/02/04. doi: 10.1107/S0907444909052925. PubMed PMID: 20124702; PubMed Central PMCID: PMC2815670.
53. Emsley P, Lohkamp B, Scott WG, Cowtan K. Features and development of Coot. *Acta Crystallogr D Biol Crystallogr.* 2010;66(Pt 4):486-501. Epub 2010/04/13. doi: 10.1107/S0907444910007493. PubMed PMID: 20383002; PubMed Central PMCID: PMC2852313.
54. Pettersen EF, Goddard TD, Huang CC, Couch GS, Greenblatt DM, Meng EC, Ferrin TE. UCSF Chimera--a visualization system for exploratory research and analysis. *J Comput Chem.* 2004;25(13):1605-12. Epub 2004/07/21. doi: 10.1002/jcc.20084. PubMed PMID: 15264254.

**Figure 1**

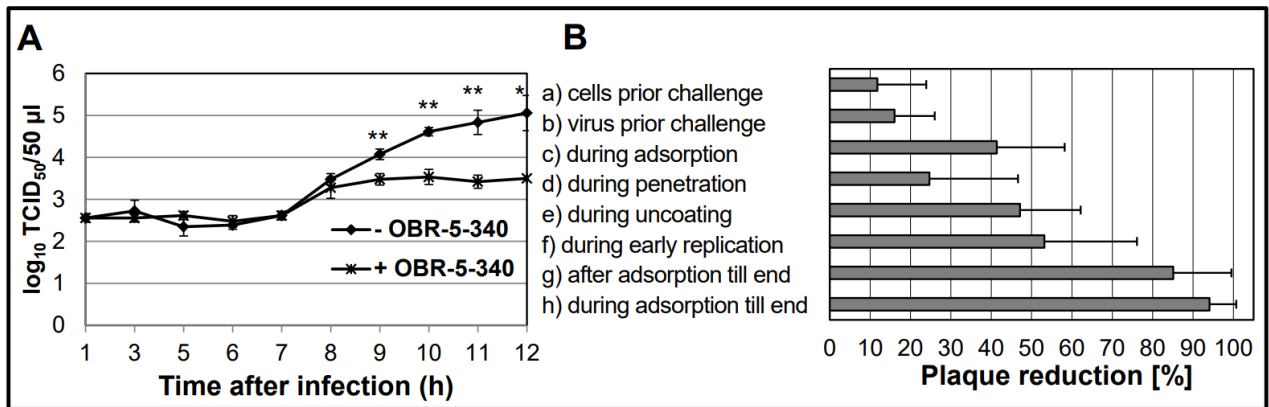


Figure 1: A) OBR-5-340 strongly reduces the yield of RV-B5 in a one cycle infection. HeLa cells were challenged with RV-B5 at multiplicity of infection (MOI=1) ± OBR-5-340 at 1 µM and the virus titer was determined at the times indicated. Mean and standard deviation of three parallel experiments per time point are shown. Significant differences determined with Welch's t-test: \* p<0.05, \*\* p<0.01, and \*\*\* p<0.001. B) Impact of OBR-5-340 on different steps of the replication cycle of RV-B5 determined in a plaque-reduction assay (PRA). RV-B5 was always used at 2×10<sup>5</sup> PFU except for 'pretreatment of virus' (i.e. bar b), in which 5,000 x more PFU were used to account for the dilution required to reduce the inhibitor to a non-active concentration in the subsequent plaque test. The number of plaques recorded in experiments without addition of OBR-5-340, but otherwise conducted identically was set to 100%. The bars indicate percent plaque reduction by OBR-5-340. From top to bottom: a) HeLa cells were pre-incubated with OBR-5-340 for 1 h at 33 °C, washed and RV-B5 was added. b) RV-B5 was incubated with OBR-5-340 for 1 h at 33 °C and subsequently diluted to non-effective inhibitor concentrations (1:5,000). c) RV-B5 was incubated with the cells at 4 °C for 2 h, and non-adsorbed virus was washed away. d) RV-B5 was allowed to attach to the cells as in c) but without inhibitor. OBR-5-340 was then added and the mixture was transferred to the cells. After adsorption for 1 h, the cells were washed and further incubated. e) OBR-5-340 was added immediately after adsorption as in d) and then then kept present till the end

of the experiment. f) OBR-5-340 was added together with the virus and kept present during the whole experiment. g) Cells were challenged with RV-B5 without OBR-5-340 (control). Plaques were allowed to develop under agar and counted after 3 days.

Figure 2

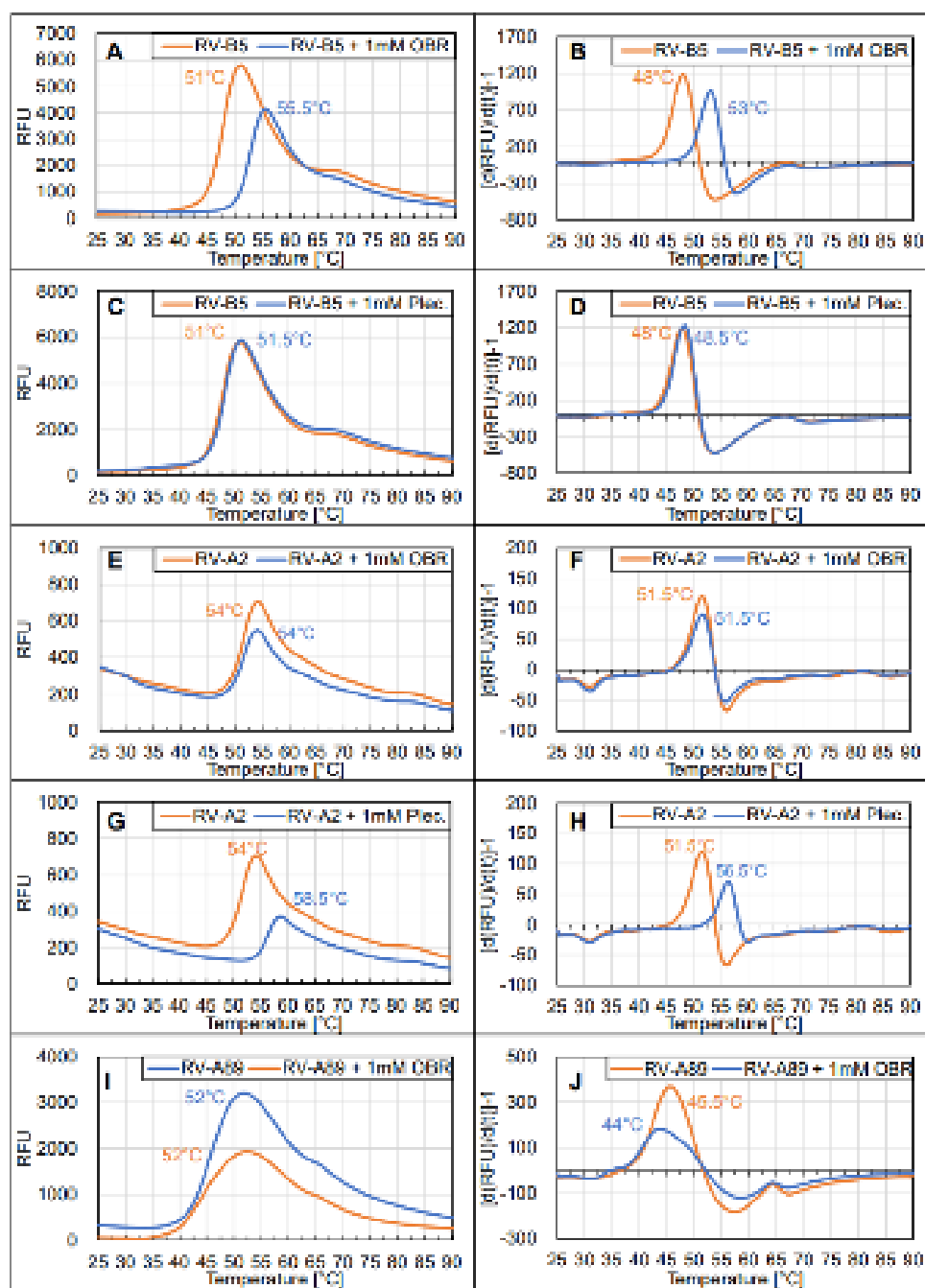


Figure 2: Pleconaril and OBR-5-340 differently stabilize RVs against heat-triggered uncoating. The specified virus types were pre-incubated with or without 1 mM of the indicated inhibitors for 1 h at 37 °C. Syto-82 was then added and the temperature was continuously increased while monitoring fluorescence as detailed in M&M. Left panels show relative fluorescence units measured at the temperatures given at the abscissa. The temperature at which the peak of the respective fluorescence intensity was observed is indicated. The right panels show the corresponding 1<sup>st</sup> derivative. Here, the peaks denote the highest change in fluorescence, which was taken as the onset of RNA accessibility. Note that RV-B5 is stabilized by OBR-5-340 but not by pleconaril and that RV-A2 is stabilized by pleconaril but neither RV-A2 nor RV-A89 is stabilized by OBR-5-340. For lower concentrations of OBR-5-340 inhibiting RV-B5 see Fig. S1. Control experiments with free RNA obtained by prior heating RV-B5 to 60 °C demonstrated a fluorescence plateau that started to decline at about 40 °C presumably because of dissociation of the dye from unfolding RNA (Fig. S2). Note that the two effects occur in parallel with the first one overwhelming the second one.

**Figure 3**

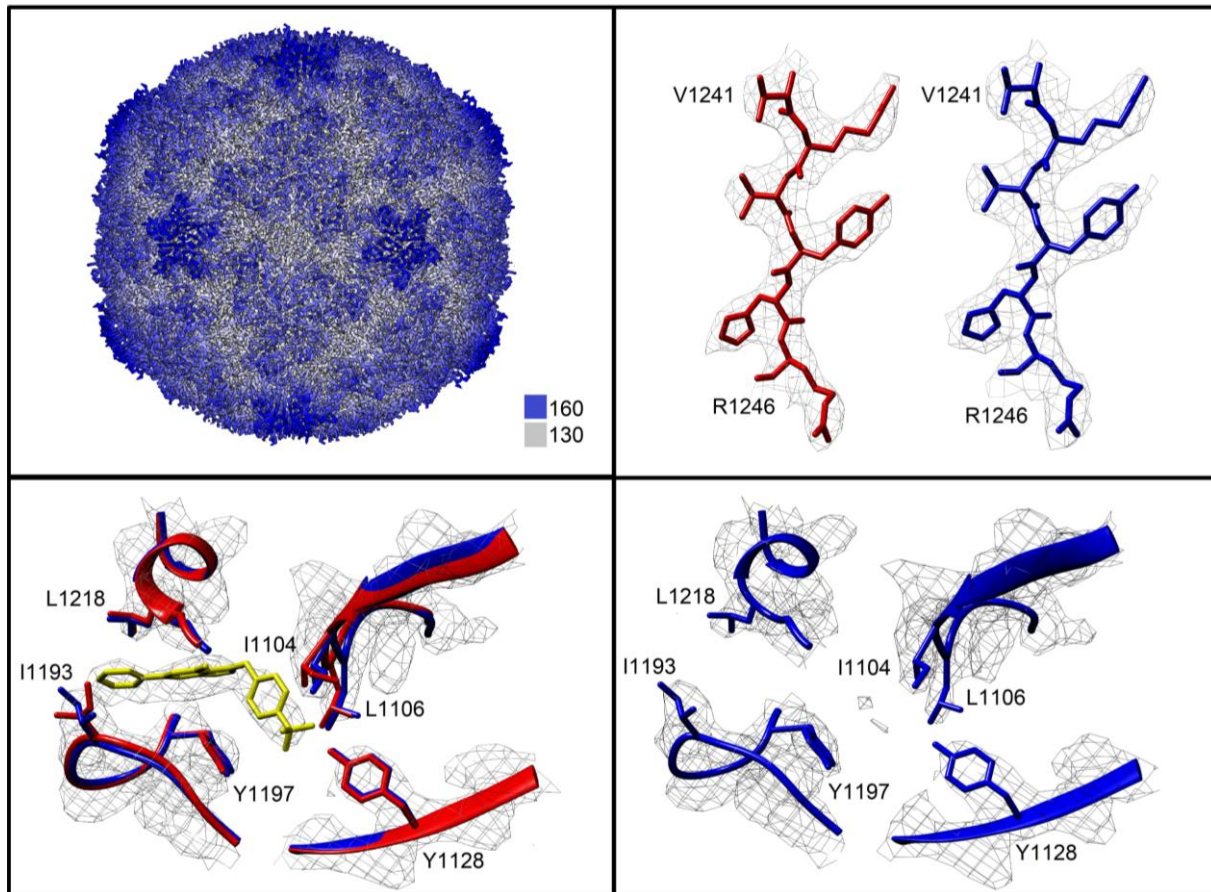


Figure 3: Cryo-EM structure of RV-B5 complexed to OBR-5-340 colored radially as indicated by the color bar. Distance from the viral center is 130 Å (white) to 160 Å (dark blue). B) Example of the quality of the maps of RV-B5 with OBR-5-340 (left) and without (right). C) View centered on OBR-5-340 (yellow) in complex with RV-B5 (red). For comparison, the control, i.e. RV-B5 solved in the absence of inhibitor (blue), is overlaid. Residues nearby and contributed by VP1 are labeled. D) RV-B5 solved in the absence of OBR-5-340. Note the absence of density at the position where the inhibitor is seen in the complex.

**Figure 4**

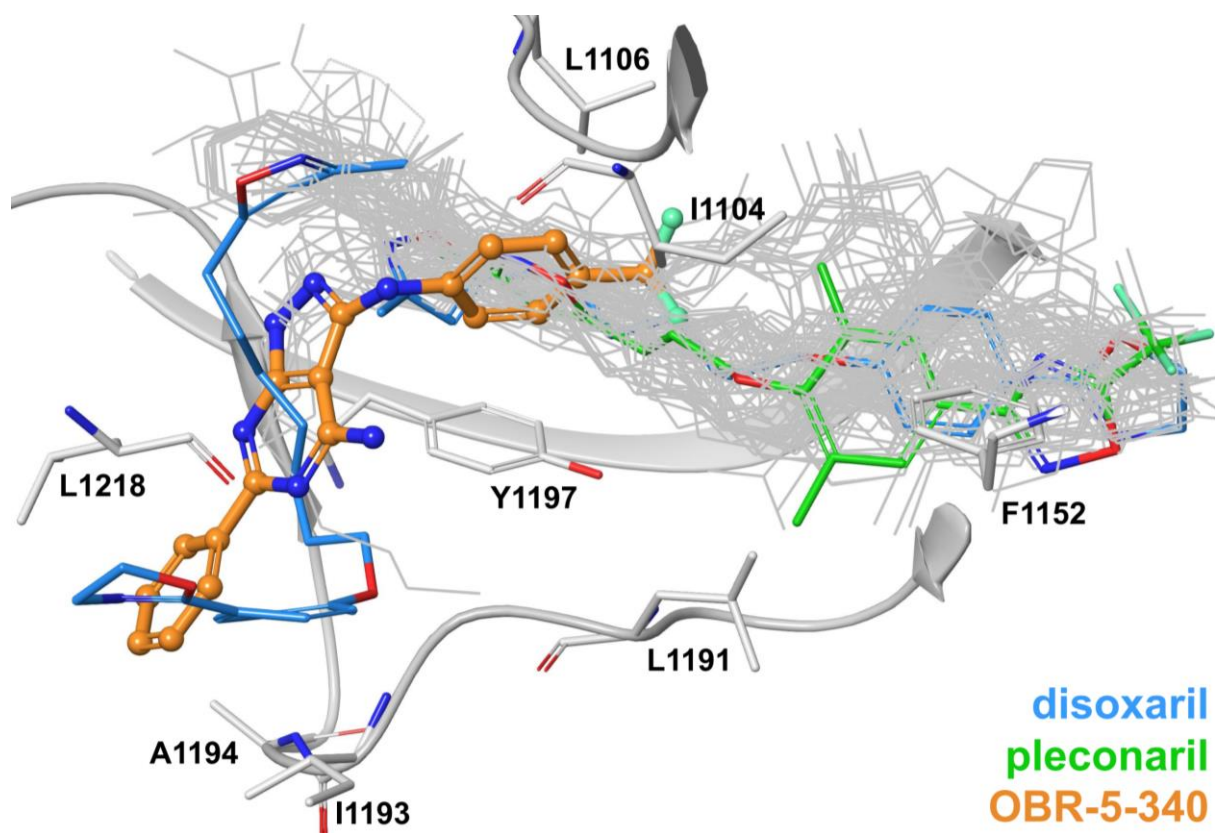


Figure 4: Superposition of 90 crystal structures of capsid binders (most depicted in grey wires) in complex with *ENTEROVIRUS* coat proteins (PDB ids listed in Table S2). OBR-5-340 in complex with RV-B5 is shown in an orange ball-and-stick representation and the two binding poses of WIN51711 from PDB 1D4M are shown in green ball and stick representation. The viral proteins are depicted as ribbons; VP1 (cyan), VP2 (green), VP3 (red), VP4 (yellow).

## Supplementary Information for Chapter 2

### Cryo-EM Structure of Pleconaril-Resistant Rhinovirus-B5 Complexed to the Antiviral OBR-5-340 Reveals Unexpected Binding Site

Jiri Wald<sup>1,\*</sup>, Marion Pasin<sup>2,\*</sup>, Martina Richter<sup>3,\*</sup>, Christin Walther<sup>3,\*</sup>, Neann Mathai<sup>4</sup>, Johannes Kirchmair<sup>4</sup>, Vadim A. Makarov<sup>5</sup>, Nikolaus Gössweiner-Mohr<sup>6</sup>, Thomas C. Marlovits<sup>1</sup>, Irene Zanella<sup>2</sup>, Antonio Real-Hohn<sup>2</sup>, Nuria Verdaguer<sup>7</sup>, Dieter Blaas<sup>2,\*\*</sup>, and Michaela Schmidtke<sup>3,\*\*</sup>

<sup>1</sup>Centre for Structural Systems Biology (CSSB), D-22607, Hamburg, Germany & University

1. Medical Center, Hamburg-Eppendorf (UKE), Institute for Structural and Systems Biology, D-22607 Hamburg, Germany & German Electron Synchrotron Centre (DESY), D-22607 Hamburg, Germany
2. Max F. Perutz Laboratories, Department of Medical Biochemistry, Medical University of Vienna, A-1030 Vienna, Austria,
3. Jena University Hospital, Department Medical Microbiology, Section Experimental Virology, D-07740 Jena, Germany,
4. Department of Chemistry, University of Bergen, N-5020 Bergen, Norway & Computational Biology Unit (CBU), University of Bergen, N-5020 Bergen, Norway & University Hamburg, Centre for Bioinformatics, D-20146 Hamburg, Germany,
5. Federal Research Center Fundamentals of Biotechnology RAS, 119071 Moscow, Russia,
6. Institute of Biophysics, Johannes Kepler University Linz, A-4020 Linz, Austria,
7. Structural Biology Unit, Institute of Molecular Biology of Barcelona IBMB-CSIC, E-08028 Barcelona, Spain

\*these authors contributed equally to this work

\*\*corresponding authors

## Supplementary Methods

### Cells and viruses

HeLa Ohio cells (Flow Laboratories, USA) were grown in Eagle's minimal essential medium (MEM) supplemented with 5% neonatal calf serum (PAA, Cölbe, Germany). For infection with RV-A89 (ATCC VR-1199) or RV-B5 (National Collection of Pathogenic Viruses, Salisbury, UK) the same medium but with 2% serum (test medium) was employed. As RV-B5 did not replicate efficiently in suspension culture it was grown in 175 cm<sup>2</sup> T-flasks in MEM supplemented with 2% fetal calf serum and 30 mM MgCl<sub>2</sub><sup>1</sup>. Purification was as described<sup>2</sup> except that column chromatography was omitted to avoid loss of material. Serotype identity was confirmed by neutralization with type-specific antiserum from ATCC. Sequencing of the three major capsid proteins via MSMS revealed T3004 instead of A, as listed in the Uniprot database (B9V433-1). Aliquots of virus stocks were stored at -80 °C until use. Titers were determined by endpoint dilution according to Reed and Muench<sup>3</sup>.

### Effect of OBR-5-340 on single-step growth of RV-B5 in HeLa cells

Single step growth curves without (control) and with addition of OBR-5-340 were recorded by using semi-confluent one-day-old HeLa Ohio cell monolayers grown in 4-well tissue culture plates. One well per plate was mock-infected and used as additional control. RV-B5 was diluted in test medium without (control) or with 1 μM OBR-5-340 at multiplicity of infection (MOI) of 1 TCID<sub>50</sub>/cell. Three wells of a tissue culture plate per time point were challenged with 300 μl virus sample. After incubation for 1 h at 33 °C in 5% CO<sub>2</sub>, and 95% humidity, cells were washed with test medium to remove unattached virus. Then 500 μl test medium +/- respective inhibitor were added and incubation was continued at 33 °C for the times indicated in Fig. 1A. Cells were subjected to three rounds of freeze-thawing to release intracellular virus and the titer was determined as above.

## **Mechanism of action studies with RV-B5 and OBR-5-340 using a modified plaque reduction assay**

To examine the influence of OBR-5-340 on the different steps of the viral replication cycle, plaque reduction assays with RV-B5 at 15-50 plaque-forming units (PFU) were conducted in HeLa cells grown in 12-well plates as described previously for CVB3<sup>4</sup> except that the RV-B5 infected monolayers were incubated at 33 °C for 3 days. To see whether OBR-5-340 treatment of cells before infection affects viral replication, HeLa cells were pre-incubated with or without OBR-5-340 for 0.5 h at 33 °C and washed three times with test medium before virus addition. After exposure of the cell monolayers to virus for 2 h at 4 °C, the inoculum was removed and 1 mL of 0.4% agar-containing test medium without inhibitor was added (pre-treatment of cells). Neutralization of RV-B5 by OBR-5-340 was analyzed by incubating  $2.5 \times 10^5$  PFU of cell-free RV-B5 with or without the inhibitor in test medium for 1 h at 33 °C. This mixture was then diluted to non-effective inhibitor concentrations (1:5,000) and added to confluent cell monolayers for virus adsorption. After 2 h incubation at 4 °C, the virus inoculum was replaced by 1 mL of 0.4% agar-containing test medium without inhibitor. To study inhibition of viral adsorption by OBR-5-340, virus without or with the inhibitor was incubated with the cells at 4 °C for 2 h. Non-attached virus was washed away and 1 mL of 0.4% agar-containing test medium without inhibitor was added. Inhibition of uncoating was tested by adding OBR-5-340 after virus adsorption at 4 °C for 2 h followed by 1 h at room temperature. The compound was then washed away and 1 mL of 0.4% agar-containing test medium without inhibitor was added. Finally, the effect of OBR-5-340 treatment on virus uncoating and early replication was studied by adding the compound after viral adsorption (2 h at 4 °C) and penetration (1 h at RT) for 2 or 6 h, respectively, at 37 °C. Moreover, OBR-5-340 was also added immediately after adsorption for 2 h at 4 °C and kept present till the end of the experiment (after adsorption) or kept present during the whole experiment (during and after adsorption). Three days p.i. cells were fixed and stained with a crystal violet-formalin solution before plaque-counting.

## **Temperature-dependent *in vitro* uncoating of native virus and its inhibition by drugs**

Nine  $\mu\text{l}$  RV-B5 at about 0.15 mg/ml in phosphate buffered saline (PBS), were mixed with 1  $\mu\text{l}$  of the respective inhibitor in DMSO to give a final concentration of 1 mM. All samples were adjusted to a final concentration of 10 % DMSO. The samples were then incubated at 37 °C for 1 h to allow for binding of the respective inhibitors. Five  $\mu\text{l}$  of the above mixture were supplemented with 45  $\mu\text{l}$  Syto-82 (Thermo Fisher) in PBS to give a final concentration of 40  $\mu\text{M}$ . Two replicates (20  $\mu\text{l}$ ) of this mixture were then transferred into a CFX96 Touch™ Real-Time PCR Detection System (BioRad) and heated at 0.1 °C/sec from 25 °C to 90 °C while recording fluorescence ( $\lambda_{\text{ex}}=530$  nm,  $\lambda_{\text{em}}=560$  nm) every other 5 seconds. The relative fluorescence intensity and its first derivative as a function of temperature are indicated in Fig. 2 and Figs. S2 and S3.

## **Cryo-EM analysis of RV-B5 OBR-5-340 complexes and of RV-A89 in presence of OBR-5-340**

RV-B5 and RB-A89, respectively, were mixed with OBR-5-530 and incubated as in the stability assay except from the addition of Syto-82. As a control, RV-B5 was incubated with solvent alone. The solution (10  $\mu\text{l}$ ) was then mixed with 1  $\mu\text{l}$  n-dodecyl- $\beta$ -D-maltoside (0.2 % in water, Sigma) for obtaining thinner ice and better random orientations<sup>5</sup>. Aliquots of 4  $\mu\text{l}$  were applied to glow-discharged (60 s on carbon side, 25 mA) grids (Agar Scientific) with an additional layer of 4 nm continuous carbon. The grids were blotted for 3 s at 100% humidity and plunge-frozen in liquid ethane cooled with liquid nitrogen to about -188 °C, by using a Vitrobot Mark III. Grids with RV-B5 plus OBR-5-340, and with RV-A89 + OBR-5-340 were imaged on a FEI Polara EM operating at 300 kV equipped with Gatan K2 Summit direct electron detector. Movies were recorded with a K2 camera in dose-fractionation mode at a calibrated magnification of 37,000 x, corresponding to 0.97 Å per physical pixel. The dose rate on the specimen was set to be 8  $e/\text{\AA}^2\text{s}$  and total exposure time was 5 s, resulting in a total dose of 40  $e/\text{\AA}^2$ . Data for RV-B5 incubated without OBR-5-340 but with the solvent 10 % DMSO used as control, were collected on a FEI Titan Krios operating at 300 kV and movies were recorded with a Falcon III detector in linear mode. Details of the data collection are summarized in Table S1. Picking, image reconstruction

and refinement were carried out with Relion-3.0-beta2<sup>6-8</sup> by using a map of RV-A2 previously determined and Fourier-filtered to 60 Å as starting volume. ‘Bad particles’ were removed in repeated steps of 2D- and 3D-classifications and on the basis of excessive values of the relion parameter `_rlnLogLikeliContribution`. A model was built with the beta version of SwissModel <https://swissmodel.expasy.org/interactive#> (as of April 2018) allowing simultaneous modelling of hetero oligomers<sup>9-10</sup> using the Uniprot RV-B5 sequences (B9V433-1) and the automatically selected RV-B14 structure (4RHV) as template. For RV-A89 fitting, the sequence B9V4A5\_HRV89 and the model of RV-A16 (1AYN) were used. Coordinates were fitted and refined via Phenix<sup>11</sup> and validated with Coot<sup>12</sup> and Molprobit<sup>13</sup>. Structures were visualized with Chimera<sup>14</sup> and Coot. Coordinates of RV-B5, RV-B5 complexed to OBR-5-340, and of RV-A89 solved in the presence of OBR-5-340 were deposited in the pdb database (pdb-xx1, pdb-xx2, and pdb-xx3).

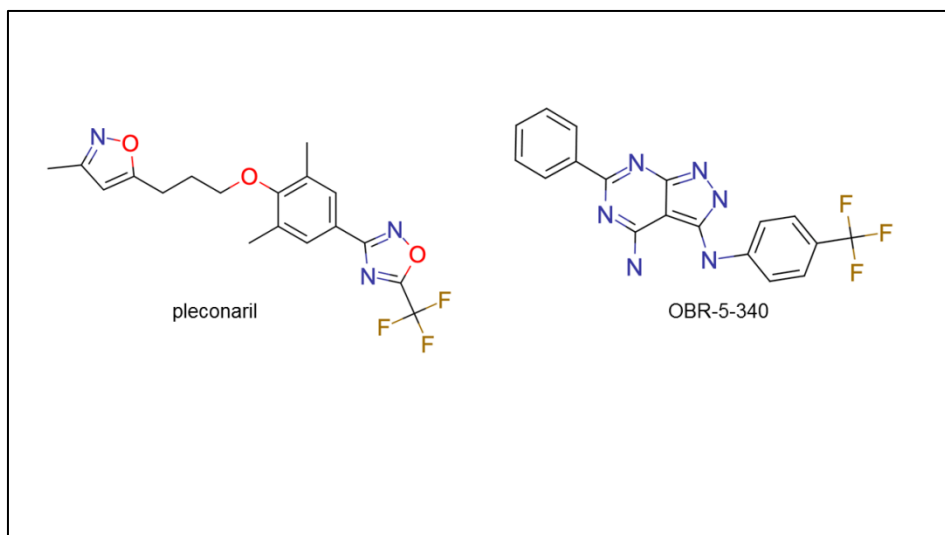


**Fig. S1** Chemical structures of capsid binders pleconaril and OBR-5-340

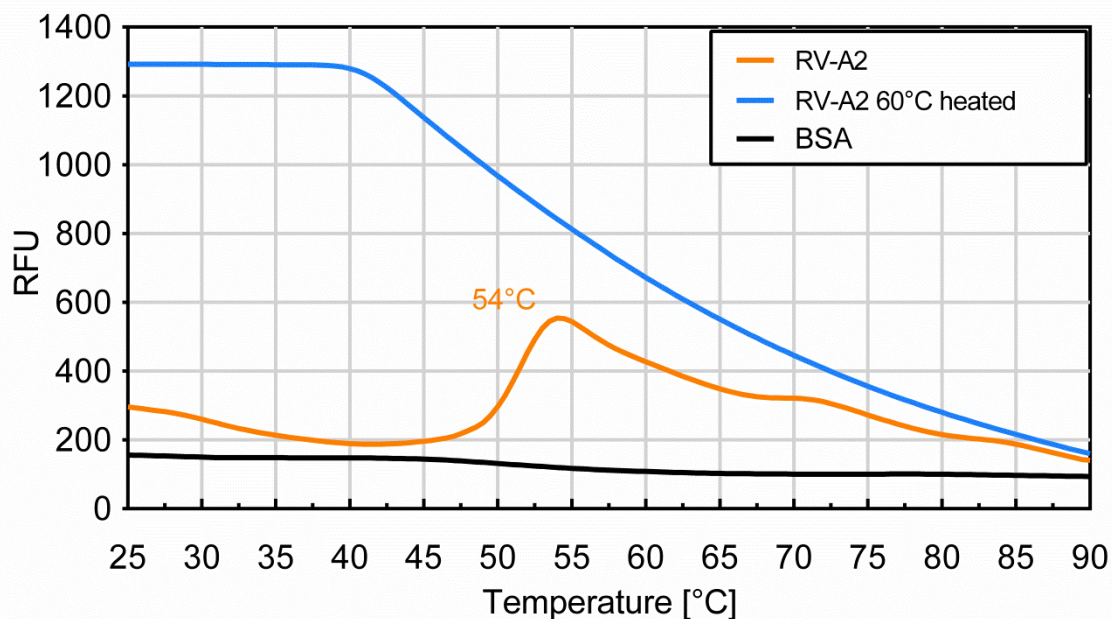


**Fig. S2** Release of the viral RNA from RV-A2 by heating to 60 °C for 5 min prior to the temperature ramping experiment results in high fluorescence. Experimental conditions were otherwise as in Fig. 2. Note that the fluorescence remains unchanged up to about 40 °C from where on it decreases presumably because of dissociation of the dye and/or RNA unfolding. When compared to the control that was not heated, it is apparent that the two effects, the RNA becoming accessible for the dye and the fluorescence being declining at elevated temperature, are counteracting. However, the former one overwhelms the latter one. No fluorescent signal was recorded when 20 µg bovine serum albumin was used instead of the viral probes. This excludes a signal occurring upon interactions of the dye with DMSO and/or OBR-5-340.

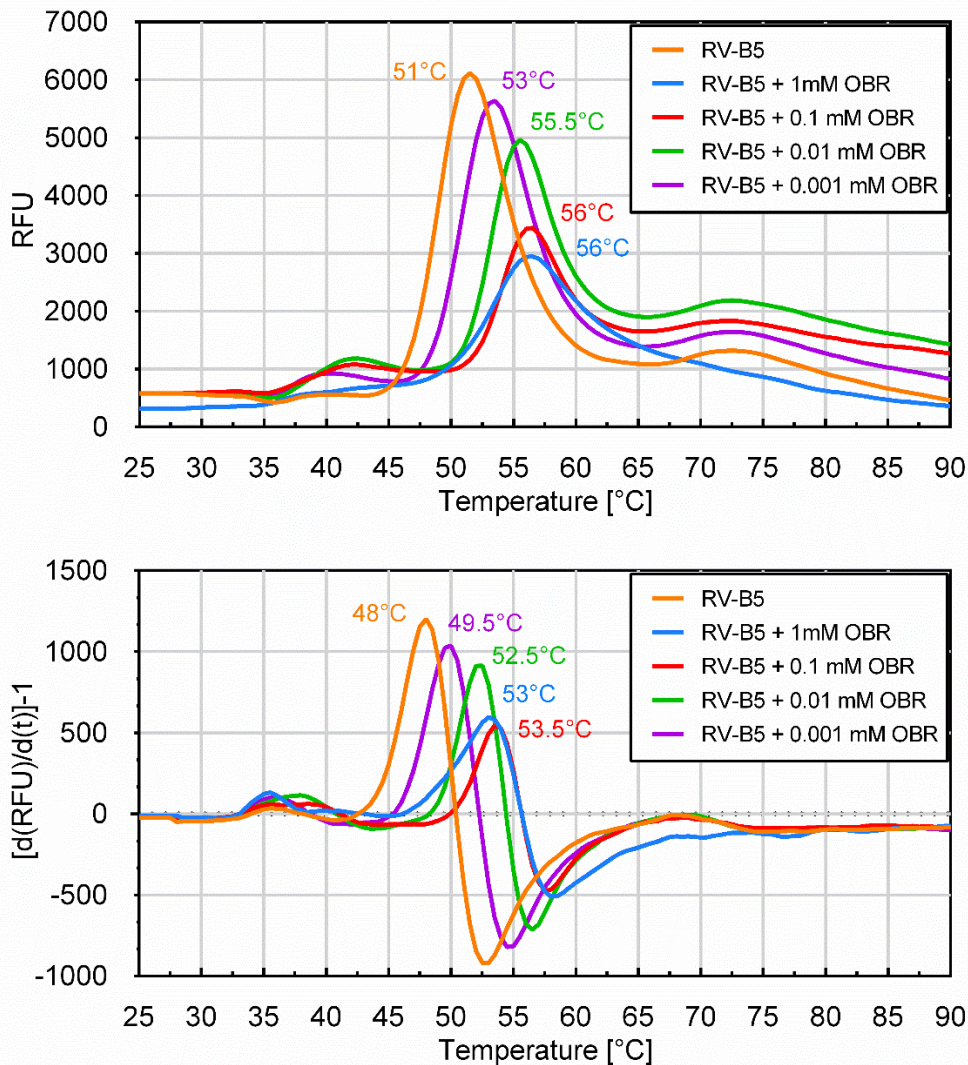
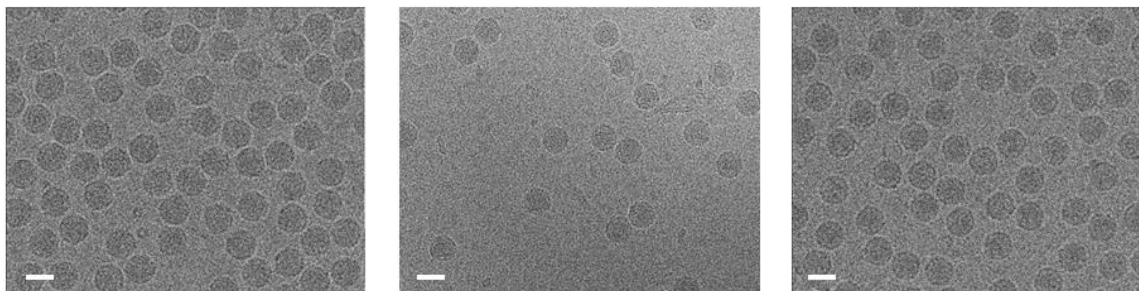


**Fig. S3** RV-B5 is stabilized by OBR-5-340 against conversion into subviral particles with accessible RNA at elevated temperatures in a concentration-dependent manner. The experiments were carried out as in Fig. 2. Briefly, 9  $\mu$ l RV-B5 at about 0.15 mg/ml in phosphate buffered saline (PBS), were mixed with 1  $\mu$ l of OBR-5-340 in DMSO to give final concentrations of 1  $\mu$ M, 10  $\mu$ M, 100  $\mu$ M, and 1 mM, respectively. All samples were adjusted to a final concentration of 10 % DMSO. The samples were then incubated at 37  $^{\circ}$ C for 1 h to allow for binding. Five  $\mu$ l of the above mixture were supplemented with 45  $\mu$ l Syto-82 (Thermo Fisher) in PBS to give a final concentration of 40  $\mu$ M, transferred into a CFX96 Touch™ Real-Time PCR Detection System (BioRad) and heated at 0.1  $^{\circ}$ C/sec from 25  $^{\circ}$ C to 90  $^{\circ}$ C while recording fluorescence ( $\lambda_{ex}$ =530 nm,

$\lambda_{em} = 560 \text{ nm}$ ) every other 5 seconds. The change in relative fluorescence intensity (upper panel) and its first derivative (lower panel) as a function of temperature are indicated. Note that presence of even  $1 \mu\text{M}$  OBR-5-340 resulted in a clear shift of the temperature of fluorescence onset by  $1.5 \text{ }^\circ\text{C}$ .



RV-B5 + OBR-5-340

RV-B5 solvent control

RV-A89 + OBR-5-340

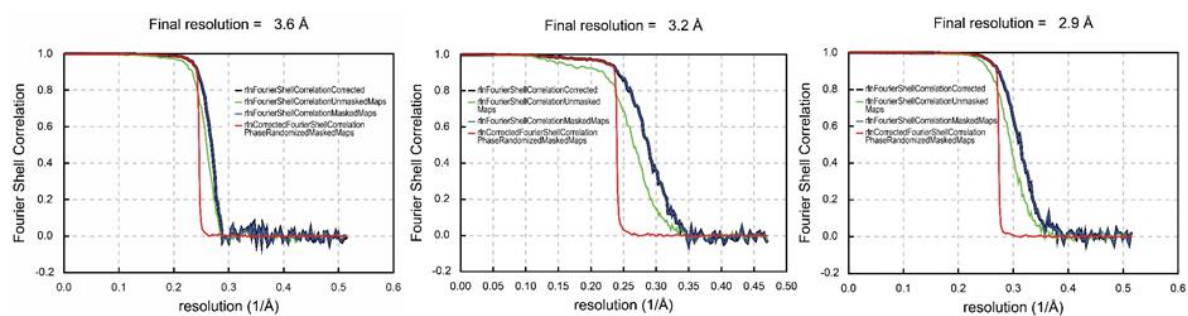


**Fig. S4:** Examples of motion-corrected micrographs of RV-B5 + OBR-5-340, RV-B5, and RV-A89 + OBR-5-340. Size bar is 30 nm (top). The respective resolution was calculated according to the 0.143 criteria as output from relion-3.0 (bottom).

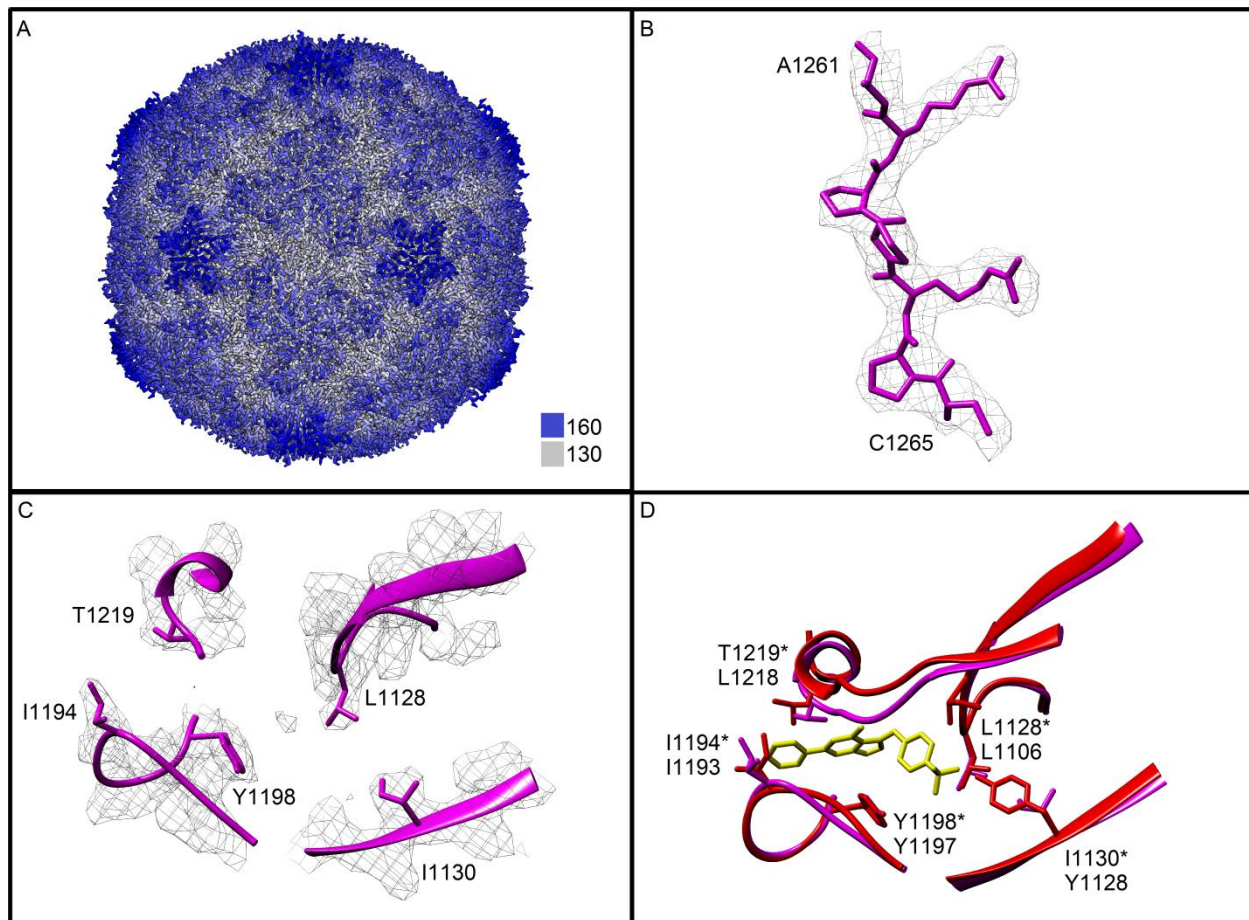


**Fig. S5:** Cryo-EM structure of the OBR-5-340 resistant RV-A89 incubated with OBR-5-340; A) Coloured radially as indicated by the colour bar. Distance from the viral centre is 130 Å (white) to 160 Å (dark blue). B) Example of the quality of the map. C) View centered on the position where OBR-5-340 is found in the complex with RV-B5; note that the orientation is exactly as in (Fig. 3C, D). D) Superposition of models of RV-B5 and RV-A89 showing that the region of AA 1200 to 1218 is slightly shifted downward in the latter (arrow), which might be a reason for lack of binding of OBR-5-340.

RV-B5 GLEDDLVEVIVDKAQ---**OTLASIKSDSKHTQKVPSLTANETGATLPTTPSDSVETRTT** 56  
 RV-A89 ----NPVENYIDSVLNEVLVVPNIQPSTSVSSHAAPALDAAETGHTSSVQPEDMIETRYV 59  
 \* :: \* \* :\* . \* \* :: \* \* \* \* \* \* \* \* \* \* \* \* \* \* \* \*

RV-B5 LMHYTGSETTLENFLGRAACVHVVEIVNKRPTDTEEHRMQLLFNNWK**INLSSLVQLRRKL** 116  
 RV-A89 ITDQTRDETSIESFLGRSGCIAMIEFNIS-SDKTEHDKIGKGFKTWKVSLQEMAQIRRY 118  
 : . \*

RV-B5 EMFTYVRFDSEYTHIATSSQPNEAKFSSNLTIQAM**FIPPGAPNPKKWDDYTWQSATNPSV** 176  
 RV-A89 ELFTYTRFDSEITIVTAAAA--QGNDSGHIVLQFMVPPGAPVPEKRDDYTWQSGTNASV 176  
 \*

RV-B5 FFNVGKS-ARFSVPY**LGIASAY**NCFYDGYSHDNSTTPYGINV**L**NHMGSMAFRVVNEHDNH 235  
 RV-A89 FWQEGOPYPRFTIP**FMSIASAY**MFYDGYDGDGSAASKYGSVV**T**NDMGTCVRIVTSNOKH 236  
 \* : \* : \* \* : \*

RV-B5 TTHVKVRVYHRAKHIRAWVPRAPRALEYLHIGRTNYKQSPQNPIK---**TRKTISTY**--- 288  
 RV-A89 DSNIVCRIYHKAKHIKAWCPRPPRAVAYQHTHSTNYIPSNGEATTQIKTRPDVFTVTVN 295  
 : : \*

**Fig. S6:** Clustal Omega alignment of capsid protein VP1 of RV-B5 and RV-A89 with default parameters. RV-B5 VP1 residues in proximity of OBR-5-340 as shown in Fig. 4 are indicated in **red-italic-bold-underlined**. The corresponding residues in RV-A89 are also shown for comparison. Residues visible in the respective cryo-EM maps are underlined in black. For a list of these residues see Table S3.

**Table S1: Statistics of 3D-structure determination of RVs ± drug**

<b>Cryo-EM statistics RV-B5 complexed with OBR-5-340</b>									
No of Micrographs <sup>a</sup>	Defocus (μm)	Pixel size (Å)	Dose rate (e <sup>-</sup> /Å <sup>2</sup> s)	Frame rate (ms)	Total dose (e <sup>-</sup> / Å <sup>2</sup> )	No of Particles picked	No of Particles used for reconstruction	Resolution <sup>b</sup> (Å)	Map sharpening B-factor (Å <sup>2</sup> )
2,547	0.3 – 4.6	0.97	1.6	200	40	165,291	46,070	3.6	-192
<b>Model statistics</b>									
FSCC between model and map <sup>c</sup>	No of atoms (protein /OBR-5-340)	Average B-factor (Å <sup>2</sup> )	RMSD bond lengths (Å) <sup>c</sup>	RMSD bond Angles (°) <sup>c</sup>	Ramachandran plot favoured (%) <sup>d</sup>	Ramachandran plot allowed (%) <sup>d</sup>	Ramachandran plot outliers (%) <sup>d</sup>		
0.8559	12347/39	39.8 / 33.37	0.0175	1.18	97.2	2.67	0.13		
<b>Cryo-EM statistics RV-B5 (control)</b>									
No of Micrographs <sup>e</sup>	Defocus (μm)	Pixel size (Å)	Dose rate (e <sup>-</sup> /Å <sup>2</sup> s)	Frame rate (ms)	Total dose (e <sup>-</sup> / Å <sup>2</sup> )	No of Particles picked	No of Particles used for reconstruction	Resolution <sup>b</sup> (Å)	Map sharpening B-factor (Å <sup>2</sup> )
1,400	0.9 – 3.3	1.061	1.4	25	56	41,638	13,656	3.2	-192
<b>Model statistics</b>									
FSCC between model and map <sup>c</sup>	No of atoms (protein)	Average B-factor (Å <sup>2</sup> )	RMSD bond lengths (Å) <sup>c</sup>	RMSD bond Angles (°) <sup>c</sup>	Ramachandran plot favoured (%) <sup>d</sup>	Ramachandran plot allowed (%) <sup>d</sup>	Ramachandran plot outliers (%) <sup>d</sup>		
0.8480	12347	30.88	0.0262	1.26	98.09	1.78	0.13		
<b>Cryo-EM statistics RV-A89 (control)</b>									
No of Micrographs <sup>a</sup>	Defocus (μm)	Pixel size (Å)	Dose rate (e <sup>-</sup> /Å <sup>2</sup> s)	Frame rate (ms)	Total dose (e <sup>-</sup> / Å <sup>2</sup> )	No of Particles picked	No of Particles used for reconstruction	Resolution <sup>b</sup> (Å)	Map sharpening B-factor (Å <sup>2</sup> )
5,370	0.3 – 5.1	0.97	1.6	200	40	188,880	107,054	2.9	-192
<b>Model statistics</b>									
FSCC between model and map <sup>c</sup>	No of atoms (protein)	Average B-factor (Å <sup>2</sup> )	RMSD bond lengths (Å) <sup>c</sup>	RMSD bond Angles (°) <sup>c</sup>	Ramachandran plot favoured (%) <sup>d</sup>	Ramachandran plot allowed (%) <sup>d</sup>	Ramachandran plot outliers (%) <sup>d</sup>		
0.7476	12495	23.25	0.0249	1.26	97.03	2.85	0.12		

<sup>a</sup> Cryo-EM data were collected using an FEI Polara transmission electron microscope operated at 300 kV with a Gatan K2 Summit direct electron detector

<sup>b</sup> Estimated on the basis of Fourier shell correlation between two half maps using a cut-off of 0.143

<sup>c</sup> Between the cryo-EM map and map calculated based on the atomic model specifying the cryo-EM map using the program Phenix

<sup>d</sup> Based on the criteria of MolProbity

<sup>e</sup> Cryo-EM data were collected by using a FEI Titan Krios transmission electron microscope operated at 300 kV with a Falcon III direct electron detector in linear mode; this data collection was funded by grant 11437 from iNext.

**Table S2: List of PDB structures aligned to RV-B5 and shown in Figure 4.**

1AL2	1FPN	1PO1	1RUE	2HWB	2RS1	4AED	5ABJ
1AR6	1HRI	1PO2	1RUG	2HWC	2RS3	4CDQ	5C4W
1AR7	1HRV	1POV	1RUH	2HWD	2RS5	4CDU	5C8C
1AR8	1K5M	1PVC	1RUI	2HWE	2X5I	4CDW	5C9A
1AR9	1MQT	1QJU	1V9U	2HWF	3DPR	4CDX	5OSN
1ASJ	1NA1	1QJX	1VBA	2PLV	3VBF	4CEW	
1AYM	1NCQ	1QJY	1VBB	2R04	3VBS	4CEY	
1AYN	1NCR	1R08	1VBC	2R06	3VDD	4N53	
1C8M	1ND3	1R09	1VBD	2R07	3ZFE	4PDW	
1D4M	1OOP	1RUC	1VBE	2RM2	3ZFF	4WM7	
1EAH	1PIV	1RUD	1VRH	2RR1	3ZFG	4WM8	

**Table S3:** List of residues in proximity of OBR-5-340 shown in Fig. 4 and in Fig. S5 as ***red-italic-bold-underlined***.

<b>RV-B5</b>	<b>RV-A89</b>
I1104	V1108
L1106	L1108
F1152	Y1152
L1191	M1192
I1193	I1194
A1194	A1195
Y1197	Y1198
L1218	T1219

## References

1. Fiala M & Kenny GE (1967) Effect of magnesium on replication of rhinovirus HGP. *J Virol* 1(3):489-493.
2. Allmaier G, *et al.* (2018) Monolithic anion-exchange chromatography yields rhinovirus of high purity. *J Virol Methods* 251:15-21.
3. Reed LJ & Muench H (1938) A simple method of estimating fifty per cent endpoints *J. Am. Hyg.* 27(3):493-497.
4. Makarov VA, *et al.* (2015) Pyrazolopyrimidines: Potent Inhibitors Targeting the Capsid of Rhino- and Enteroviruses. *ChemMedChem* 10(10):1629-1634.
5. Drulyte I, *et al.* (2018) Approaches to altering particle distributions in cryo-electron microscopy sample preparation. *Acta Crystallogr D Struct Biol* 74(Pt 6):560-571.
6. Kimanius D, Forsberg BO, Scheres SH, & Lindahl E (2016) Accelerated cryo-EM structure determination with parallelisation using GPUs in RELION-2. *Elife* 5.
7. Scheres SH (2016) Processing of Structurally Heterogeneous Cryo-EM Data in RELION. *Methods Enzymol* 579:125-157.
8. Scheres SH (2012) RELION: implementation of a Bayesian approach to cryo-EM structure determination. *J Struct Biol* 180(3):519-530.
9. Bienert S, *et al.* (2017) The SWISS-MODEL Repository-new features and functionality. *Nucleic Acids Res* 45(D1):D313-D319.
10. Schwede T, Kopp J, Guex N, & Peitsch MC (2003) SWISS-MODEL: An automated protein homology-modeling server. *Nucleic Acids Res* 31(13):3381-3385.
11. Adams PD, *et al.* (2010) PHENIX: a comprehensive Python-based system for macromolecular structure solution. *Acta Crystallogr D Biol Crystallogr* 66(Pt 2):213-221.
12. Emsley P, Lohkamp B, Scott WG, & Cowtan K (2010) Features and development of Coot. *Acta Crystallogr D Biol Crystallogr* 66(Pt 4):486-501.
13. Davis IW, *et al.* (2007) MolProbity: all-atom contacts and structure validation for proteins and nucleic acids. *Nucleic Acids Res* 35(Web Server issue):W375-383.
14. Pettersen EF, *et al.* (2004) UCSF Chimera--a visualization system for exploratory research and analysis. *J Comput Chem* 25(13):1605-1612.

## Concluding thoughts and future challenges

There is no discussion, that cryo-EM became one of the key method in structure determination within the last decade. With the new generation of very stable and fully automated Titan (Thermo Fisher) microscopes equipped with K3/Falcon 4 cameras allowing fully automated data collection together with the user-friendly software packages for data processing (Relion, CryoSparc, SPHIRE etc.) became cryo-EM technique easily available for everybody even without deep prior knowledge. Such a high-end microscopes are now present at almost every scientific center and despite it's relatively high running cost, project cost can be easily covered by specialized grants, which are usually rapidly evaluated. Thanks to the rapidly evolving “cryo-EM related” technologies we can currently solve structures of flexible structures from ~40kDa to several megadaltons or image entire cells using cryo-electron tomography. Although many technical challenges are still in front of cryo-EM – SPA (single particle analysis) and cryo-ET (tomography and sub-tomogram averaging,) cryo-EM techniques became a new standard in structural biology. There is no doubt that within the following years more automatization of sample preparation step (vitrification), data acquisition and data processing will be introduce, so even less user interaction will be needed – similarly to the “robotization” progress in x-ray crystallography around the millennium. With other words, cryo-EM will soon become a real “high throughput” method. This must come together with strong structure validation methods (at the level of EM density maps), however, and we should also always keep in mind the biological relevance of obtained structures.

In general, there are two main strategies to biochemically obtain the target sample: (a) purification directly from cells or (2) *in vitro* reconstitution. Both approaches have their pros and cons - the deciding factor is mostly the type and properties of sample, however (stability, intracellular quantity, cytosolic or membrane complex localization, etc.). The biological relevance of the obtained 3D structure should be then always unbiasedly assessed and interpreted in respect to the preparation strategy. Especially when the *in vivo* or *in vitro* activity can not be experimentally tested<sup>49</sup> or if components are missing in the structure<sup>50</sup>. Thus, we should always be extraordinary careful once we want the infer the potential mechanisms. This turned out to especially important in structural studies of AAA+ machines to understand the substrate processing mechanisms and

it's coupling to the hydrolytic cycle<sup>51,52</sup>. In the light of the results shown in the first chapter, it is also questionable to what extent we can mimic transitional states of AAA+ proteins connected to the ATP hydrolysis by using different ATP analogues (ADP:AlF<sub>x</sub> or ADP:BeF<sub>x</sub>) since we see, that the RuvB AAA+ motor must go through a series of states to reach the hydrolysis competent state (s2).

Thus, I believe that the next step in structural biology is to use all the offered advantages of cryo-EM (especially SPA) and apply them to complex biological samples, which we trap in functional related states (through impairing the kinetic of the chemical reaction) to resolve the conformational landscape covering the critical steps at high-resolution. This would allow us to design state specific drugs to target the vital molecular machines with better specificity and effectiveness.



## Abbreviations

cryo-EM	Cryo-electron microscopy
DDM	n-dodecyl- $\beta$ -D-maltopyranoside
AAA+	ATPases Associated with diverse cellular Activities
ADP	Adenosine diphosphate
ATP	Adenosine triphosphate
ATP $\gamma$ S	Adenosine-5'-( $\gamma$ -thio)-triphosphate
dsDNA	double stranded DNA
ssDNA/RNA	single stranded DNA/RNA
EM	electron microscopy
PDB	protein data bank
EMDB	electron microscopy data bank
WT	wild type
FSC	Fourier shell correlation
HRV	human rhinoviruses
OBR-5-340	3-(4-trifluoromethylphenyl)amino-6-phenylpyrazolo[3,4-d]pyrimidine-4-amine
VP 1-4	viral capsid protein (1-4)
MOI	multiplicity of infection
HJ	Holliday junction
PBS	phosphate buffered saline
DMSO	Dimethyl sulfoxide

## References

1. Neupert, W. Highlight: Molecular machines. *Biological Chemistry* **386**, 711 (2005).
2. Grimes, J. M. & Stuart, D. I. Large unit cells and cellular mechanics. *Nature Structural Biology* **5**, 630–634 (1998).
3. Ward, A. B., Sali, A. & Wilson, I. A. Integrative structural biology. *Science* **339**, 913–915 (2013).
4. Fox, S. W. From non-random molecular structure to life and mind. *Journal of Molecular Structure: THEOCHEM* **199**, 183–188 (1989).
5. B, A. The cell as a collection of protein machines: preparing the next generation of molecular biologists. *Cell* **92**, 291–294 (1998).
6. Chen, B. Structural dynamics of ribosome subunit association studied by mixing-spraying time-resolved cryogenic electron microscopy. *Structure* **23**, 1097–1105 (2015).
7. R Danev, W. B. Cryo-EM single particle analysis with the Volta phase plate. *eLife* **5**, e13046 (2016).
8. CJ Russo, L. P. Progress towards an optimal specimen support for electron cryomicroscopy. *Curr. Opin. Struct. Biol.* **37**, 81–89 (2016).
9. T Jain, P. S. J. C. B. C. C. P. Spotiton: a prototype for an integrated inkjet dispense and vitrification system for cryo-TEM. *J. Struct. Biol.* **179**, 68–75 (2012).
10. Razinkov, I. A new method for vitrifying samples for cryoEM. *J. Struct. Biol.* **195**, 190–198 (2016).
11. Scheres, S. A Bayesian view on cryo-EM structure determination. *J. Mol. Biol.* **415**, 406–418 (2012).
12. Scheres, S. Disentangling conformational states of macromolecules in 3D-EM through likelihood optimization. *Nat. Methods* **4**, 27–29 (2007).
13. RA Grassucci, D. T. J. F. Visualization of macromolecular complexes using cryo-electron microscopy with FEI Tecnai transmission electron microscopes. *Nat. Protoc.* **3**, 330–339 (2008).
14. Frank, J. Advances in the field of single-particle cryo-electron microscopy over the last decade. *Nature Protocols* 2017 12:2 **12**, 209–212 (2017).

15. RA Grassucci, D. T. J. F. Preparation of macromolecular complexes for cryo-electron microscopy. *Nat. Protoc.* **2**, 3239–3246 (2007).
16. Serna, M. Hands on methods for high resolution cryo-electron microscopy structures of heterogeneous macromolecular complexes. *Frontiers in Molecular Biosciences* **6**, (2019).
17. Rivera-Calzada, A. & Carroni, M. Editorial: Technical Advances in Cryo-Electron Microscopy. *Frontiers in Molecular Biosciences* **6**, 72 (2019).
18. Assaiya, A., Burada, A. P., Dhingra, S. & Kumar, J. An overview of the recent advances in cryo-electron microscopy for life sciences. *Emerging Topics in Life Sciences* **5**, 151–168 (2021).
19. Tan, Y. Z. *et al.* Sub-2 Å Ewald Curvature Corrected Single-Particle Cryo-EM. *bioRxiv* 305599 (2018) doi:10.1101/305599.
20. Zhu, D. *et al.* Pushing the resolution limit by correcting the Ewald sphere effect in single-particle Cryo-EM reconstructions. *Nature Communications* **9**, (2018).
21. Brilot, A. F. *et al.* Beam-induced motion of vitrified specimen on holey carbon film. *Journal of Structural Biology* **177**, 630–637 (2012).
22. Rubinstein, J. L. & Brubaker, M. A. Alignment of cryo-EM movies of individual particles by optimization of image translations. *Journal of Structural Biology* **192**, 188–195 (2015).
23. Punjani, A., Rubinstein, J. L., Fleet, D. J. & Brubaker, M. A. CryoSPARC: Algorithms for rapid unsupervised cryo-EM structure determination. *Nature Methods* **14**, 290–296 (2017).
24. Bai, X. C. *et al.* An atomic structure of human  $\gamma$ -secretase. *Nature* **525**, 212–217 (2015).
25. Cheng, A. *et al.* High Resolution Single Particle Cryo-Electron Microscopy using Beam-Image Shift. *High resolution single particle cryo-electron microscopy using beam-image shift* 306241 (2018) doi:10.1101/306241.
26. Abrishami, V. *et al.* Alignment of direct detection device micrographs using a robust Optical Flow approach. *Journal of Structural Biology* **189**, 163–176 (2015).
27. Naydenova, K. & Russo, C. J. Measuring the effects of particle orientation to improve the efficiency of electron cryomicroscopy. *Nature Communications* **8**, (2017).
28. Kimanius, D., Forsberg, B. O., Scheres, S. H. W. & Lindahl, E. Accelerated cryo-EM structure determination with parallelisation using GPUS in RELION-2. *eLife* **5**, (2016).

29. Nakane, T., Kimanius, D., Lindahl, E. & Scheres, S. H. W. Characterisation of molecular motions in cryo-EM single-particle data by multi-body refinement in RELION. *eLife* **7**, (2018).
30. Merk, A. *et al.* Breaking Cryo-EM Resolution Barriers to Facilitate Drug Discovery. *Cell* **165**, 1698–1707 (2016).
31. Zivanov, J. *et al.* New tools for automated high-resolution cryo-EM structure determination in RELION-3. *eLife* **7**, (2018).
32. Glaeser, R. M., Typke, D., Tiemeijer, P. C., Pulokas, J. & Cheng, A. Precise beam-tilt alignment and collimation are required to minimize the phase error associated with coma in high-resolution cryo-EM. *Journal of Structural Biology* **174**, 1–10 (2011).
33. Fernandez-Leiro, R. & Scheres, S. H. W. Unravelling biological macromolecules with cryo-electron microscopy. *Nature* **537**, 339–346 (2016).
34. Kühlbrandt, W. The resolution revolution. *Science* **343**, 1443–1444 (2014).
35. Liu, Y. & West, S. C. Happy Hollidays: 40th anniversary of the Holliday junction. *Nature Reviews Molecular Cell Biology* *2004 5:11* **5**, 937–944 (2004).
36. J, M. & SC, W. Holliday junction resolution: regulation in space and time. *DNA repair* **19**, 176–181 (2014).
37. B, M. & SC, W. Processing of Holliday junctions by the Escherichia coli RuvA, RuvB, RuvC and RecG proteins. *Experientia* **50**, 216–222 (1994).
38. SC, K., DA, D., AK, E., SD, L. & WM, R. Biochemistry of homologous recombination in Escherichia coli. *Microbiological reviews* **58**, 401–465 (1994).
39. A, K. Unraveling the late stages of recombinational repair: metabolism of DNA junctions in Escherichia coli. *BioEssays : news and reviews in molecular, cellular and developmental biology* **18**, 757–765 (1996).
40. B, M., AK, S. & DRF, L. Replication Fork Breakage and Restart in Escherichia coli. *Microbiology and molecular biology reviews : MMBR* **82**, (2018).
41. B, M., H, B., Z, B., M, L. & R, L. Recombination proteins and rescue of arrested replication forks. *DNA repair* **6**, 967–980 (2007).
42. SC, W. Processing of recombination intermediates by the RuvABC proteins. *Annual review of genetics* **31**, 213–244 (1997).

43. Callaway, E. “It opens up a whole new universe”: Revolutionary microscopy technique sees individual atoms for first time. *Nature* **582**, 156–157 (2020).
44. Nakane, T. *et al.* Single-particle cryo-EM at atomic resolution. *Nature* **587**, (2020).
45. Yamada, K. *et al.* Crystal structure of the RuvA-RuvB complex: A structural basis for the holliday junction migrating motor machinery. *Molecular Cell* **10**, 671–681 (2002).
46. SJ, N. vls Antigenic Variation Systems of Lyme Disease Borrelia: Eluding Host Immunity through both Random, Segmental Gene Conversion and Framework Heterogeneity. *Microbiology spectrum* **2**, (2014).
47. Royston, L. & Tapparel, C. Rhinoviruses and Respiratory Enteroviruses: Not as Simple as ABC. *Viruses 2016, Vol. 8, Page 16* **8**, 16 (2016).
48. Palmenberg, A. C. *et al.* Sequencing and Analyses of All Known Human Rhinovirus Genomes Reveal Structure and Evolution. *Science* **324**, 55–59 (2009).
49. Jacobs, S. E., Lamson, D. M., Kirsten, S. & Walsh, T. J. Human rhinoviruses. *Clinical Microbiology Reviews* **26**, 135–162 (2013).
49. Bunduc, C. M. *et al.* Structure and dynamics of a mycobacterial type VII secretion system. *Nature 2021 593:7859* **593**, 445–448 (2021).
50. Beckham, K. S. H. *et al.* Structure of the mycobacterial ESX-5 type VII secretion system pore complex. *Science Advances* **7**, eabg9923 (2021).
51. Peña, A. H. de la, Goodall, E. A., Gates, S. N., Lander, G. C. & Martin, A. Substrate-engaged 26S proteasome structures reveal mechanisms for ATP-hydrolysis-driven translocation. *Science* **362**, (2018).
52. Dong, Y. *et al.* Cryo-EM structures and dynamics of substrate-engaged human 26S proteasome. *Nature 2018 565:7737* **565**, 49–55 (2018).